ALPHA-CAPTURE REACTION RATES FOR ^{22}NE(α,N)^{25}MG AND ^{22}NE(α,γ)^{26}MG REACTIONS VIA SUB-COULOMB ALPHA-TRANSFER AND THEIR EFFECTS ON FINAL ABUNDANCES OF S-PROCESS ISOTOPES

A Dissertation

by

DANGALLAGE HESHANI JAYATISSA

Submitted to the Office of Graduate and Professional Studies of
Texas A&M University
in partial fulfillment of the requirements for the degree of

DOCTOR OF PHILOSOPHY

Chair of Committee,	Grigory V. Rogachev
Committee Members,	Carl A. Gagliardi
	Charles M. Folden III
	Jeremy W. Holt
	Nicholas Suntzeff
Head of Department,	Grigory V. Rogachev

August 2019

Major Subject: Physics

ABSTRACT

The ^{22}Ne(α,n) reaction is an important neutron source reaction for the slow neutron capture process (s-process) in asymptotic giant branch stars. Direct measurements are extremely difficult to carry out at Gamow energies due to the extremely small reaction cross section. The large uncertainties introduced when extrapolating direct measurements at high energies down to the Gamow energies can be overcome by determining the partial α-width of the relevant states using indirect measurements. This can be done using α-transfer reactions at sub-Coulomb energies to reduce the dependence on optical model parameters. The α-transfer reaction of ^{22}Ne(^{6}Li,d)^{26}Mg was carried out at the Cyclotron Institute at Texas A&M University to study this reaction. It appears that the partial α widths of the near α-threshold resonances of ^{26}Mg are different from what was previously assumed. This discrepancy affects the final ^{22}Ne(α,n) reaction rate and the final abundances of the s-process isotopes.

DEDICATION

To my mom, a small replacement for the degree you couldn't complete when I was born.

ACKNOWLEDGMENTS

I would like to express my heartfelt gratitude to my advisor Dr. Grigory Rogachev for taking me under his wing, and for being a truly remarkable mentor and a pillar of support. His remarkable knowledge, infectious enthusiasm, constant guidance made this work entirely possible. His door was always open for me whenever I had any questions.

I am also indebted to Dr. Yevgen Koshchiy for all his support through each step of my time as a graduate student. The experimental setup for the data analyzed in this dissertation work would not have been possible without him.

Additional thanks goes to Dr. Vladilen Goldberg for all the fruitful and encouraging educational discussions over the past years.

For my constant cheerleaders, Sriteja Upadhyayula and Joshua Hooker, thank you from the bottom of my heart for always encouraging me and for making my graduate school life enjoyable and bearable. A special thank you goes to my other group members Dr. Sunghoon (Tony) Ahn and Dr. Jack Bishop for their help during my graduate work.

I would like to convey my gratitude to my committee members Prof. Carl Gagliardi, Prof. Charles M. Folden III, Prof. Jeremy Holt and Prof. Nicholas Suntzeff for their advice and input.

Finally, I would like to thank Dr. Brian Roeder and Dr. Antti Saastamoinen for their help with the beam used for this experiment, and the Cyclotron Institute support staff, the Cyclotron Operations Group, and the machine shop staff, for their help and assistance with the work behind this project.

CONTRIBUTORS AND FUNDING SOURCES

Contributors

This work was supervised by a dissertation committee consisting of Professor Grigory V. Rogachev [advisor] and Professors Carl A.Gagliardi, Jeremy W. Holt, Nicholas Suntzeff of the Department of Physics and Astronomy, and Professor Charles M. Folden III of the College of Science.

This research used targets provided by the Center for Accelerator Target Science at Argonne National Laboratory.

All other work conducted for the dissertation was completed by the student independently.

Funding Sources

Graduate study was supported by teaching and research assistantships from the Cyclotron Institute and Texas A&M University. The dissertation work was funded in part by the U.S. Department of Energy, Office of Science under Grant DE-FG02-93ER40773, and by the support of the Welch Foundation (Grant. No. A-1853).

TABLE OF CONTENTS

Page

LIST OF FIGURES

FIGURE Page

LIST OF TABLES

TABLE Page

1. INTRODUCTION

1.1 Origin of the chemical elements in the Universe

Understanding the origin of the chemical elements present in the Universe has been a fundamental question that many scientists are attempting to answer. In 1948, Alpher, Bethe and Gamow made a breakthrough in nuclear astrophysics with the suggestion that all the chemical elements in the Universe were created in the Big Bang explosion. This work was published in their groundbreaking work *"The Origin of the Chemical Elements."* [10]. This paper argued that the Big Bang created hydrogen and helium, and all the rest of the atomic nuclei were produced by successive neutron captures on these two elements, one mass unit at a time. This latter part was contradicted later on with the discovery of the absence of any stable nuclei with masses A=5 or A=8.

The physics of chemical evolution is far more nuanced and interesting. While only the three lightest elements, hydrogen, helium and lithium, are created during the Big-Bang nucleosynthesis, all the rest of the elements are created during various complex nucleosynthesis processes occurring in stellar environments. There exists a cyclic process in the Universe where stellar matter is transferred between gas clouds and stars, creating more and more complex atoms in the process. It was proposed by Burbridge, Burbridge, Fowler and Hoyle in the famous work [11], the *"B^2FH paper"*, that most of the chemical elements are formed in the interiors of stars. This work outlined various important stellar nucleosynthesis scenarios which result in the production of the chemical elements, and is the basis for our understanding of the origin of all the chemical elements in the Universe.

The astrophysical sites still are uncertain for several major nucleosynthesis processes such as the proton capture process (p-process) [12, 13]. Various theoretical and experimental efforts are currently being utilized to further the understanding of this significant topic of stellar nucleosynthesis.

1.2 Nucleosynthesis beyond Iron

The B^2FH paper hypothesized that nuclear reaction processes involving neutron captures and subsequent β-decays on seed material such as iron and other intermediate mass nuclei occur within stellar interiors in order to synthesize heavier elements than iron. This synthesis process can occur at two different rates: a slow rate (slow neutron capture process ("*s-process*")), or a rapid rate (rapid neutron capture process ("*r-process*")). The neutrons for the s-process are predominantly produced during the helium-burning phase in red giant stars through (α,n) reactions. It is believed that the majority of the elements above iron is created through the s-process and the r-process.

The neutron captures for these two processes occur via (n, γ) reactions during which the mass number of the starting element is increased by one unit at a time. For each neutron capture, a nucleus (A, Z) is changed to a heavier isotope of (A+1, Z). If this new isotope is stable, it can lead to another neutron capture, subsequently creating the nucleus (A+2, Z) and so on. In case of an unstable isotope being produced in this chain, the next step will be determined by the intensity of the flux of neutrons in the immediate environment and on the β-decay lifetime of the unstable nuclei.

For the s-process, the time between two successive neutron captures is much larger than the β-decay lifetimes. Due to this reason, the s-process closely follows the valley of β-stability (see Figure 1.1 from Ref. [14]). The r-process is on the neutron-rich extreme, where the time between two successive neutron captures is much smaller than the β-decay lifetimes. The r-process follows close to the neutron drip line (a region where neutron binding energies are very small) far from the valley of stability. This occurs in environments where the neutron density is very high, on the order of $\sim 10^{20}$ neutrons cm^{-3}, which is roughly about 10 orders of magnitude higher than for the s-process. Once the high neutron flux ceases, the neutron rich nuclei will have successive β-decays into the region of stability, synthesizing elements not possible by the s-process.

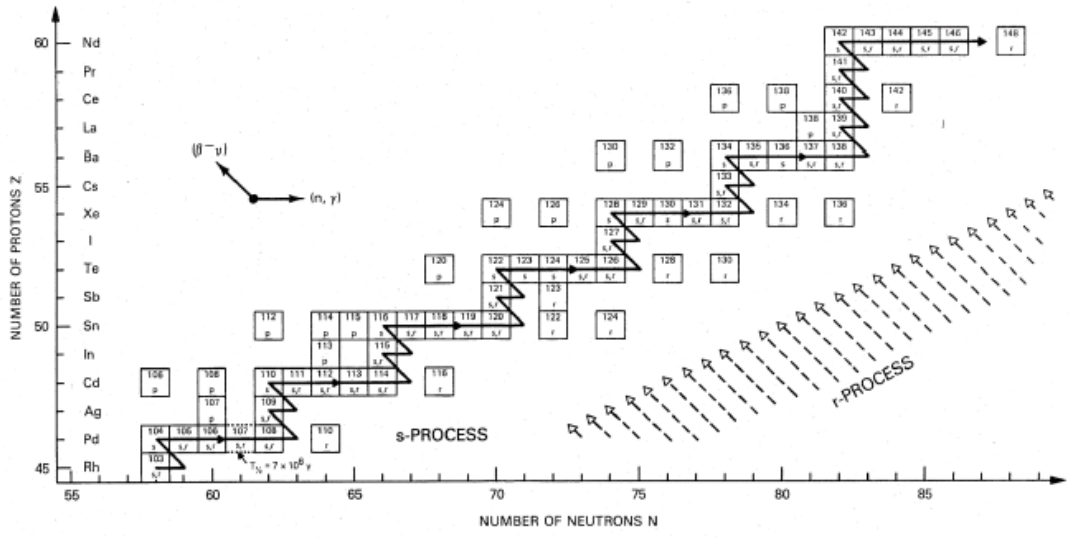

Figure 1.1: Chart of the nuclides showing the paths for the s-process and the r-process. Reprinted with permission from *Cauldrons in the Cosmos (1988)*.

^{64}Zn	^{96}Mo	^{124}Te	^{192}Pt	^{176}Lu
^{70}Ge	^{100}Ru	^{128}Xe	^{150}Sm	^{176}Hf
^{76}Se	^{104}Pd	^{130}Xe	^{152}Gd	^{186}Os
^{80}Kr	^{110}Cd	^{134}Ba	^{154}Gd	^{187}Os
^{82}Kr	^{116}Sn	^{136}Ba	^{160}Dy	^{198}Hg
^{86}Sr	^{122}Te	^{142}Nd	^{164}Er	^{204}Pb
^{87}Sr	^{123}Te	^{148}Sm	^{170}Yb	

Table 1.1: List of isotopes created only through the s-process. Adapted from [8].

1.2.1 Slow Neutron Capture Process (s-process)

The s-process mainly starts with Iron (^{56}Fe) as the seed nuclei for nucleosynthesis. In the s-process, the nucleosynthesis chain begins with ^{56}Fe and terminates with the production of ^{209}Bi. A brief description of the theory behind the s-process is detailed in this section. For a full description, please refer to Ref. [14].

There are 34 isotopes that are created only via the s-process (hereafter referred to as s-only isotopes). They are listed in Table 1.1. For a s-only isotope of mass number A which is not

radioactive, the time dependence of the abundance (N_A) is given as follows:

$$\frac{dN_A(t)}{dt} = N_n(t)N_{A-1}(t)\langle\sigma v\rangle_{A-1} - N_n(t)N_A(t)\langle\sigma v\rangle_A \tag{1.1}$$

Here, $< \sigma v >_A$ is the mean neutron capture rate per particle pair for isotope A and $N_n(t)$ is the number density of neutrons at time t. The first term describes the capture of a neutron by the predecessor $(A-1)$ to create isotope A, and the next term describes the destruction of A by neutron capture. Since the abundances of both A and $(A-1)$ depends mainly on the stellar temperature which depends on time, N_A and N_{A-1} are both time dependent. It is assumed in this case that the stellar temperature remains constant during the s-process.

Defining $\langle\sigma v\rangle = \langle\sigma\rangle v_T = \sigma_A v_T$ where v_T is the thermal velocity of the neutron and σ_A is the Maxwellian-averaged neutron capture cross section for A, Equation 1.1 becomes,

$$\frac{dN_A(t)}{dt} = v_T N_n(t)(\sigma_{A-1}N_{A-1} - \sigma_A N_A) \tag{1.2}$$

For a Maxwell-Boltzmann energy distribution for neutrons, the neutron flux $\phi(t)$ can be given by $\phi(t) = v_T N_n(t)$ neutrons cm^{-2} s^{-1}. Using this quantity, the time-integrated neutron flux τ in neutrons cm^{-2} can be written as follows:

$$\tau = \int_0^t \phi(t)dt = v_T \int_0^t N_n(t)dt \tag{1.3}$$

Using this result, Equation 1.2 can be written as follows where the abundance N_A is now expressed with respect to the time duration of neutron exposure τ.

$$\frac{dN_A}{d\tau} = N_{A-1}\langle\sigma\rangle_{A-1} - N_A\langle\sigma\rangle_A \tag{1.4}$$

Certain situations such as regions between magic neutron numbers have a tendency to reduce the difference between the terms $\langle\sigma\rangle_A N_A$ and $\langle\sigma\rangle_{A-1}N_{A-1}$, and reaches a state of equilibrium where $dN_A/d\tau = 0$. This is called a *local equilibrium approximation* where $\langle\sigma\rangle_A N_A =$

$\langle\sigma\rangle_{A-1}N_{A-1}$ = constant. At this point, for the abundance of s-only isotopes the rate of destruction equals the rate of production.

There are two principle neutron-source reactions that produces the neutrons for the s-process. They are namely the ^{13}C(α,n) and ^{22}Ne(α,n) reactions. Their roles in the s-process nucleosynthesis will be described in the next sections of this text.

1.2.1.1 Main component

The main neutron-source reaction in this component is the ^{13}C(α,n) reaction due to the low energy required for its activation. This component of the s-process is responsible for the formation of elements from strontium (Sr) and yttrium (Y) all the way up to lead (Pb), bismuth (Bi) and polonium (Po) in low metallicity stars. The production site for this component is low-mass (1.3 $M_\odot \leq M \leq 8\ M_\odot$) asymptotic giant branch stars (see Chapter 1.2.2) detailed in the next section.

$$^{12}C(p,\gamma)^{13}N(\beta^+\nu)^{13}C(p,\gamma)^{14}N \tag{1.5a}$$

$$^{14}N(\alpha,\gamma)^{18}F(\beta^+\nu)^{18}O(\alpha,\gamma)^{22}Ne \tag{1.5b}$$

It is assumed that protons mix with ^{12}C created via 3 ^{4}He $\rightarrow$ ^{12}C, the *"3α reaction"*, to create ^{13}C during the hydrogen burning phase of AGB stars. This leads to a reaction sequence that produces ^{14}N and ^{13}C through the reaction sequence in 1.5a shown above. When the temperature of the star increases to about $\sim$ 0.3 x 10^9 Kelvin (K) during the helium burning phase, the created ^{14}N is gradually converted through alpha and positron (β^+) captures into ^{22}Ne via the sequence 1.5b [8].

1.2.1.2 Weak component

Elements from iron up to strontium and yttrium are created through the weak s-process which takes place in massive stars ($M \geq 8\ M\odot$) at the end of their helium and Carbon burning phases [15]. This occurs with the ^{22}Ne(α,n) reaction as the main neutron source. This component is far

less understood compared with the main s-process. The yield of the weak s-process depends on the amount of ^{22}Ne present, which is in turn determined by the amount of ^{14}N in the star.

In these massive stars, the ^{22}Ne(α,n) reaction produces neutrons in two different stages [16]. The first is during the end of the core helium burning when the temperature is high enough to activate this reaction. In this stage, since the amount of neutrons created is relatively low, the s-process cannot overcome the closed neutron shell at N=50. Also at this stage, not all the ^{22}Ne created will be consumed by the helium burning. The second neutron exposure comes during the Carbon shell burning phase where the leftover ^{22}Ne will react with helium.

During the Carbon burning phase, the ^{12}C(^{12}C,p)^{23}Na reaction creates protons which can react with the ^{22}Ne via the ^{22}Ne(p,γ)^{23}Na reaction and act as a poison for the ^{22}Ne [15]. Nevertheless, it has been shown that the effectiveness of the ^{22}Ne(α,n) reaction during both core helium and Carbon burning phases are comparable [15, 17].

1.2.1.3 Branching of the s-process

Branching in the s-process path occurs when an unstable isotope with long half-lives are encountered where neutron capture competes with β-decay [18]. In this scenario, the isotope can either capture a neutron and create the next neutron-rich isotope or β-decay and continue along the valley of stability. The strengths of the branching point for neutron capture and β-decay is given by f_n and f_β respectively as in:

$$f_n = \frac{\lambda_n}{\lambda_\beta + \lambda_n} \quad \text{and} \quad f_\beta = \frac{\lambda_\beta}{\lambda_\beta + \lambda_n}$$

Here, $\lambda_\beta = 1/\tau$ is the β-decay rate for a mean lifetime τ, and λ_n is the neutron capture rate. Additionally, the β-decay lifetimes of certain isotopes can be affected by temperature and electron density variations of the immediate environment. The temperature dependence will be more complicated if these isotopes have an isomeric state which can be thermalized at higher temperatures. Isotopes (s-only) affected in the manner can be used as tools to obtain information about the physical conditions during the process, i.e., temperature, neutron density [19].

1.2.2 Asymptotic giant branch (AGB) stars for the s-process

It was proposed [20, 21] that the helium-burning shell of thermally pulsing red giant stars are the main sites of the s-process. This evolutionary phase of stars in particular are the asymptotic giant branch (AGB) stars, which is the last stage of burning for stars with initial mass between $\sim$ 0.8 - 8 $M_{\odot}$.

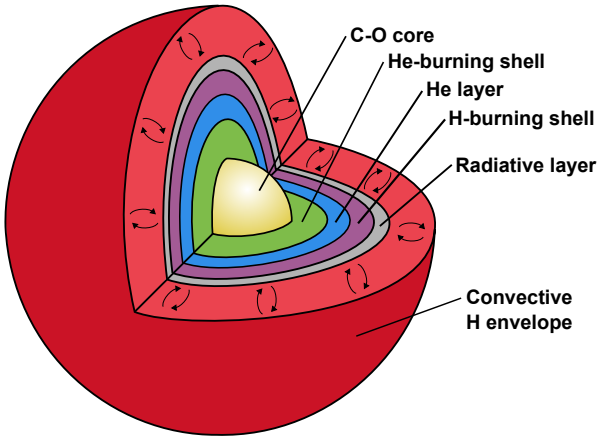

Figure 1.2: Schematic view of the internal structure of an AGB star. Adapted from [1]

At the base of the AGB phase, all the helium in the core of the star is exhausted, and the star begins to produce energy by burning helium in a shell that surrounds the inert, electron-degenerate carbon and oxygen (C-O) core, and by the release of energy from the gravitationally-collapsing core. During this rapid early-AGB phase, the hydrogen-burning shell will remain inactive due to the expansion and cooling of the star from the energy output of the helium-burning shell, which leads to a mixing of different layers. Once this early-AGB phase is complete, hydrogen shell will ignite and become the dominant energy source of the star for a long period of time ($\sim 10^4$ years) while the growing helium shell remains inactive. At this point, these stars have a specific interior structure shown in Figure 1.2. They consist of an inert C-O core, then a helium-burning shell, a helium inter-shell, and finally a hydrogen-burning shell which is composed of an inner radiative

shell and an outer convective shell, respectfully.

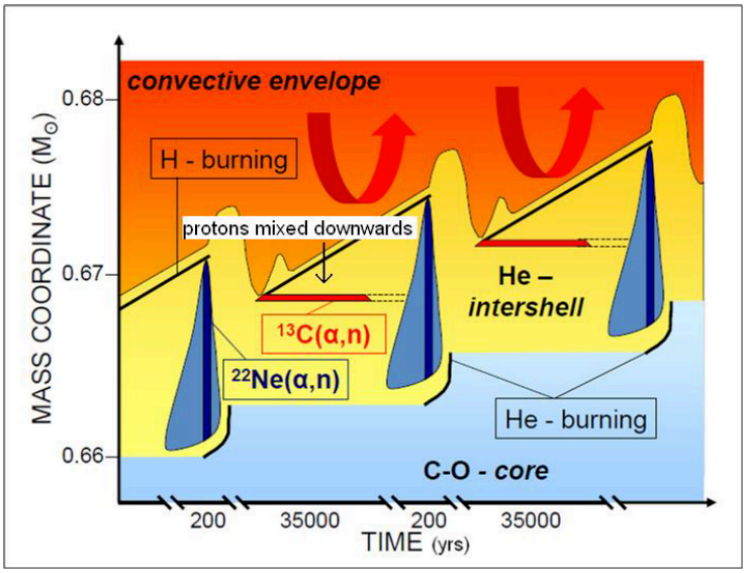

Figure 1.3: Schematic view of the time evolution of an low mass AGB star in the He-intershell. [2]

During hydrogen burning, the amount of matter in the helium inter-shell will be continuously increasing, increasing its temperature and density. At some point, the helium will start to burn for a short period of time ($\sim$ few 100s of years) at the bottom of the helium inter-shell. This leads to a thermal pulse where an enormous amount of energy is produced which in turn deactivates the hydrogen burning. During this thermal pulse, a convective zone will be created in the helium inter-shell (Figure 1.3), which mixes the ashes from the helium-burning shell with the inter-shell. This phase is known as the thermally-pulsing AGB (TP-AGB) phase. During a thermal pulse, a radiative layer is created between the helium inter-shell and the convective envelope. This layer causes the sudden expansion and cooling of the convective envelope, which causes the bottom of the envelope to move into the helium shell and mix with the material produced by helium-burning and the s-process, and thus removing these material from the interior of the star. The thermal pulses are caused mainly due to the strong temperature dependence of the helium burning shell combined with the high temperatures in the stellar interior.

There is a large amount of evidence for the presence of the s-process from observational astronomy. S-process elements have been observed on the surface of some of the most luminous portion of AGB stars called the *S-type stars*. Visual spectra of these S-type stars depict clear features related to s-process isotopes such as spectral lines due to yttrium oxide (YO), strontium (Sr), barium (Ba) and lanthanum oxide (LaO) present in the surface [22]. Several S-type stars have also shown evidence of technetium (Tc) which results from s-process neutron capture [23].

1.2.3 Neutron poisons for the s-process

Neutron poisons for the s-process mainly concerning the ^{22}Ne(α,n) reaction will be discussed in this section.

The product of ^{22}Ne+α, ^{26}Mg, has the neutron decay threshold located at 11.093 MeV, while the alpha-decay threshold is at 10.614 MeV. Hence, the resonances relevant for the ^{22}Ne(α,n)^{25}Mg reaction will be affected by the ^{22}Ne(α,γ) reaction which will compete for the amount of ^{22}Ne in the stellar environment. A *Q-value* of a nuclear reactions is a measure of the amount of energy absorbed (negative Q-value) or released (positive Q-value) during the reaction. Due to the positive Q-value for the ^{22}Ne(α,γ) reaction (+10.614 MeV) compared with the ^{22}Ne(α,n) reaction (-0.478 MeV), the former reaction will continue to burn throughout the helium-burning phase even at low stellar temperatures, reducing the amount of ^{22}Ne that can participate in the production of neutrons. Hence the ^{22}Ne(α,γ) reaction is called a *neutron poison*. The competition between these two reactions during the thermal pulse of an AGB star will affect the neutron production for the s-process.

Another important neutron poison is the ^{14}N created as a product of the hydrogen-burning in the CNO cycles (Equations 1.5a and 1.5b) and also present from the primordial abundance of the star. ^{14}N has a high cross section for absorption of neutrons through the ^{14}N(n,p)^{14}C reaction (Q = +0.63 MeV). This reaction can also affect the yield of ^{22}Ne produced by reducing the amount of ^{14}N for alpha capture.

The yield of ^{18}O created from the burning of ^{14}N also plays a role in the yield of ^{22}Ne. The yield of ^{18}O depends on the relative rates of the ^{18}O(α,n)^{21}Ne reaction (Q = -0.697 MeV) and

the ^{18}O(α,γ)^{22}Ne reaction (Q = +9.67 MeV). Due to these Q-values, the temperature of the star determines the manner of burning for ^{18}O, i.e., and neutron-producing reaction will occur at high temperatures creating ^{21}Ne and at low temperatures the main product will be ^{22}Ne.

In some occasions, the ^{22}Ne(α,n)^{25}Mg reaction can act as a self-poisoning reaction due to the high neutron capture cross section of ^{25}Mg. Hence, the ^{25}Mg(n,γ)^{26}Mg reaction is also a neutron poison.

1.3 Significance of ^{26}Mg for the ^{22}Ne(α,n)^{25}Mg and ^{22}Ne(α,γ)^{26}Mg reactions

Out of the two main neutron-source reactions for the s-process, the ^{22}Ne(α,n) reaction affects the s-only isotopes near the branching points as compared with the ^{12}C(α,n) reaction which determines the overall shape of the main component. The main focus of this study will be the effect of the ^{22}Ne(α,n) reaction in stellar environments.

The negative Q-value of the ^{22}Ne(α,n) reaction (Q = -0.478 MeV) requires high temperatures for activation (around T $\geq$ 0.3 GK). The energy region of interest for astrophysics of this reaction lies around $\sim$400 - 800 keV in centre-of-mass energies. Since this reaction competes with the ^{22}Ne(α,γ) radiative alpha-capture reaction, it is imperative to constrain the (α,n) and (α,γ) reaction rates to accurately determine the contribution of the ^{22}Ne(α,n) as a neutron source for the s-process.

Neutron production for the s-process occurring with alpha-capture on ^{22}Ne occurs through the resonances in the ^{26}Mg nucleus. The main focus of this dissertation is the study of these resonance levels of ^{26}Mg contributing to the ^{22}Ne(α,n) reaction rate.

An alpha particle is a cluster of two protons and two neutrons bound together in a closed-shell configuration. This makes an alpha particle relatively stable within a nucleus consisting of an even number of protons and neutrons (even-even nuclei). This effect can be seen in nuclei such as ^{8}Be, ^{12}C [24] and ^{16}O which have two, three and four alpha-cluster configurations respectively. Such nuclei can be characterized with states that have large alpha decay widths. ^{26}Mg also exhibits a similarly dominant alpha-cluster structure with large alpha spectroscopic factors for some states. This effect can also be seen in resonances close to the alpha-decay threshold in nearby nuclei to ^{26}Mg such as ^{18}O [25].

Several direct α-capture measurements have been performed in the past to study the ^{22}Ne(α,n) and ^{22}Ne(α,γ) reactions [4, 26, 27, 28, 29, 30, 31, 32]. The direct study of these reactions at energies relevant for astrophysics is difficult due to the presence of the Coulomb barrier preventing alpha-particles from penetrating into the ^{22}Ne nucleus at such low energies, and experimental measurements are limited to alpha energies above $\sim$ 800 keV. Obtaining an upper limit for the resonances of ^{26}Mg in the region of interest have been attempted using various extrapolation methods using direct/indirect measurements at higher energies.

Within the energy region of interest for this reaction, ^{26}Mg has an extremely high level density (a few tens of levels per 100 keV) [33] which can be challenging for experimental techniques. Only the natural parity states of ^{26}Mg should be of interest due to $J^{\pi} = 0^{+}$ for both alpha and ^{22}Ne. The biggest uncertainty lies in the fact that the spin-parity assignments and the energies of all the resonances of ^{26}Mg within the energy region of interest are not well known as of the time of the writing.

An extensive amount of research has been done to study the levels of ^{26}Mg in order to better understand the effect of the levels ^{26}Mg for the ^{22}Ne(α,n) and ^{22}Ne(α,γ) reactions. 1) Neutron capture studies on ^{25}Mg (reactions such as ^{25}Mg(n,γ)^{26}Mg and ^{25}Mg(n,tot)) [34, 35, 36], 2) ^{26}Mg(p,p')^{26}Mg [37, 38], 3) ^{26}Mg(d,d')^{26}Mg measurements [38], and 4) ^{26}Mg(α,α')^{26}Mg measurements [6, 39] have been performed previously to obtain data on the resonance energies of ^{26}Mg. ^{26}Mg(γ,γ')^{26}Mg measurements [40, 41, 42] have also been performed using polarized and unpolarized γ rays in order to obtain information on the spin-parities of the levels of ^{26}Mg.

The work presented in this dissertation aims to reduce the uncertainties regarding the two ^{22}Ne(α,n)^{25}Mg and ^{22}Ne(α,γ)^{26}Mg reaction rates.

2. ALPHA-CAPTURE REACTIONS AT SUB-COULOMB ENERGIES

2.1 Motivation

Helium is the second most abundant element in the Universe. Hence, there are many alpha-capture reactions such as (α,p), (α,γ) and (α,n) that takes place in various astrophysical sites. The study of these various reactions can help towards understanding the chemical abundances in the Universe. The nucleosynthesis rates that define the chemical abundances of isotopes created through the s-process are mainly determined by the α-cluster states near the α-threshold of the different nuclei involved. However, the cross sections for these reactions are suppressed due to the Coulomb barrier between the charged particles. The energy range at which the reaction proceeds with highest probability in the given astrophysical environment is defined as the "*Gamow energy window*" (Figure 2.1), named after Soviet-American Physicist George Gamow (1904-1968). Depending on the temperature of the star, this energy window defines the region where the cross section of a nuclear reaction is significantly high. This is a convolution of two factors. First, the probability of a particle penetrating the Coulomb barrier increases with the particle energy which is parameterized by the transmission probability P. Second, the probability of a particle having a high energy, and therefore a high velocity, at a given stellar temperature decreases rapidly with increasing energy, which is given by the Maxwell-Boltzmann energy distribution ($\phi(v)$) [43]. These two quantities are depicted in the equations below.

$$P = \exp(-2\pi\eta) = \exp\Big(-2\pi\frac{Z_1 Z_2 e^2}{(\hbar\nu)}\Big) = \exp\Big(-2\pi\frac{Z_1 Z_2 e^2}{\hbar}\sqrt{\frac{\mu}{2E}}\Big) \tag{2.1}$$

$$\phi(v) = 4\pi v^2\Big(\frac{\mu}{2\pi k_B T}\Big)^{\frac{3}{2}}\exp\Big(-\frac{\mu v^2}{2k_B T}\Big) \propto E\exp\Big(-\frac{E}{k_B T}\Big) \tag{2.2}$$

Here, μ is the reduced mass of the system of particles with atomic numbers Z_1 and Z_2, and k_B is the Boltzmann constant. Equation 2.2 is the velocity distribution of the particles in an environment with temperature T. The maximum of the Gamow peak (E_0) is given by the derivative below using

the exponential terms in the above two equations:

$$\frac{d}{dE}\Big(- 2\pi\frac{Z_1 Z_2 e^2}{\hbar}\sqrt{\frac{\mu}{2E}} - \frac{E}{k_B T}\Big)_{E=E_0} = \frac{\pi}{\hbar} Z_1 Z_2 e^2 \sqrt{\frac{\mu}{2E_0^3}} - \frac{1}{k_B T} = 0 \tag{2.3}$$

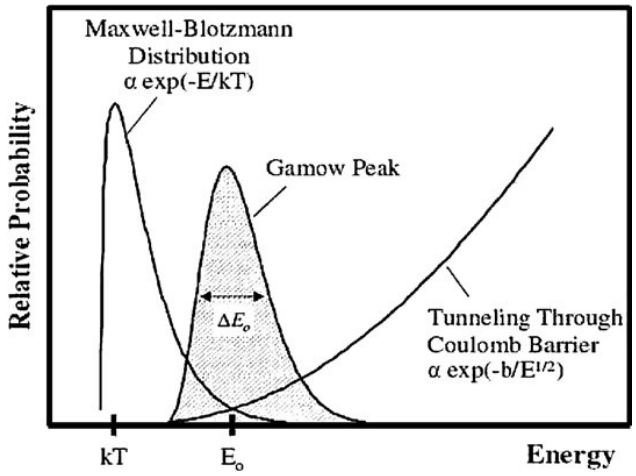

Figure 2.1: Schematic representation of the Gamow energy window for a particle of energy E. The Gamow energy window is a convolution between the Maxwell-Boltzmann energy distribution and the Coulomb barrier penetration probability. Reprinted with permission from *Cauldrons in the Cosmos (1988)*.

In Figure 2.1 from Ref. [14], E_0 is the maximum of the Gamow window given by $E_0 = 1.22\mu^{1/3}(Z_1 Z_2 T_6)^{2/3}$ keV where T_6 is the stellar temperature in mega Kelvin (MK). The width of the peak is given by $\Delta E_0 = 0.749(Z_1^2 Z_2^2 \mu T_6^5)^{1/6}$ keV.

For many reactions relevant for nuclear astrophysics, the Gamow energy window lies at very low energies and has small cross sections, which makes it near impossible to replicate them in laboratory environments. In order to study these reactions, much work has been done where the cross sections are measured at higher energies and extrapolated into the energy region of interest. This method produces significant uncertainties in the reaction rate calculations for stellar temperatures. In order to reduce these uncertainties arising from the extrapolations, the use of transfer reactions are becoming more prominent at the present.

2.2 Reaction rate and the Astrophysical S-Factor

For nuclear reactions relevant for astrophysics, the rates of these reactions play a dominant role in describing the abundances of the chemical elements in the Universe. These reaction rates are highly dependent upon the reaction cross section and the temperature of the environment. The reaction cross sections $\sigma(E)$ are only dependent on the relative energy between two interacting particles.

Using the velocity distribution from Equation 2.2 and the cross section $\sigma(E)$, the averaged reaction rate can be defined as,

$$\begin{aligned} N_A\langle\sigma v\rangle &= \int_0^\infty \sigma(E)\phi(v)v dv \\ &= \sqrt{\frac{8}{\pi\mu}}\frac{N_A}{(k_BT)^{3/2}}\int_0^\infty E\sigma(E)\text{exp}\Big(-\frac{E}{k_BT}\Big)dE \end{aligned} \tag{2.4}$$

The integrand of Equation 2.4, $E\sigma(E)\text{exp}(-E/k_BT)$ is called the *Gamow distribution function*, which is used to find the peak of the Gamow energy window described previously.

$$\sigma(E) = \frac{1}{E}e^{-2\pi\eta}S(E) \tag{2.5}$$

The reaction cross section $\sigma(E)$ drops exponentially with the decrease of the center-of-mass energy E due to the repulsion arising from the Coulomb barrier; $\sigma(E) \propto e^{-2\pi\eta}$ where $\eta = Z_1Z_2e^2/hv$ is the *Sommerfield parameter* where v is the relative incident velocity and $Z_1Z_2e^2$ is the product of the charges of the two particles. The cross section is also inversely proportional to the energy E, $\sigma(E) \propto 1/E$. These energy dependences can be factored out by using the *Astrophysical S-Factor S(E)* (see Figure 2.2 from Ref. [14]). This S-factor is a smoothly varying function of energy (see Equation 2.5) and contains all the reaction physics. Hence, the S-Factor is much more useful than the cross section when extrapolating to astrophysical energies.

In Equation 2.5, the exponent depicts the Coulomb barrier penetrability. Whereas the reaction

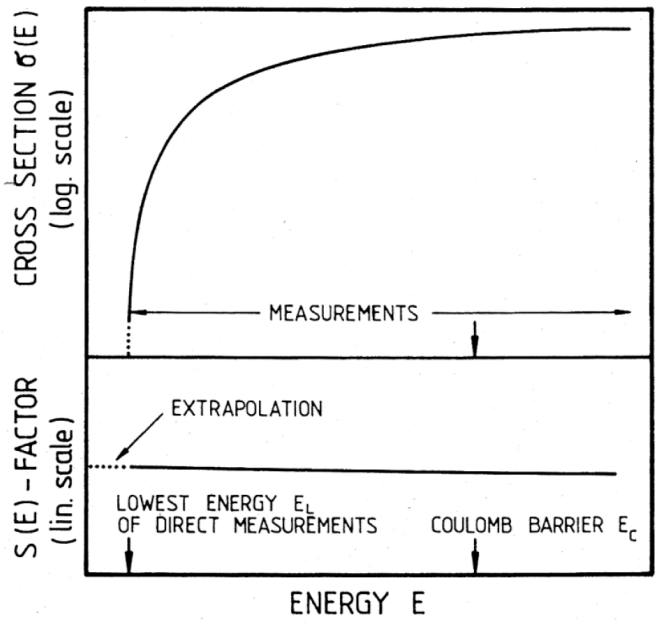

Figure 2.2: Dependence of the cross section and S-factor on the energy E. Reprinted with permission from *Cauldrons in the Cosmos (1988)*.

cross section decreases exponentially with energy, the variations of the astrophysical S-factor is minimal. For very low reaction cross sections at extremely low energies, it is much more common to find $S(E)$ over a range of available energies and then to extrapolate down to the energies of interest, which has significant errors involved, which will be described in a later section.

2.3 Distorted-Wave Born Approximation

The Distorted-Wave Born Approximation (DWBA) is a common formalism used to obtain inelastic and transfer reaction cross sections. The DWBA uses the optical model (described in detail the Section 2.4) to describe the relative motions of the particles involved in a particular reaction. Here the interaction between different nuclei during the transfer or inelastic excitation is considered as a perturbation to the optical potentials modeling the system. More information can be found in [44, 45].

Consider a projectile nucleus $A = a + x$ scattering on a target nucleus b. Once the particle x has been transferred to b, the final system would be $B = b + x$ (See Figure 2.3). Here, a and b are

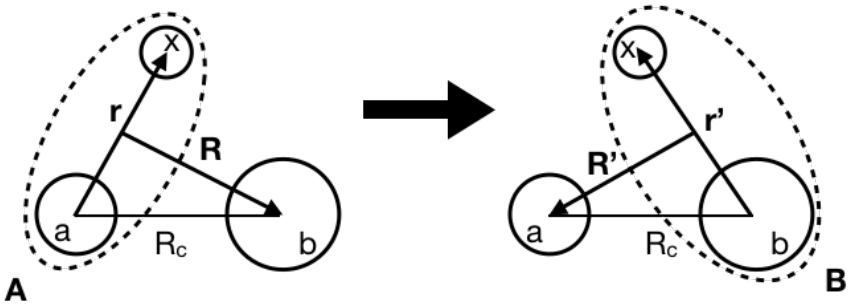

Figure 2.3: Transfer reaction scheme for A + b = a + B reaction.

referred to as the *core*, and x is the *valence particle*. The bound states / internal wave functions of the nuclei A and B, ϕ_A and ϕ_B, are described by the internal Hamiltonians H_A and H_B. In Figure 2.3 and all the following equations, **r**, **r'**, **R** and **R'** are three dimensional vectors.

$$[H_A - \epsilon_A]\phi_A(\mathbf{r}) = [T_r - V_{ax}(\mathbf{r}) - \epsilon_A]\phi_A(\mathbf{r}) = 0 \tag{2.6a}$$

$$[H_B - \epsilon_B]\phi_B(\mathbf{r'}) = [T_{\mathbf{r'}} - V_{bx}(\mathbf{r'}) - \epsilon_B]\phi_B(\mathbf{r'}) = 0 \tag{2.6b}$$

In the above equations, ϵ_A and ϵ_B are the internal energies of the A and B systems, T is the kinetic energy and V is the potential energy. The total Hamiltonian for the transfer reaction can be described in two different forms, *prior* and *post*, which depends on whether the initial $(A + b)$ or final $(a + B)$ mass partition were chosen.

$$H_{prior} = T_R + U_{Ab}(\mathbf{R}) + H_A(\mathbf{r}) + \mathcal{V}_{prior}(\mathbf{r}, \mathbf{R}) \tag{2.7a}$$

$$H_{post} = T_{R'} + U_{aB}(\mathbf{R'}) + H_B(\mathbf{r'}) + \mathcal{V}_{post}(\mathbf{r'}, \mathbf{R'}) \tag{2.7b}$$

U_{Ab}, U_{aB} are the diagonal potentials of the entrance and exit channels, and $\mathcal{V}_{prior}$, $\mathcal{V}_{post}$ are the *interaction terms* or *transition potentials* for the prior and post forms. They can be further

described as follows:

$$\mathcal{V}_{prior}(r, R) = V_{bx}(\mathbf{r'}) + [U_{ab}(R_c) - U_{Ab}(\mathbf{R})] \approx V_{bx}(\mathbf{r'}) \tag{2.8a}$$

$$\mathcal{V}_{post}(\mathbf{r'}, R') = V_{ax}(\mathbf{r}) + [U_{ab}(R_c) - U_{aB}(\mathbf{R'})] \approx V_{ax}(\mathbf{r}) \tag{2.8b}$$

Here, the terms in the brackets are called the *remnant terms* and the V_{ax}, V_{bx} are the *binding potentials* which are usually described by real-valued optical potentials. $U_{ab}(R_c)$ is the potential describing the scattering between the a and b cores, which is described by real and imaginary potentials. $U_{Ab}(\mathbf{R})$ and $U_{aB}(\mathbf{R'})$ are the potentials describing the elastic scattering between the nuclei in the entrance and exit channels, respectively. These are generally complex optical potentials. In Eq. 2.8a, the approximation is valid if the core a and the target A are typically heavier than the transferred particle x. In Eq. 2.8b, the approximation is true if the target A and the target-like fragment B are similar. In cases where the full remnants are considered, the same results should be obtained by the *prior* and *post* forms.

Using the above transition potentials, the *Transition Amplitude* can be written as follows for the *prior* or *post* forms:

$$T^{\text{DWBA}}_{prior} = \langle \chi^{(-)}_{\beta} \phi_a \phi_B | \mathcal{V}_{prior} | \chi^{(+)}_{\alpha} \phi_A \phi_b \rangle \tag{2.9a}$$

$$T^{\text{DWBA}}_{post} = \langle \chi^{(-)}_{\beta} \phi_a \phi_B | \mathcal{V}_{post} | \chi^{(+)}_{\alpha} \phi_A \phi_b \rangle \tag{2.9b}$$

Here, α and β refers to the entrance and exit channels, respectively. The plus and minus signs denote the incoming and outgoing wave functions of the χ *distorted waves*. ϕ_A is also described as an *overlap functions* between a and x, and similarly for ϕ_B between b and x. The distorted waves are generated by solving Schrodinger's equation using an optical potential obtained through fittings for the relevant elastic scattering cross sections.

The theoretical DWBA cross sections can then be described using this transition amplitude, the

reduced masses $\mu_{\alpha,\beta}$ and the wave number $k_{\alpha,\beta}$, as

$$\left(\frac{d\sigma}{d\Omega}\right)_{\text{DWBA}} = \frac{\mu_\alpha \mu_\beta}{\left(2\pi\hbar^2\right)^2} \frac{k_\beta}{k_\alpha} |T(k_\beta, k_\alpha)|^2 \tag{2.10}$$

Consider the overlap function of the composite particle A (ϕ_A). This overlap function can be described using the orbital angular momentum l and intrinsic spin s of the valence particle x coupled with total angular momentum j to the core a with an intrinsic spin I_a.

$$\phi_A(\mathbf{r}) = \sum_{I_a,lsj} A_{lsj}^{JI_aI_A} \frac{u_{nl}(r)}{r} \left[\left[Y_l(\mathbf{r}) \otimes \chi_s\right]_j \otimes \phi_{I_a}\right]_{I_A} \tag{2.11}$$

Equation 2.11 shows the overlap function ϕ_A where J is the total angular momentum of the composite particle A, $u_{nl}(r)$ is the single-particle wave function normalized to unity and n is the number of radial nodes of the overlap wave function. Here, $A_{lsj}^{JI_aI_A}$ is called the *Spectroscopic Amplitude*, the square modulus of which is called the *Spectroscopic factor* (S),

$$S_{lsj}^{JI_aI_A} = |A_{lsj}^{JI_aI_A}|^2 \tag{2.12}$$

The spectroscopic factor can also be described as the probability of finding the core state I_a within a composite state I_A when removing a nucleon in a state lsj due to the relation,

$$\sum_{Ilsj} |A_{lsj}^{JI_aI_A}|^2 = \sum_{Ilsj} S_{lsj}^{JI_aI_A} = 1 \tag{2.13}$$

2.4 The Optical Model

The behavior of one particle interacting with another beam of particles can be considered to be analogous to the behavior of light and an optical lens, where the light could be partially absorbed by the lens, partially scattered and partially transmitted. Hence, the "Optical Model" is more commonly used to model the interaction between particles in nuclear reactions. In order to calculate the distorted waves described in the previous section, various optical potentials are used for this

model. A brief description of the potentials used for the optical model is described in this section. For additional information please refer to [44].

The most widely used form for the optical model potential is,

$$U(r) = -Vf(r, R, a) - iWf(r, R', a') - iW_D g(r, R', a') \tag{2.14}$$

where W_D is the imaginary surface potential depth and f is the Woods-Saxon form factor defined for the real (V) and imaginary (W) terms for a particle with radius R and diffusivity a as,

$$f_i(r, R_i, a_i) = \frac{1}{1 + e^{\left(\frac{r-R_i}{a_i}\right)}} \text{ for } i = V, W \tag{2.15}$$

The radius R of a nucleus is given by $R = r_0 A^{1/3}$ where A is the nuclear mass number and r_0 is the reduced radius. The second imaginary potential in Equation 2.14 is peaked at the nuclear surface and is the derivative of the first term.

$$g_i(r, R_i', a_i') = 4a\frac{d}{dr} f_i(r, R_i', a_i') \tag{2.16}$$

The Wood-Saxon form factor can be thought of as a smoothed out step function, where $f(r = 0) \approx 1$ and $f(r = R) = 0.5$. Also f falls from 9/10 to 1/10 over a distance of $4.4a$ centered at $r = R$.

Additionally, if the particles involved have spin, a spin-orbit term may also be added to the list of potentials. Specifically for the spin-orbit potential, the derivative of the Wood-Saxon form factor, $g_{so}(r)$, can be substituted with the "Thomas" form where $g_{so}(r) = r^{-1}(d/dr)f(r, R_{so}, a_{so})$ [46]. An expansion of Equation 2.14 including a full list of the most commonly used potentials are shown below in Equation 2.17.

$$
\begin{aligned}
U(r) = & \\
& + V_c(r) \qquad \text{(a Coulomb term)}, \\
& - V_R f_R(r) \qquad \text{(a real volume term)}, \\
& - iW_S f_S(r) \qquad \text{(an imaginary volume term)}, \\
& + 4a_D V_D \frac{df_D(r)}{dr} \qquad \text{(a real surface term)}, \\
& + i4a_D W_D \frac{df_D(r)}{dr} \qquad \text{(an imaginary surface term)}, \\
& + V_{so}\Big(\frac{\hbar}{m_\pi c}\Big)^2 g_{so}(r)(\vec{l}.\vec{s}) \qquad \text{(a real spin-orbit term)}, \\
& + iW_{so}\Big(\frac{\hbar}{m_\pi c}\Big)^2 g_{so}(r)(\vec{l}.\vec{s}) \qquad \text{(an imaginary spin-orbit term)}
\end{aligned}
\tag{2.17}
$$

Here, the subscript 'S' is used for the imaginary volume term, 'D' denotes the surface terms, and so denotes the spin-orbit component. The Coulomb potential is usually approximated by two different forms depending on which radius range is being considered. This is shown in Equation 2.18.

$$
V_c(r) = \begin{cases} \frac{Z_1 Z_2 e^2}{2R_c}\Big(3 - \frac{r^2}{R_c^2}\Big) & \text{for } r \leq R_c \\ \frac{Z_1 Z_2 e^2}{r} & \text{for } r > R_c \end{cases} \tag{2.18}
$$

Here, Z_1 and Z_2 are the charges of the interacting nuclei and with an inter-nuclei distance of r, and R_c is the Coulomb radius. For charged particles with angular momentum higher than $l = 0$, the centrifugal barrier also has to be overcome for a reaction to occur. This is given by,

$$
V_{cf}(r) = \frac{l(l+1)\hbar^2}{2\mu r}. \tag{2.19}
$$

2.5 Partial widths of astrophysically-relevant resonances

For a particle transfer reaction, the experimental and DWBA cross sections are related via the *Spectroscopic factor (S)* for the entrance and exit channels. This relation is shown in Equation 2.20. The spectroscopic factor is a measure of how much the populated resonance resembles a "single-particle" shell-model state [47].

$$\Big(\frac{d\sigma}{d\Omega}\Big)_{exp} = S_\alpha S_\beta \Big(\frac{d\sigma}{d\Omega}\Big)_{DWBA} \tag{2.20}$$

In order to study transfer reactions in this manner, the spectroscopic factor of either the entrance or exit channel must be known prior to experimental measurements. The partial width of the state for the transferred particle (Γ_x) is related to the spectroscopic factor by the *single particle width* Γ_{sp} as follows:

$$\Gamma_x = S_x \Gamma_{sp} \tag{2.21}$$

The single particle widths are calculated using the wave function obtained by solving the time-independent Schrodinger Equation with a potential described by correct optical model potentials. It has been shown that the product of S_x and Γ_{sp} in this manner is quite insensitive to the bound-state parameters due to the fact that the same wave functions are used to calculate both quantities [48]. Γ_{sp} denotes the partial width of a single-particle resonance located at the same energy as the resonance of interest and provides a measure of the maximum decay width based on the probability of the Coulomb barrier penetration [49]. The method of obtaining the single-particle width is briefly described below. For further information, please refer to *Nuclear Reactions for Astrophysics* [43].

$$\Big[\frac{\hbar^2}{2\mu}\Big(-\frac{1}{R^2}\frac{\partial}{\partial R}(R^2\frac{\partial}{\partial R}) + \frac{\hat{L}^2}{R^2}\Big) + V(R) - E\Big]\psi(R,\theta,\phi) = 0 \tag{2.22}$$

The time-independent Schrodinger equation can be written as above using spherical coordi-

nates (R, θ, ϕ) for a spherically symmetric potential $V(R)$, and squared angular momentum operator $\hat{L}^2$. Choosing the z-axis as the beam direction simplifies this equation to be independent of the coordinate ϕ, and thus simplifying the scattering wave function to $\psi(R, \theta)$. Using boundary conditions for a smooth wave function at all radial distances, the wave function can be written as follows.

$$\psi(R, \theta) = e^{ikz} + f(\theta)\frac{e^{ikR}}{R} \tag{2.23}$$

In the above equation, $f(\theta)$ is called the *scattering amplitude* which gives the differential cross section $d\sigma/d\Omega = |f(\theta)|^2$ of a nuclear reaction. This wave function can be expanded using Legendre polynomials $P_L(cos\theta)$ using a partial-wave expansion.

$$\psi(R, \theta) = \sum_{L=0}^{\infty}(2L+1)i^L P_L(cos\theta)\frac{1}{kR}\chi_L(R) \tag{2.24}$$

where the partial waves $\chi_L(R)$ satisfies the partial-wave equation given below.

$$\Big[-\frac{\hbar^2}{2\mu}\Big(\frac{d^2}{dR^2} - \frac{L(L+1)}{R^2}\Big) + V(R) - E\Big]\chi_L(R) = 0 \tag{2.25}$$

The scattering amplitude can then be derived using the expanded wave function given in Equation 2.24 using a *phase shift* δ_L for each partial wave:

$$f(\theta) = \frac{1}{k}\sum_{L=0}^{\infty}(2L+1)P_L(cos\theta)e^{i\delta_L}\text{sin}(\delta_L) \tag{2.26}$$

Most excitation functions (cross sections $\sigma(E)$ plotted as a function of energy E) often show peaks or dips caused by resonances, which are a result of a sudden increase in the phase shift $\delta(E)$ [43]. This phase shift can be defined using the width (Γ) and the energy (E_R) of the resonance:

$$\delta(E) = \tan^{-1}\Big(\frac{\Gamma/2}{E_R - E}\Big) \tag{2.27}$$

The reaction cross section $\sigma(E)$ can then be simplified using the phase shift as follows.

$$\sigma(E) \simeq \frac{4\pi}{k}(2L+1)\text{sin}^2\delta(E) \tag{2.28a}$$

$$= \frac{4\pi}{k}(2L+1)\frac{(\Gamma/2)^2}{(E_R-E)^2+(\Gamma/2)^2} \tag{2.28b}$$

It can be seen from Equation 2.28b that the cross section $\sigma(E)$ peaks at $E \sim E_R$ with a full-width at half maximum (FWHM) equal to Γ for the resonance if the width is independent of energy. In all realistic cases, $\Gamma = \Gamma(E)$, with Γ increasing with energy due to the decrease of the potential barrier with energy. A resonance of the form of Equation 2.28b is called a *pure Breit-Wigner resonance* [50]. The single-particle width Γ_{sp} of a resonance is then defined as the difference between the two energy points where $\text{sin}^2\delta$ = 1/2, i.e., δ = 45° and 135° [51]. The single-particle width denotes the width of a single-particle resonance located at energy E_R. It also provides information about the maximum decay width based on the barrier penetration probability [49].

2.6 Sub-Coulomb alpha-transfer measurements

As mentioned in the previous chapter, since ^{4}He is the second most abundant element in the Universe, alpha-capture reactions play a dominant role in nuclear astrophysics. In order to study the relevant nuclear reactions at astrophysical energies, the methods used until recently have been to measure the cross sections and astrophysical S-factors at higher energies and then to extrapolate the results down to the energies of interest. This method provides significant disadvantages since the extrapolation of the cross sections inflict a large uncertainty on the reaction rates. The disadvantage has led to the development of indirect techniques to study these nuclear reactions. Some of these indirect techniques used are to extract the Asymptotic Normalization Coefficients (ANCs) of the relevant states, the Trojan Horse Method (THM) [52], the Coulomb Dissociation method, to name a few. The ANC technique was first introduced by Tribble, Gagliardi and Mukhamedzhanov from Texas A&M University in 1994 [53], and initially used to study (p,γ) reactions. This ANC

technique is used to study the ^{22}Ne(α, n)^{25}Mg reaction in this thesis.

The use of the ANC technique for α-capture reactions was handicapped due to uncertainties in optical model parameters needed for the theoretical analysis. In order to reduced the dependence of the results on the optical model parameters, it was suggested to use the ANC technique in combination with an alpha transfer reaction performed at sub-Coulomb energies (in both the entrance and exit channels), which was first introduced by C. Brune [54] to study the ^{12}C(α,γ)^{16}O reaction. More measurements have been performed since then using (^{6}Li,d) α-transfer reactions at energies close to the Coulomb barrier [55, 56, 57]. It has been demonstrated that this approach produces reliable results in determining the partial α-width for the near α-threshold resonances [55].

2.7 The study of the ^{22}Ne(α,n)^{25}Mg reaction using ^{22}Ne(^{6}Li,d)^{26}Mg.

Direct measurements of ^{22}Ne(α,n)^{25}Mg reaction at such low centre-of-mass energies is difficult to carry out due to the very low reaction cross section due to the Coulomb barrier and relatively high cosmic gamma-ray background. The lowest observed resonance of the compound nucleus ^{26}Mg of the ^{22}Ne+α system is located at $\sim$ 832 keV [4], which is at the higher end of the astrophysical energy region of interest. Following the success of using a (^{6}Li,d) α-transfer reaction to study the near α-threshold resonances, we use the same technique to study the ^{22}Ne(α,n)^{25}Mg reaction by using the ^{22}Ne(^{6}Li,d)^{26}Mg reaction to study the resonances of ^{26}Mg within the Gamow energy window that are relevant to the ^{22}Ne(α,n)^{25}Mg and the ^{22}Ne(α,γ)^{26}Mg reactions.

2.8 Asymptotic Normalization Coefficient (ANC)

The main technique used in this study is the measure of the ANCs for the resonances that are relevant for the astrophysical reaction rate. The brief description regarding the equations relevant for this technique is given in this section. Further information on this topic can be found in Refs. [58] and [59].

For the system described in Section 2.3 of A + $b \rightarrow B$ + a, consider a virtual decay of A in the form of $A \rightarrow a + x$ for a 'core' of a and a 'valence' particle x (similarly for $B \rightarrow b + x$). The overlap functions ($I^{B}_{ax}(r)$) for the particles involved in this virtual decay can then be expressed

using the wave functions $\phi_b(\xi_b)$ and $\phi_B(\xi_b, \mathbf{r})$, where ξ_b is the internal coordinate of b, and $\mathbf{r}$ is the relative motion coordinate of the center of mass.

$$I^A_{ax}(r) = \langle \phi_a(\xi_a) | \phi_A(\xi_a, \mathbf{r}) \rangle \tag{2.29}$$

Direct capture reactions at astrophysical energies involve the capture of a particle through the tail of the nuclear overlap function. The asymptotic behavior of the overlap function can then be approximated using the ANC (C) and the *Whittaker function (W)* found for a particular Sommerfield parameter η, orbital angular momentum l and a bound state wave number k.

$$I^A_{ax}(r) \xrightarrow{r>R_{ax}} C^A_{ax} \frac{W_{-\eta_A, l_A+1/2}(2k_{ax}r)}{r} \tag{2.30}$$

Similarly, the asymptotic behavior of the bound state wave function ($\varphi_{ax}(r)$) can also be expressed in terms of the *single-particle ANC (b)* as follows.

$$\varphi_{ax}(r) \xrightarrow{r>R_{ax}} b^A_{ax} \frac{W_{-\eta_A, l_A+1/2}(2k_{ax}r)}{r} \tag{2.31}$$

The overlap wavefunction and the bound state wave function are related to each other via the spectroscopic factor, $I^A_{ax}(r) = S^{1/2}_{ax}\varphi_{ax}(r)$. Then using Equations 2.30 and 2.31, a relationship between the ANC and the single-particle ANC can be found as follows:

$$(C^A_{ax})^2 = S_{ax}(b^A_{ax})^2 \tag{2.32}$$

Using this relationship, Equation 2.20 for the theoretical DWBA cross section can be modified as follows:

$$\left(\frac{d\sigma}{d\Omega}\right)_{\text{exp}} = \frac{(C^A_{ax})^2}{(b_{ax})^2} \frac{(C^B_{bx})^2}{(b_{bx})^2} \left(\frac{d\sigma}{d\Omega}\right)_{\text{DWBA}} \tag{2.33}$$

The partial width ($\Gamma_{ax}(k_{ax})$) calculated at the relative momentum of k_{ax} between particles a and x can be described using the reduced width γ^2 and the penetrability $P_l(E)$ factor evaluated at

the channel radius R_{ax} (Equation 2.34a) as shown by [60].

$$\Gamma_{ax}(k_{ax}) = 2\gamma_{ax}^2 P_{l_A}(k_{ax}R_{ax}) \tag{2.34a}$$

$$\gamma_{ax}^2 = S\gamma_{ax(sp)}^2 \tag{2.34b}$$

The reduced width can be evaluated using the single-particle reduced width γ_{sp}^2 and the spectroscopic factor S as shown in Equation 2.34b [61]. The *penetrability* P_l and the *shift function* S can be expressed in terms of the regular and irregular Coulomb wave functions F_l and G_l as

$$P_{l_A}(k_{ax}R_{ax}) = \Big(\frac{k_{ax}R_{ax}}{F_l^2 + G_l^2}\Big) \tag{2.35a}$$

$$S(k_{ax}R_{ax}) = k_{ax}R_{ax}\Big(\frac{F_l'F_l + G_l'G_l}{F_l^2 + G_l^2}\Big) \tag{2.35b}$$

The formal reduced width γ^2 can be written using the Whittaker function W for the bound state of A as follows.

$$\gamma_{ax}^2 = \frac{W_{-\eta_A, l_A+1/2}^2(2k_{ax}R_{ax})}{2\mu_{ax}R_{ax}}(C_{ax}^A)^2 \tag{2.36}$$

Here, C_{ax}^A shows the ANC of the $A \to a + x$ system, and μ_{ax} is the reduced mass. Then, for sub-threshold resonances (where the state is bound in the entry channel and unbound in the exit channel), the ANC and the formal partial width can be related using Equation 2.34a.

$$\Gamma_{ax}(k_{ax}) = P_{l_A}(k_{ax}R_{ax})\frac{W_{-\eta_A, l_A+1/2}^2(2k_{ax}R_{ax})}{\mu_{ax}R_{ax}}(C_{ax}^A)^2 \tag{2.37}$$

But since the penetrability and the shift function in reality is energy-dependent, the true position of the energy of the resonance will be slightly shifted. Hence, the "formal" partial width from Equation 2.34a will be modified as shown below to give the "observed" partial width:

$$\Gamma_{ax}(k_{ax}) = \frac{2\gamma_{ax}^2 P_{l_A}(k_{ax}R_{ax})}{1 + \gamma_{ax}^2 \frac{dS}{dE}} \tag{2.38}$$

This formalism to obtain the observed partial width is used in the work presented in this dissertation to obtain the partial alpha widths of the resonances in ^{26}Mg which contribute to the ^{22}Ne(α,n) and ^{22}Ne(α,γ) reaction rates.

3. EXPERIMENTAL SETUP AND PROCEDURES

3.1 Experimental Setup

The ^{22}Ne(^{6}Li,d)^{26}Mg and the ^{22}Ne(^{7}Li,t)^{26}Mg reactions were carried out in April 2016 at the Texas A&M University Cyclotron Institute using the Multipole-Dipole-Multipole (MDM) Spectrometer [3]. The MDM focal plane detector was modified for these measurements to accommodate low energies of the detected recoils. Inverse kinematics is used to study these reactions where the dominant reaction yield is at backward angles in the center-of-mass frame at low energies, which translates to forward angles in the laboratory frame. The ^{22}Ne beam of 1 MeV/u energy corresponding to 4.65 MeV in the center-of-mass was obtained from the K150 cyclotron and sent to the beam-line in cave 3 (Figure 3.1). This beam energy was chosen such that the center-of-mass energy would be below the Coulomb barrier of $\sim$ 6 MeV for the ^{22}Ne+^{6}Li system. Both of these reactions were carried out in inverse kinematics because the detection of deuterons and tritons with low energies are more favorable to be detected at small laboratory angles. Direct kinematics for these reactions provided several disadvantages such as the need for a rare isotope gas target and detection of low energy particles in backward angles in the lab frame.

3.1.1 The Target Chamber Setup

For these measurements, ^{6}LiF and ^{7}LiF targets were used with thickness of 30 μg/cm^2 each, which were separately placed in a cylindrical target chamber on a target ladder located at the center. The ^{6}Li enrichment of the ^{6}LiF target was 95.34$\%$ and the lithium in the ^{7}LiF target was natural Lithium (92.41$\%$ of ^{7}Li and 7.59$\%$ of ^{6}Li). The LiF targets were supported by a ^{12}C backing of 10 μg/cm^2 thickness. For additional calibration purposes (described later in the text), a ^{197}Au target of thickness 198 μg/cm^2 was also placed on the target ladder. A Faraday cup was located at the back of the target to measure the incoming beam charge. A Micron quadrant silicon detector (outline shown in Figure 3.2) was placed centered at 25° from the beam axis for additional normalization as well as to monitor the degradation of the LiF targets. Each quadrant of the silicon detector has an

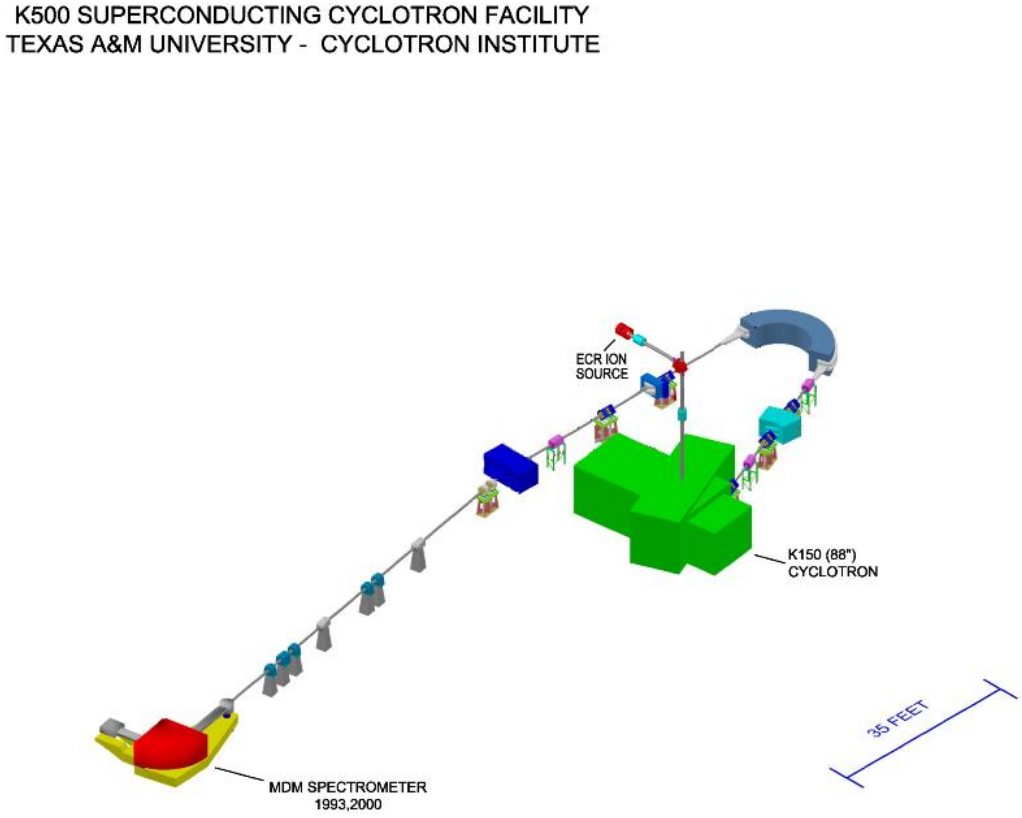

Figure 3.1: Schematic representation of the beam line from the K150 cyclotron to the MDM experimental area.

active area of 2.5 cm x 2.5 cm. In order to get a clear separation of the different reaction products resulting from the various constituents in the target, a collimator was placed in front of the silicon detector with narrow slits for each quadrant (Figure 3.3). The slits for quadrants 1 and 3 were 4.7 x 0.8 mm^2 and for quadrants 2 and 4, were 4.7 x 1.2 mm^2. The separation between the various constituents was better for the quadrants at a larger angle from the beam axis (quadrants 2 and 4).

3.1.2 The Multipole-Dipole-Multipole Spectrometer

The Multipole-Dipole-Multipole (MDM) spectrometer was used to separate out the deuterons and tritons populating the states of ^{26}Mg from the other various reaction products (see Figure 4.1) by setting a specific magnetic field corresponding to the magnetic rigidity of the particles of interest. For the measurements of ^{22}Ne(^{6}Li,d)^{26}Mg and ^{22}Ne(^{7}Li,t)^{26}Mg reactions, the MDM

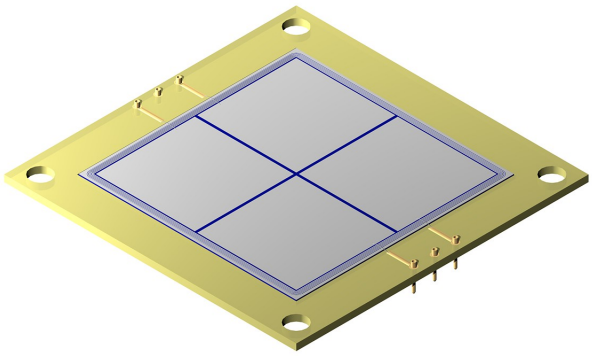

Figure 3.2: Schematic of the quadrant silicon detector.

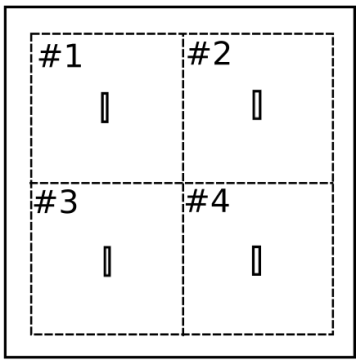

Figure 3.3: Schematic of the Collimator (solid line) in front of the quadrant silicon detector (dashed line).

spectrometer was placed at 5° from the beam axis.

3.1.2.1 Collimator box

The particles of interest are separated out using a 'slit-box', which is located between the target chamber and the spectrometer, and has three different collimation masks located 65.25 cm away from the target location. The three collimation masks are the 'single slit' mask, the '5-finger'

mask, and the 'wide' or '4-by-1' mask (Figure 3.4). The single slit mask has a rectangular opening which is 11.7 mm high and 1.6 mm wide (0.1°). The 5-finger mask has 5 different slits equal to the single slit with each slit separated by 0.765°. The centermost of the 5 slits is centered along the spectrometer center. These two masks are mainly used for calibration purposes. The final mask has a 4° by 1° rectangular opening (11.7 mm high and 45.5 mm wide), hence the name 4-by-1 slit, which is mainly used for data collection purposes. Each mask is made of brass with a lead backing to prevent the particles that do not go through the slits from entering the spectrometer.

(a) Single slit (b) '5-finger' slit (c) '4-by-1' slit

Figure 3.4: Photos showing the different masks used in the collimator box. Each slit is 11.7 mm high.

3.1.2.2 Spectrometer

The MDM spectrometer was built for the University of Oxford and was operational in early 1983. It was moved to Texas A&M University in the late 1990s. The MDM spectrometer has a bending angle of 100° along with a central radius of 160 cm, and a maximum acceptance of 8 msr [3]. A schematic view of the spectrometer is shown in Figure 3.5.

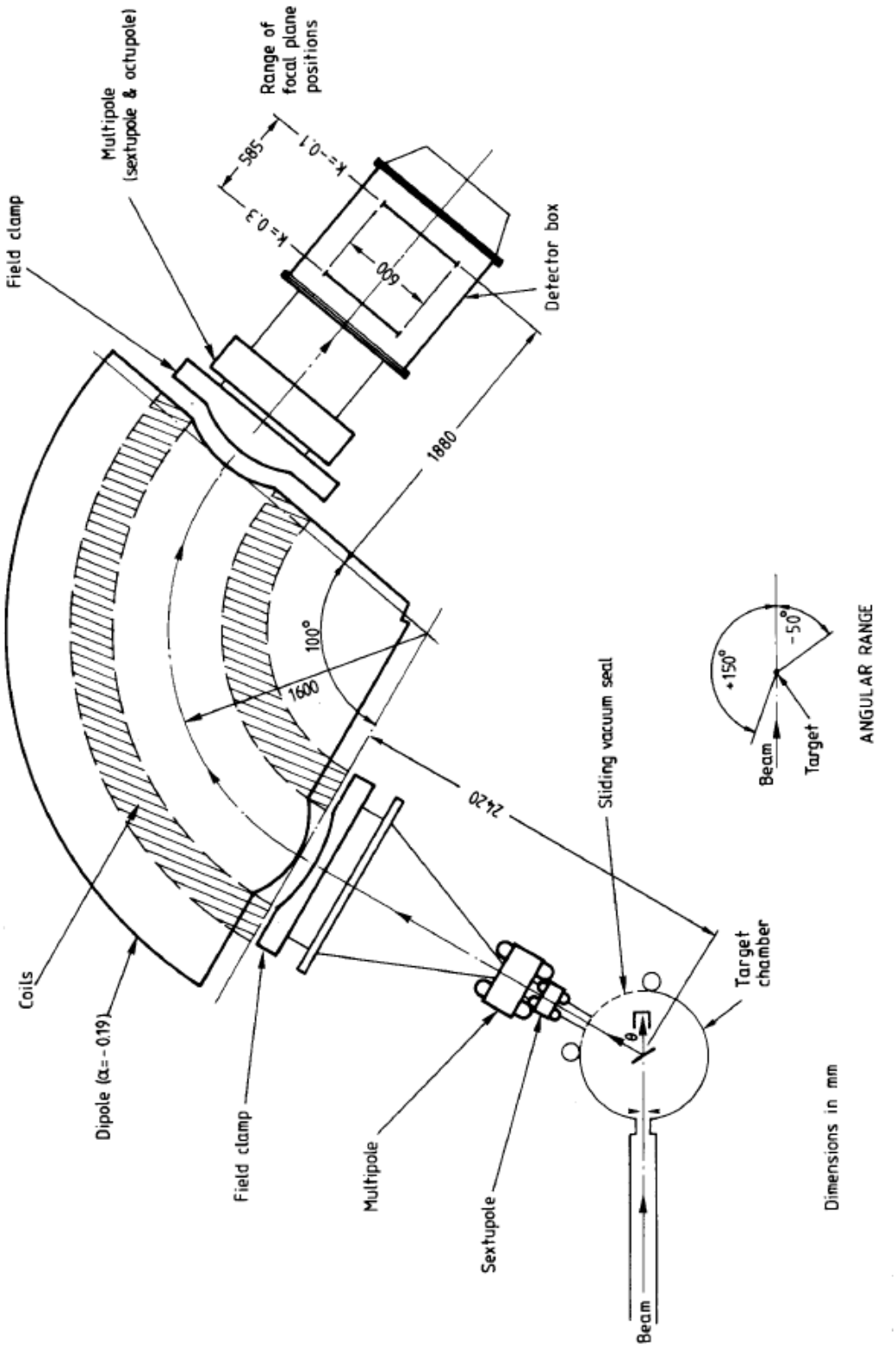

Figure 3.5: Schematic of the various major components along the beam path from the cyclotron: target chamber, multipole, dipole, multipole and focal plane detector. Reprinted from [3]. Units are in millimeters.

The spectrometer has a sextupole and multipole at the entrance, followed by a gradient field dipole, and a multipole at the exit. The maximum field strength of the dipole is 1.5 T. The computer code RAYTRACE [62] is used to determine the settings for the magnetic elements of the spectrometer. This code has the ability to track a specific particle from the target location all the way to the focal plane detector located at the exit of the spectrometer. It also takes into account all the different elements in its path (such as the various magnetic fields) and their distances and thicknesses. The multipole has been calibrated such that the magnitude of the field of the multipole is always a factor of 0.71 of the value of the dipole field.

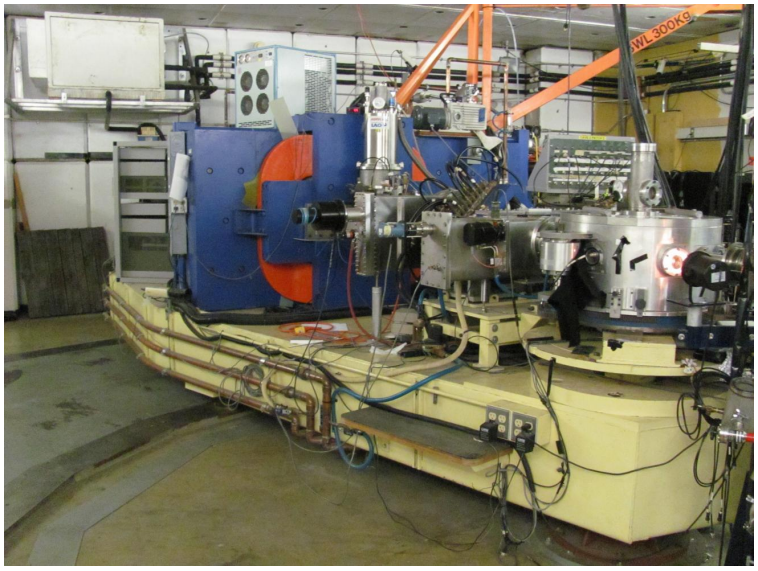

Figure 3.6: The MDM spectrometer and mobile platform (shown in yellow).

The MDM spectrometer has the ability to rotate through $\sim 200^\circ$ around the beam axis (from 50° to the right of the beam direction to 150° to the left looking from the beam direction). This is achieved by a rotating mobile platform on top of which the spectrometer sits (Fig. 3.6).

3.1.3 Oxford Detector

The particles that pass through the MDM spectrometer are detected using the focal plane detector called the Oxford detector. This detector consists of a gas ionization chamber, and located

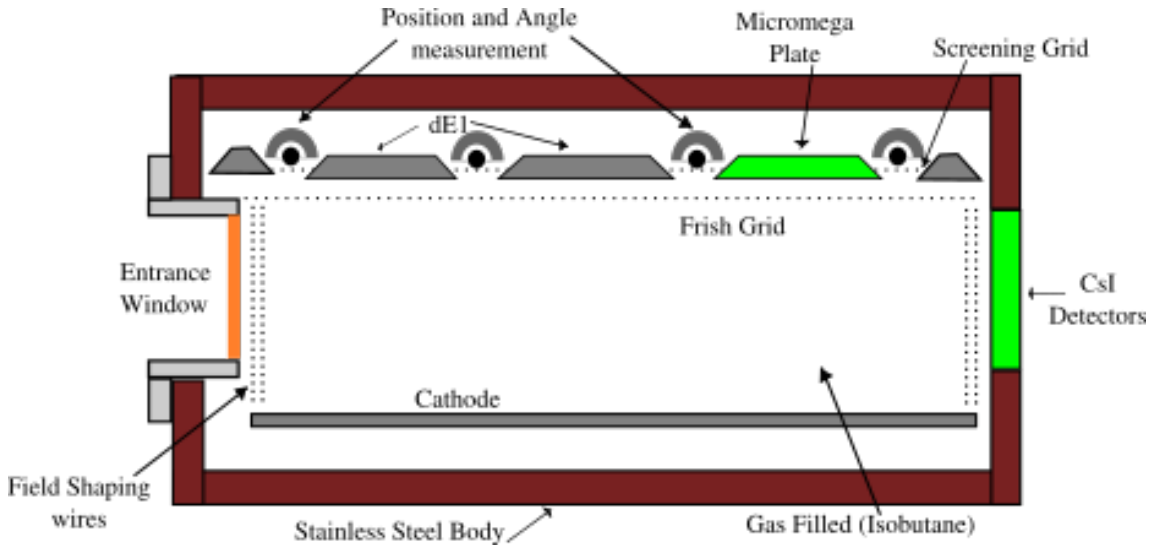

Figure 3.7: Schematic of the cross section view of the modified Oxford detector. It consists of a kapton entrance window, a micromegas plate anode and CsI detector array for particle identification, and 4 proportional counter wires (perpendicular to the beam axis) for particle track reconstruction.

within the chamber are proportional counter wires, anode readouts and Cesium Iodide (CsI) detectors. The chamber has a rectangular shape made of 1.27 cm thick stainless steel and has an active detection region of 30 cm by 51 cm by 10.5 cm (w x l x h). The gas used for this measurement was pure isobutane gas at a pressure of 50 Torr. Isobutane has an ionization potential of 10.52 eV [63]. The pressure was monitored using a Baratron gauge. A schematic of the cross sectional view of the Oxford detector is shown in Figure 3.7. The cathode and the two inter-connected anode plates between the 1^{st} and 2^{nd} wires and the 2^{nd} and 3^{rd} wires are made of aluminum. The gap between the anode plane and the cathode plane is 12 cm.

The Oxford detector was originally built for the detection of charged heavy particles. When these particles travel through the gas volume after entering through the entrance window, they ionize the gas molecules in their path creating electron-ion pairs. The electrons are attracted to the anode and the positive ions drift towards the cathode.

Additionally, there is another set of wires around the detection area which acts as a field cage to form a uniform electric field between the cathode and the anode. There are 14 wire levels in

total and each are inter-connected by an electronic voltage divider setup. In this electric field, the electrons travel quickly towards the anodes and produces a rapid signal. The drift of the positive ions towards the cathode is slower compared to the electrons, which results in the positive ions inducing a signal on the anode over a longer period of time. This results in a detection pulse in the anode which does not show a linear response to the energy loss of the charged particles. This effect from the positive ions can be eliminated by using a Frisch Grid.

The Frisch Grid is situated 10.5 cm above the cathode. It is made up of multiple, uniformly-spaced Be-Cu wires. Each wire is 40 cm long and is 80 μm in diameter. The pitch between each wire is 1.5 mm. The role of the Frisch Grid is to screen the anode plane from the positive ions created during the ionization of gas particles. Using correct biases for the anode, Frisch Grid and cathode, transparency of the Frisch Grid to the electrons can be ensured.

3.1.3.1 Proportional Counter wires

The Oxford detector contains four resistive avalanche counter wires to measure the track of the particles through the detection volume. Each wire is made of a Ni-Cr-Fe alloy (Stablohm 675 from California Fine Wire company), and has a diameter of 12.5 μm and a length of 40 cm. The first wire is located 2 cm behind the entrance window. From the first wire, the other three wires are placed at distances of 15.1 cm, 31.4 cm and 47.7 cm, respectively. One end of each wire is biased between +800 V and +1500 V depending on the desired signal strength.

Each wire is surrounded by an aluminum body called a 'shell', which is usually biased at +100 V. The electric field between the shell and the wire gradually increases in strength going from the shell to the wire. Electrons that pass through the Frisch Grid are accelerated in this field and interacts with neutral atoms in the gas creating many secondary electron-ion pairs, which in turn creates additional pairs. This process is known as Townsend Avalanche. There are individual screening grids underneath each wire to protect the Frisch Grid from all the positive ions created during the avalanche process.

The output signal from the wires have two components: a direct signal from the attracted electrons and an induced signal from the motion of the positive ions. The main contributor to the

output signal comes from the positive ions; the electron component is considered negligible. The signal is then divided across the wire resistance and sent to each end of the wire. Each signal's amplitude is inversely proportional to the encountered resistance which in turn depends on the length from the interaction point to the end of the wire. Using this fact, the interaction location (x) along the wire for a wire length of (D) can be determined by using the readout charge from the left (Q_L) and right (Q_R) side of the wire.

$$x = \frac{Q_L}{Q_L + Q_R} D \,, \tag{3.1}$$

Using the interaction points of the 4 wires, the track taken by the particle of interest through the Oxford detector can be reconstructed after properly calibrating the wire positions.

3.1.3.2 The microMegas detector

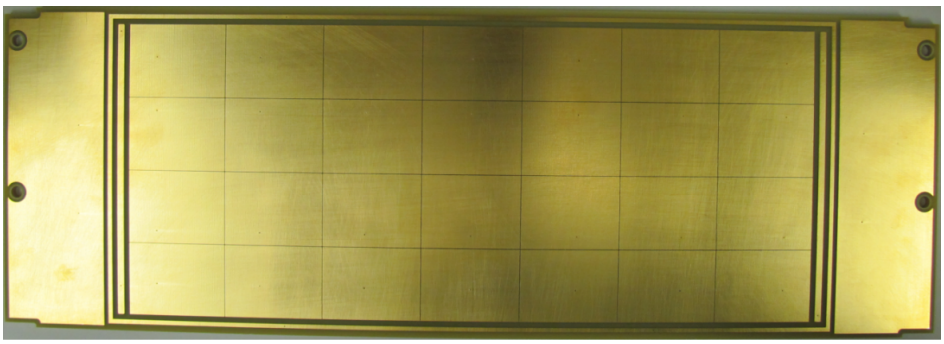

Figure 3.8: The segmented microMegas detector used in the Oxford detector.

A recent upgrade [64] to the Oxford detector was done to improve the energy loss detection of particles in the gas volume. This was done by installing a microMegas detector (Figure 3.8) between the 3rd and 4th wire, replacing an aluminum plate. The microMegas detector has a small amplification gap 128 μm and a much larger drift gap. These two different regions are separated using a thin metallic "micromesh".

Figure 3.9 shows the individual components of the microMegas detector. The main printed

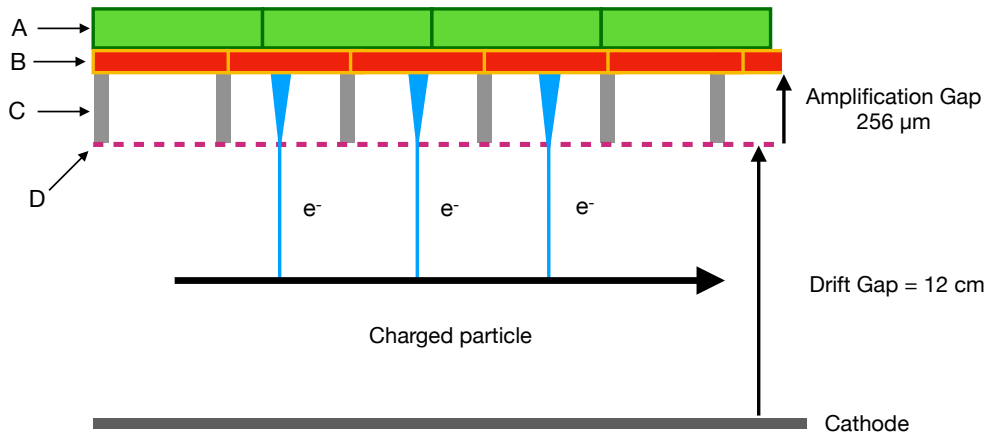

Figure 3.9: Individual components of the microMegas detector: A) The printed circuit board B) gold-plated copper pads C) resin pillars D) micromesh.

circuit board (PCB) of 6 mm thickness has 28 gold-plated copper pads, each with dimensions 32.5 mm by 44 mm. There are 4 rows of pads and 7 columns, each separated by a spacing of $\sim$0.2 mm. The PCB is made of multiple layers of circuit boards with 6 grounded copper layers in between, which allows the signals between the pads and the connectors to have no capacitive connections to other pad-lines. The PCB has been designed to minimize noise and cross-talk between pads.

The micromesh sitting below the pads is made of stainless steel interwoven wires. The micromesh is located 128 μm below the pads and this region is called the amplification gap. The mesh is supported by many tiny insulating resin pillars. These pillars ensure the uniformity of the amplification gap to an accuracy of a few microns. This very small amplification gap produces high electric field that generates the avalanche, and hence, results in the microMegas having an overall amplification of up to 10^5 [65]. This high amplification was desirable for the ^{22}Ne(^{6}Li,d)^{26}Mg and ^{22}Ne(^{7}Li,t)^{26}Mg reactions where the particles detected in the Oxford detector are Z=1 ions that have small specific energy losses in the gas.

The positive ions created during the avalanche process are collected by the mesh while the pads collect the charge from the electrons. The positive ions that escape the mesh are then collected by the Frisch Grid. The output signal from each pad is the sum of the ion-induced signal and the

signal from the electrons.

3.1.3.3 Modification

The original Oxford detector consisted of an entrance and exit windows for the gas section made of aramica foil. The thicknesses of these two windows are 25 μm and 50 μm, respectively. Each window is 6 cm high and 30 cm wide. Due to these windows, the gas volume can handle pressures up to 150 Torr. The original Oxford detector also has a plastic scintillator made of BC-400, which is attached to the exit window frame and lies behind the exit window. The light produced by the scintillator is collected by two Hamamatsu photomultiplier tubes connected to either end of the scintillator.

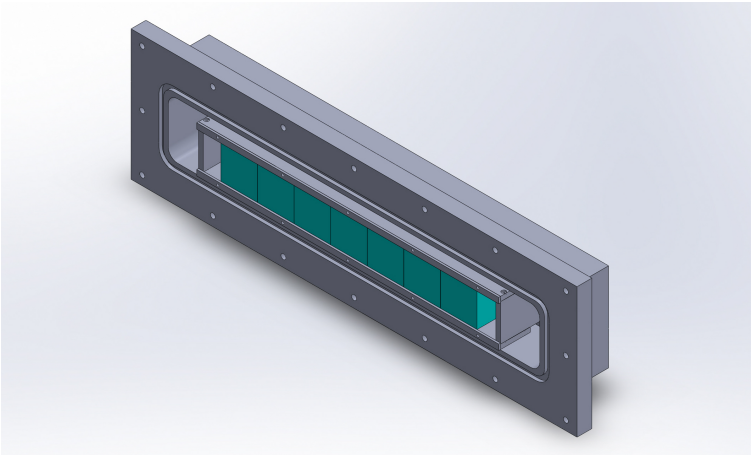

Figure 3.10: Schematic of the new exit flange of the Oxford detector holding 7 Cesium Iodide detectors.

For the study of the ^{22}Ne(^{6}Li,d)^{26}Mg and ^{22}Ne(^{7}Li,t)^{26}Mg reactions, the deuterons and tritons will lose a few MeV in the Oxford detector and will lose more energy while travelling through the 50 μm thick exit window. Once the particles have passed through the window the residual energy falls in the noise regime for the plastic scintillator that originally came with the Oxford detector. In order to overcome this obstacle, it was necessary to remove the exit window, the scintillator, and the photomultiplier tubes. This entire back unit was replaced by a new back flange that held seven

CsI(Tl) scintillator detectors (Figure 3.10). This flange contains an O-ring to ensure that the gas pressure of the Oxford can be controlled without an exit window. Each detector has an active area of 50 mm x 50 mm, and a thickness of 40 mm. Each CsI detector is individually wrapped by 2 μm Mylar foil, and has a resolution of 2.8%.

3.1.4 The DAQ System / Electronics

Component	Bias (Volts)
Silicon detector	-150
CsI detectors	+60
Cathode	-800
Proportional counter wires	+1000
microMegas pads	+360
Shell	+100

Table 3.1: The biases used for the various components of the Oxford detector and target chamber.

The voltage biases used for the various detector components are listed in Table 3.1.

For each proportional counter wire, the position along the wire (POS) can be calculated using the left (L) and right (R) signals after the Analog-to-Digital Converter (ADC) using the following formula:

$$\text{POS} = A\frac{L}{L+R}\,. \tag{3.2}$$

Here A (=1024) is the number of channels in the histogram for the position along the proportional counter wire, and L/R are the charges induced at the left/right end of the wire. Each end of the 4 wires was connected to a Canberra 2004 preamplifier, and all the preamplifiers were connected to a CAEN N568B 16-channel spectroscopy amplifier. The wires were biased using the

preamplifiers on the right side of each wire. The bias applied for the wires depends on the required gas gain and can vary from experiment to experiment.

For the microMegas pads, row 1 and 2 were connected to a Mesytec MPR-16 preamplifier. A second similar preamplifier was used for row 3 and 4 (4 rows total). Both of these preamplifiers were then connected to a Mesytec MSCF-16 shaper amplifier.

All the signal amplitudes were digitized using Mesytec MADC-32 (analog to digital converter) 32-channel modules, and the timing signals were obtained using a 128-channel Caen V1190 TDC (time to digital converter) module. The schematic for the analog electronic signals is shown in Figure 3.11. The coincidence between the two shaper module triggers from the two sections of the microMegas detector was taken as the first level of trigger. Next, this was combined with the signal from the CsI detector array. For the final trigger, the CsI and microMegas coincidence was combined with the silicon detector trigger using a Philips Quad 4-Fold Logic Unit along with the DAQ veto (dead-time) signal, in order to record only the events of interest (Figure 3.12). One logic output of this module was then used as the trigger for the acquisition. Another output was sent to an Ortec 8010 Gate and Delay Generator module to create the logic gates for the ADC modules. The Gate and Delay Generator created a 6.4 μs gate for the ADC modules. A third output was used to trigger the TDC module (see Figure 3.13). The silicon detector timing signals were prescaled by a factor of 100 to reduced the amount of data recorded for the silicon detector. The silicon and CsI detector array analog signals were also send to a Mesytec MPR-16 preamplifier, Mesytec MSCF-16 shaper amplifier and Mesytec MADC-32 modules respectively.

Data events were collected using a VME electronics crate and observed, recorded and analyzed with a software created in Linux, using the C++ based ROOT framework [66].

3.2 Experimental Procedures

Before using the ^{22}Ne beam for the study of interest, we first employed a 8 MeV deuteron beam from the K150 Cyclotron for calibrations and to normalize the Faraday cup. The energy of this deuteron beam was chosen such that it was very similar to the energies of the deuterons produced by the ^{22}Ne(^{6}Li,d) reaction. For this study, the single-slit mask was used in the collimator box

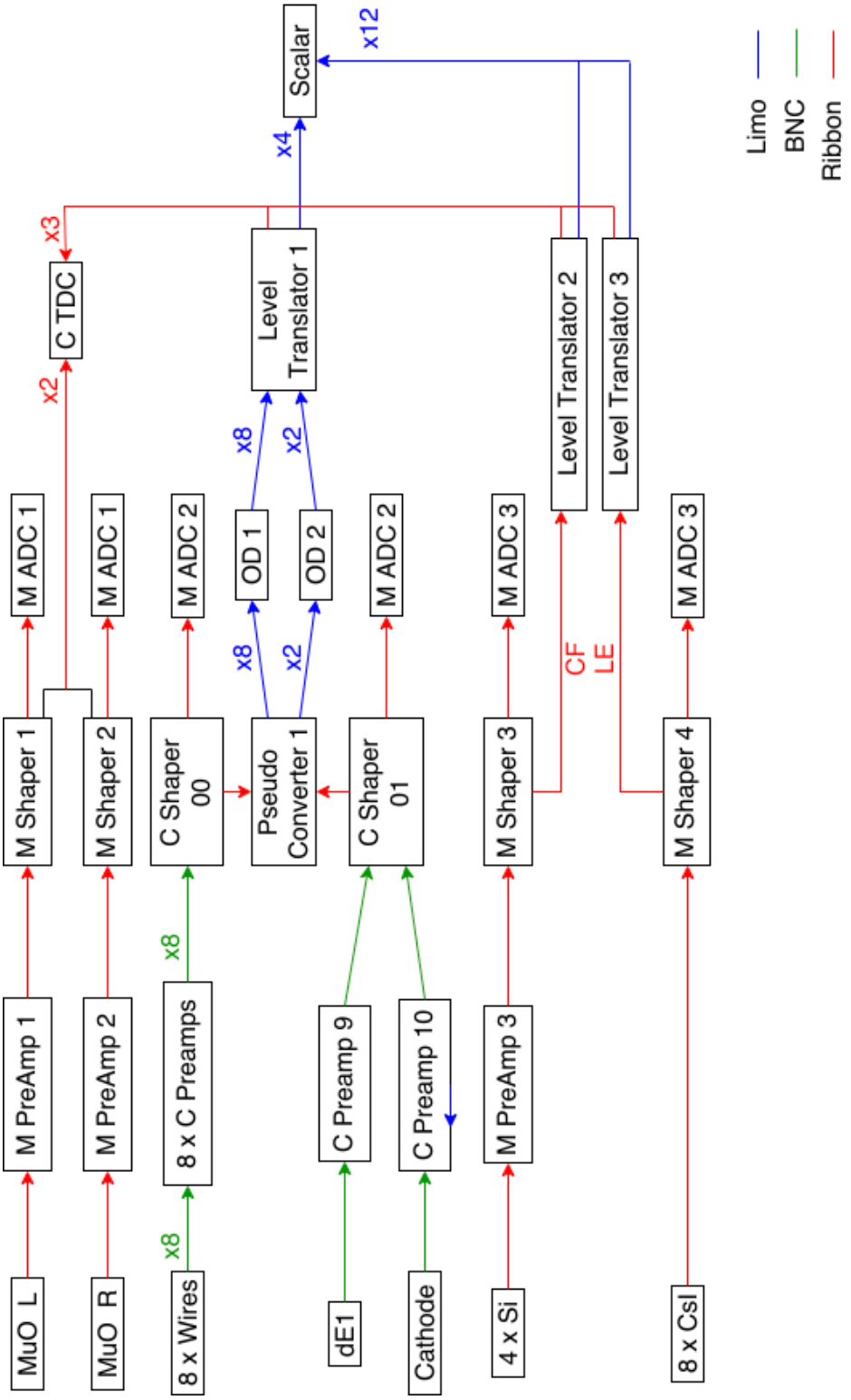

Figure 3.11: Electronic schematic (C ≡ Caen, M ≡ Mesytec)

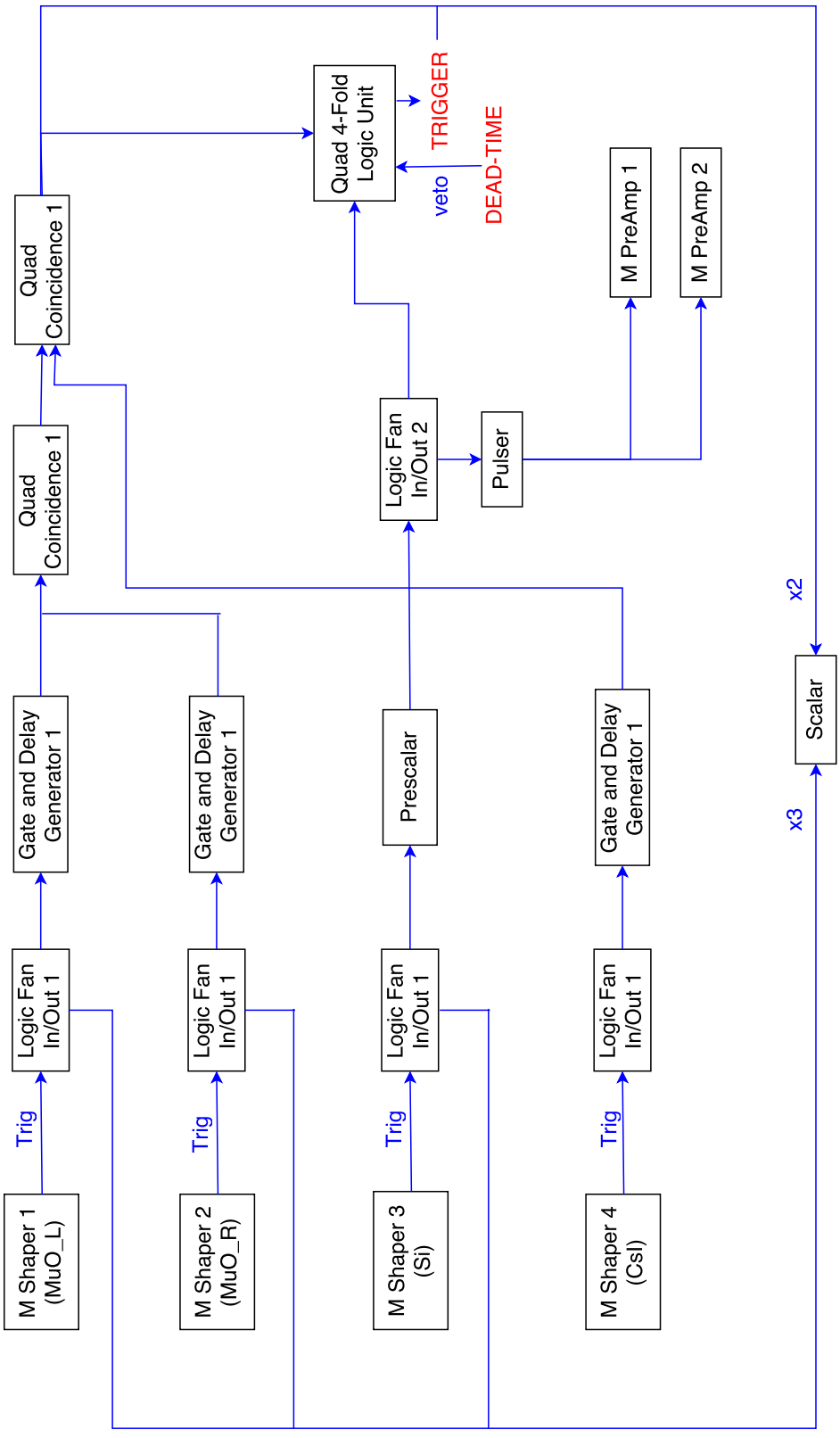

Figure 3.12: Timing signal schematic (C ≡ Caen, M ≡ Mesytec, MuO ≡ microMegas)

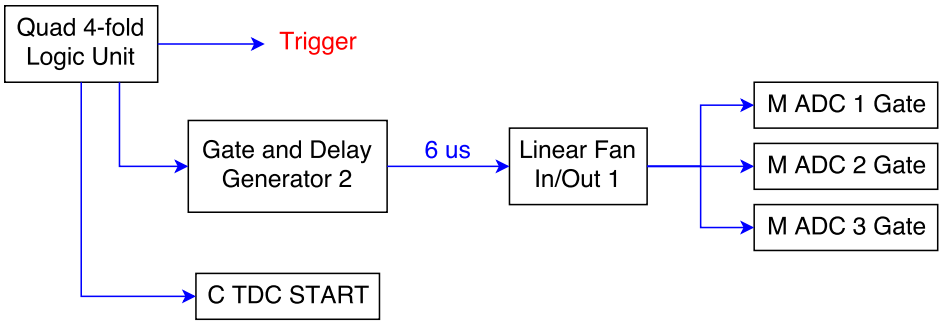

Figure 3.13: The trigger setup schematic (C ≡ Caen, M ≡ Mesytec)

to obtain a narrow recoil beam. Several calibration measurements (explained later in the section) were then done using elastic scattering of the deuteron beam on ^{197}Au target foil of thickness 198 μg/cm^2. The intensity of the deuteron beam was 150 pnA at the target location. The narrow deuteron beam is sent across the MDM spectrometer and into the Oxford detector.

3.2.1 Detector Center and Deuteron Beam Energy

The energy of the deuteron beam was found by observing the elastically scattered deuterons in the silicon detector placed in the target chamber. Each quadrant of the silicon detector was calibrated using a 4-peak alpha source consisting of four different radioactive isotopes: ^{148}Gd, ^{239}Pu, ^{241}Am and ^{244}Cm. The energies of the peaks of the alpha source were 3.117, 5.142, 5.474 and 5.787 MeV. Taking into account the energy loss of the deuterons in the 0.5 μm dead layer of the silicon detector, the deuteron beam energy was found to be 7.8 MeV. An additional check for the deuteron beam energy was also carried out by sending the elastically scattered deuteron beam into the Oxford detector, and by recreating the deuteron energies at the target location using the code MDMTRACE. Both of these methods result in a very similar deuteron beam energy of 7.8 MeV.

MDMTRACE is a code which runs the computer code RAYTRACE [62] in a 'reverse' direction. By using the RAYTRACE code for the MDM spectrometer and Oxford detector, the path of a particle can be tracked from the target location until the end of the focal plane Oxford detector. This code takes into account the effects of all the magnetic elements along the path of the particle

such as the multipoles and dipole defining the MDM spectrometer. The main function of RAYTRACE is to track a particle (with a specific magnetic rigidity) right after the reaction location (generally a solid target) with a given initial energy and angle from the beam axis. The output of RAYTRACE gives the location of the particle in each of the 4 proportional counter wires of the Oxford detector. The angle of the particle relative to the center axis of the Oxford detector can be found using the positions along any two proportional counter wires. The MDMTRACE code was developed at Texas A&M University Cyclotron Institute to use the properties of RAYTRACE and do a reverse calculation. MDMTRACE uses the position of a particle along the 4 wires of the Oxford detector obtained experimentally for specific magnetic fields of the magnetic elements of the MDM spectrometer, and finds the corresponding energy and angle at the target location using a chi-square minimization routine.

Since the microMegas detector is centered on the center axis of the Oxford detector, and since the pads of the microMegas detector have a well-defined width, the center of the detector can be found using the central column of the microMegas. The elastically scattered deuteron beam through the Oxford detector can be swept from one corner to the other corner by changing the field of the dipole magnet. The dipole field values were found for the two edges of the central column of the microMegas detector by observing the charge collected by each pad on either side of an edge. When the charge is equal on either side of an edge, it means that the magnetic field is set right along the edge. In this manner, once the field values for both edges of the central column were found, the mean of these two values will provide the dipole field for the detector center for the deuteron beam.

3.2.2 Energy Calibration of the Oxford detector.

The elastically scattered deuterons have an energy of 8 MeV within the Oxford detector. Since energies are very close to the deuteron energies from the ^{22}Ne(^{6}Li,d)^{26}Mg reaction, this beam was used to calibrate the microMegas pad energies and the CsI detector energies. The raw deuteron spectrum obtained from the CsI detector located along the center of the Oxford detector is shown in Figure 3.14. The channel spectrum from the ADC for the CsI detectors and microMegas pads

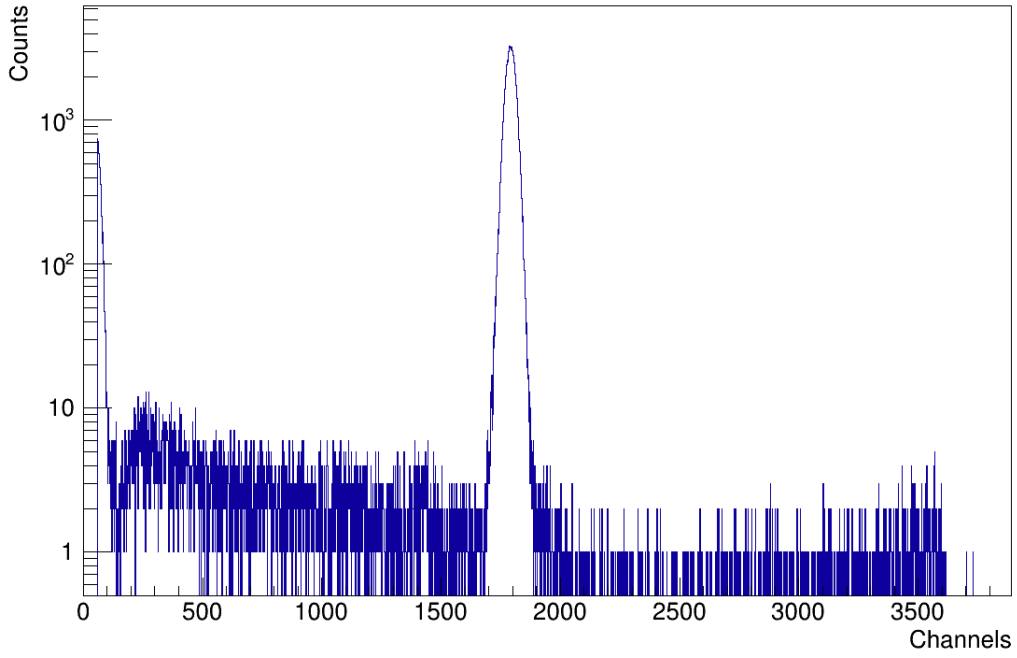

Figure 3.14: The raw spectrum of elastically scattered deuterons from the CsI detector located along the center of the Oxford detector.

were calibrated for 3.5 keV/channel and 5.5 keV/channel respectively.

3.2.3 Gain-matching the wires

Before any new measurement with the Oxford detector is performed, the 4 avalanche counter wires have to be gain-matched. The elastically scattered deuteron beam used to find the center of the Oxford detector was also used for the gain matching. For this, all the right-side (R) signals of the 4 wires were set to the same gains in their respective shapers. Since there are 1024 channels in the histograms for the position along each wire, the gains of the left-side (L) shapers were changed until the peak due to the beam appeared at channel 512 for each wire.

Once all the wires were gain-matched, the position resolution for each wire were calculated by fitting a gaussian to the deuteron beam peak for the detector center run. The wire resolutions were as follows:

Wire number	Resolution (mm)
1	3.6
2	4.0
3	5.2
4	6.4

Table 3.2: The position resolution for 7.8 MeV deuterons for the 4 wires of the Oxford detector.

3.2.4 Position Calibration

The position calibration for the signals from the 4 wires was done using the collimated deuteron beam and the edges of the pads of the microMegas. Following the same procedure detailed in Section 3.2.1, seven (7) *"beam sweep"* measurements were taken for every pad edge and the detector center (one detector center measurement and 3 inter-pad locations on either side).

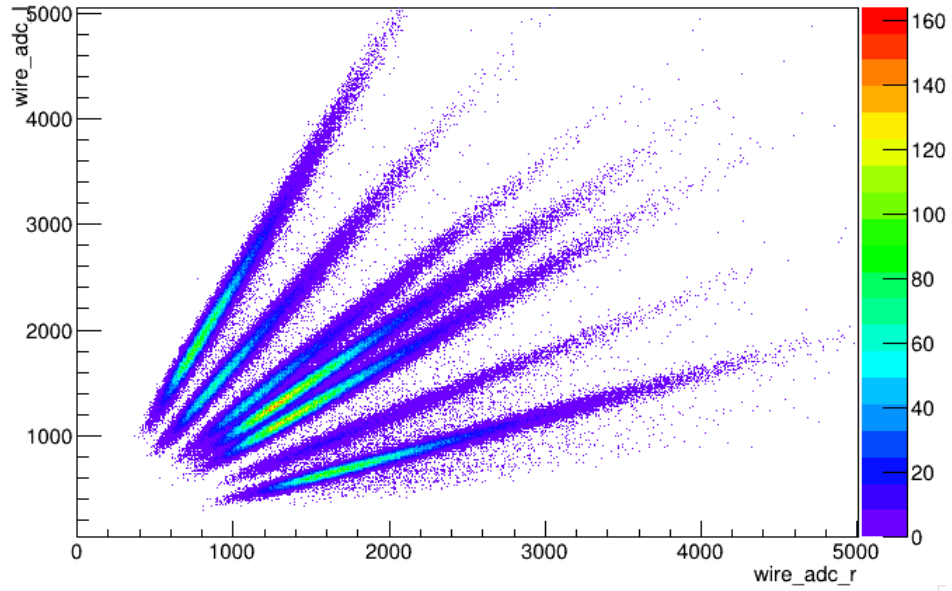

Figure 3.15: Two-dimensional plot for wire 1 with the left and right signals from the ADCs for the beam sweep plotted against each other. Units are in ADC channel numbers.

Once these 7 measurements were done, then the MINUIT2 minimization function of ROOT was used to calibrate the positions of each wire. The procedure for the calibrations is described below.

First, each signal obtained for each wire from the left side (L) is assumed to have a linear response. This linear response is defined using two undetermined variables A and B, and the same for the right side (R) with variables C and D. Then these two signals will be "$A + BL$" and "$C + DR$". Then Equation 3.2 becomes:

$$\text{POS} = \frac{(A + BL)}{(A + BL) + (C + DL)} \tag{3.3}$$

Equation 3.3 only gives a ratio. In order to compare this with the known positions for the pad edges, this has to be converted to measurable units. This is done using two additional variables E and F, to be determined. Then the ratio in Equation 3.3 becomes,

$$P(L, R) = E * \Big(\frac{A + BL}{A + BL + C + DL}\Big) + F \tag{3.4}$$

Here, $P(L, R)$ is the position for one wire calculated as a function of the left and right signals from the ADCs. Next, the positions for each wire for the 7 different magnetic fields corresponding to the 7 beam sweep measurements were calculated using the RAYTRACE code. Then a χ^2 minimization was done between the RAYTRACE position values and the experimental position obtained using Equation 3.4 for each of the 4 wires, and the parameters A through F were found for each wire. Finally, these parameters were used to obtain the position of each particle along the wire in units of centimeters. The calibrated positions of the beam sweep measurements ("Experimental Pos") plotted against the theoretical values obtained by RAYTRACE ("Theoretical Pos") are shown in Figure 3.16. The y-axis in the plot in Figure 3.16 is restricted to show the actual total length of 30 cm of each proportional counter wire.

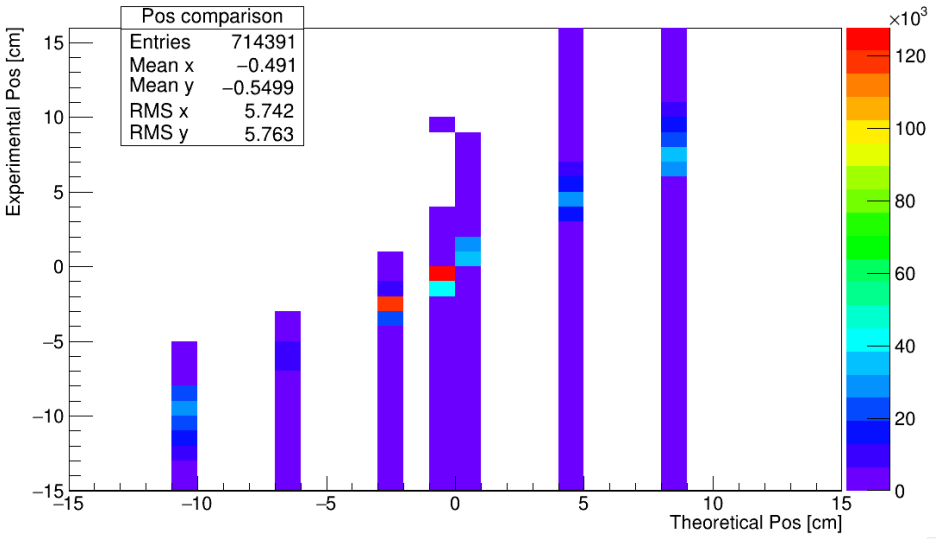

Figure 3.16: Two-dimensional plot for wire 1 with the calibrated experimental positions against the theoretical positions.

3.2.5 Faraday Cup Normalization

In order to properly count the incoming beam particles, it is necessary to normalize the Faraday cup (FC) placed downstream of the target location. This normalization should be done with the Faraday cup placed at the location it will remain during the experiment, and it should be done at the beginning of every experiment.

$$\sigma_{Ruth} = \left(\frac{Z_{\text{target}} Z_{\text{beam}}\, e^2}{4E} \right)^2 \frac{1}{\sin^4(\theta/2)} \,. \tag{3.5}$$

Equation 3.5 gives the formula to calculate the Rutherford cross section. Here, E is the energy of the beam, e is the electron charge, Z is the atomic charge and θ is the c.m. scattering angle. Accounting for the finite mass of the target (M) and the projectile (m), Equation 3.5 can be generalized as follows.

$$\sigma_{Ruth} = \left(\frac{Z_{\text{target}} Z_{\text{beam}}\, e^2}{2E} \right)^2 \frac{1}{\sin^4\theta} \frac{\{\cos\theta \pm [1-(m/M)^2 \sin^2\theta]^{1/2}\}^2}{[1-(m/M)^2 \sin^2\theta]^{1/2}} \,. \tag{3.6}$$

The normalization is done at small laboratory angles using a very heavy target, ensuring that

the elastic scattering is mainly the Rutherford cross section (σ_{Ruth}). In this particular case, the same deuteron beam and the Au foil used for position calibration measurements were also used for the Faraday cup normalization.

Data was taken for a specific number of counts in the beam current integrator and the experimental cross section (σ_{exp}) can be calculated. Then it is compared with the theoretical cross section given by Equation 3.5. The ratio of the theoretical and experimental cross sections obtained in this manner (f) is used to correct for the counts from the current integrator (FC_{corr}) for further calculations:

$$f = \frac{\sigma_{exp}}{\sigma_{Ruth}} \qquad\qquad FC_{corr} = f \times FC$$

4. DATA ANALYSIS AND RESULTS

The 1 MeV/u ^{22}Ne beam from the K150 Cyclotron was used to measure the ^{22}Ne(^{6}Li,d)^{26}Mg and ^{22}Ne(^{7}Li,t)^{26}Mg reaction cross section using the ^{6}LiF and ^{7}LiF targets. A detailed description of the experimental procedures, theoretical analysis and results for these two measurements are presented in this chapter.

4.1 Cross section normalization procedures

It is critical to obtain accurate and verifiable normalization in this experiment to have reliable absolute values for the cross section. Elastic scattering of ^{22}Ne on ^{6}Li was used for this purpose, as described below.

The K150 Cyclotron provided a ^{22}Ne beam with charge state 3^{+}. When the beam is travelling through the target, the electrons of the ^{22}Ne beam interact with the atoms in the target, and the equilibrium charge state of ^{22}Ne ions after the target is different than the initial one. We have evaluated the effective charge state after the target using the following procedure.

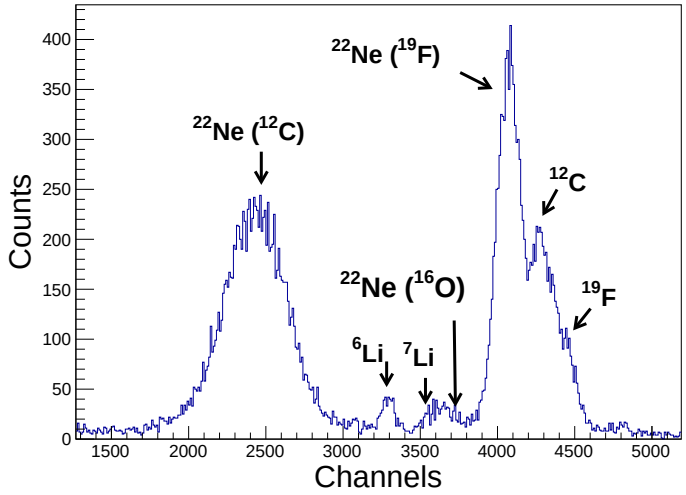

Figure 4.1: The spectrum from quadrant 2 of the silicon detector. The various peaks arise from the ^{22}Ne beam elastically scattering off of the various components of the target (^{12}C, ^{19}F and ^{16}O), as well as elastically scattered ^{6}Li, ^{7}Li, ^{12}C and ^{19}F from the ^{22}Ne beam.

The beam current was measured by the Faraday cup, located at zero degrees after the target using a blank target frame. The beam current was monitored between the measurements with the ^{6}LiF target and a blank target by the Faraday cup upstream of the target. It was found that the Faraday cup reading was about a factor of two higher with the target than without. Hence, the equilibrium charge state of the ^{22}Ne beam has changed from 3^{+} to about 6^{+} after the target. This gives as approximate initial normalization, but the more accurate normalization procedure is described below.

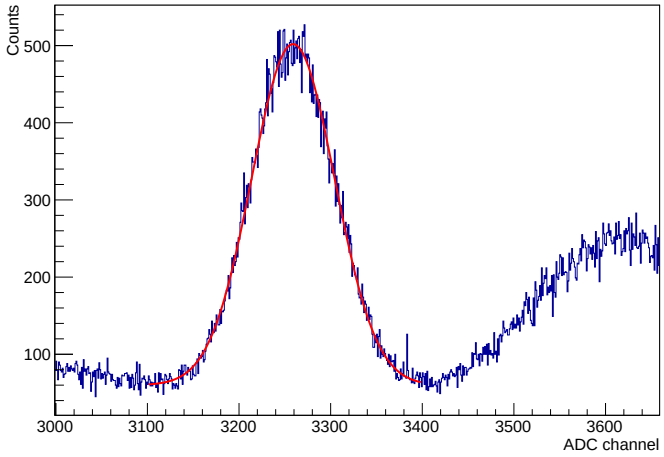

Figure 4.2: The elastically scattered ^{6}Li peak in the silicon detector (zoomed from Figure 4.1) fit with a flat background below the peak from channel 3100 to 3400, and a Gaussian fit to obtain the true number of counts in the peak.

The ^{6}Li ions in the target which are elastically scattered from the ^{22}Ne beam were measured in the silicon detector installed inside the scattering target chamber as well as by the Oxford detector at two different angle settings of the MDM spectrometer (5° and 10° from the beam axis). The spectrum from the 2^{nd} quadrant (upper right) of the silicon detector from the ^{22}Ne beam on the ^{6}LiF target is shown in Fig. 4.1. The peaks in Fig. 4.1, going from left to right, are: the ^{22}Ne elastically scattered on carbon backing of the LiF target, the elastically back-scattered ^{6}Li ions, a small contribution from elastically back-scattered ^{7}Li ions overlapping with ^{22}Ne ions elastically

scattered on ^{16}O that is present on the surface of the target, the ^{22}Ne ions elastically scattered on the fluorine target nuclei, and the ^{12}C and ^{19}F ions back-scattered by the ^{22}Ne beam. As seen in Figure 4.1, the background introduced by other various elements have to be subtracted to obtain the number of back-scattered ^{6}Li.

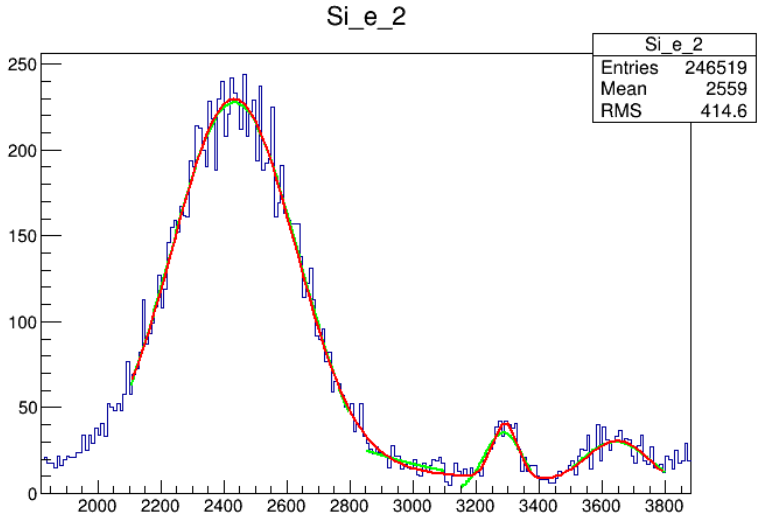

Figure 4.3: Curve fit to obtain pure elastically scattered ^{6}Li in the silicon detector for 5° MDM angle.

For the elastically scattered ^{6}Li peak in the silicon detector, two extreme background subtraction cases were considered to obtain the proper number of elastically scattered particles. One was assuming a flat background under the ^{6}Li peak. The Gaussian fit, which includes the flat background for the ^{6}Li peak is shown in Figure 4.2. Another assumption is that there is no "flat" background, only a contribution from neighboring peaks that are accounted for by a multi-Gaussian fit as shown in Fig. 4.3. The systematic error associated with the assumptions made on the shape of the background was found to be 4.5.

The Oxford detector and the MDM spectrometer were used to measure the elastically back-scattered ^{6}Li ions at large c.m. angles (160° and 170°). The raw spectrum obtained from the 2nd proportional counter wire of the Oxford detector is shown in Figure 4.4 for the spectrometer

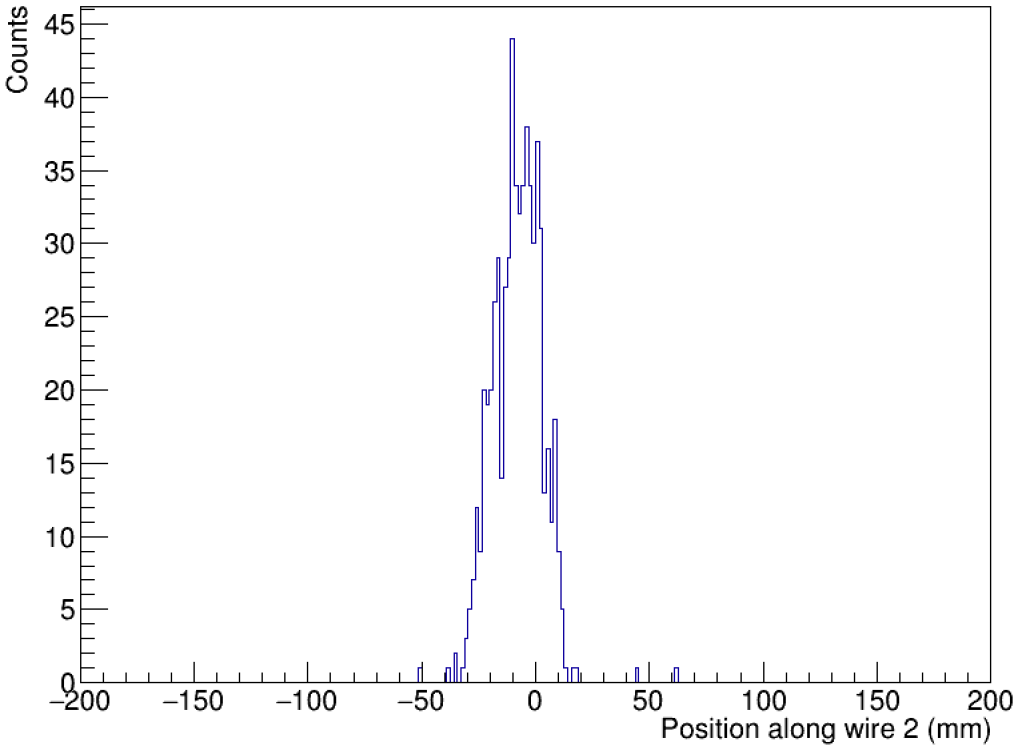

Figure 4.4: The raw spectrum from the 2nd proportional counter wire of the Oxford detector when the dipole field was set to accept ^{6}Li elastically scattered from the ^{22}Ne beam. The physical length of the wire spans from -150 mm to +150 mm. Unlike from the silicon detector, the absence of any background when using the MDM spectrometer is evident from this spectrum.

at 170° in center of mass. This x-axis of this figure is the position along the wire where the center of the detector is at 0 mm after the position calibration (the total length of the actual wire is 300 mm, i.e 150 mm to each side from the center of the detector). As seen in this figure, a background subtraction is not necessary. Only a peak associated with the elastically scattered ^{6}Li ions is observed. Using the number of ^{6}Li ions measured in the Oxford detector, the nominal elastic scattering cross sections can be calculated.

The experimental cross section ($d\sigma/d\Omega$) in the center of mass frame can be calculated as follows:

$$\frac{d\sigma}{d\Omega} = \frac{Nk}{It\Delta\Omega} \tag{4.1}$$

$$I = \frac{\text{Amount of charge collected}}{\text{(Electron charge) x (Charge state)}} \tag{4.2a}$$

$$t = \frac{\text{(Target thickness in g/cm}^2\text{) x (Avagadro constant)}}{\text{Atomic mass of the LiF}} \tag{4.2b}$$

where N is the number of counts in the peak of interest, k is the conversion factor between lab and center-of-mass frames, I is the total number of beam ions impinged on the target, t is the effective target thickness (Equation 4.2b) and $\Delta\Omega$ is the solid angle. The Faraday cup used for this measurement gives a signal measured using a current integrator, producing the total accumulated charge.

The silicon detector placed in the target chamber has a collimator in front of it with slits described in Section 3.1.1. Using the distance to the collimator and the dimensions of the slits, the solid angle for the 2$^{\text{nd}}$ quadrant can be accurately calculated. This, the values obtained from the faraday cup, the charge state of the beam, the nominal target thickness and the background-subtracted number of ^{6}Li peak counts from the silicon detector can be used in Equation 4.1 to calculate the elastic cross section for the angle of the silicon detector (see Figure 4.5). Here, three nominal cross sections for the 2nd quadrant of the silicon detector have been calculated for the number of counts recorded in three separate measurements: 1) Detecting deuterons from the (^{6}Li,d) transfer reaction (magenta circle in Figure 4.5) 2) Detecting elastically scattered ^{6}Li for the MDM spectrometer placed at 5 degrees (red circle in Figure 4.5), and 3) Detecting elastically scattered ^{6}Li for the MDM spectrometer placed at 10 degrees (blue circle in Figure 4.5). For the last two measurements, the MDM spectrometer used the '4-by-1' mask (described in the previous Chapter) which has a nominal solid angle of 1.25 millisteradians (msr). Using this, along with the number of ^{6}Li particles detected in the Oxford detector, the nominal elastic cross sections can be found for the two different angles of the MDM spectrometer (5° (red triangle in Figure 4.5) and 10° (blue triangle in Figure 4.5)) as well. The two laboratory angles of the spectrometer correspond

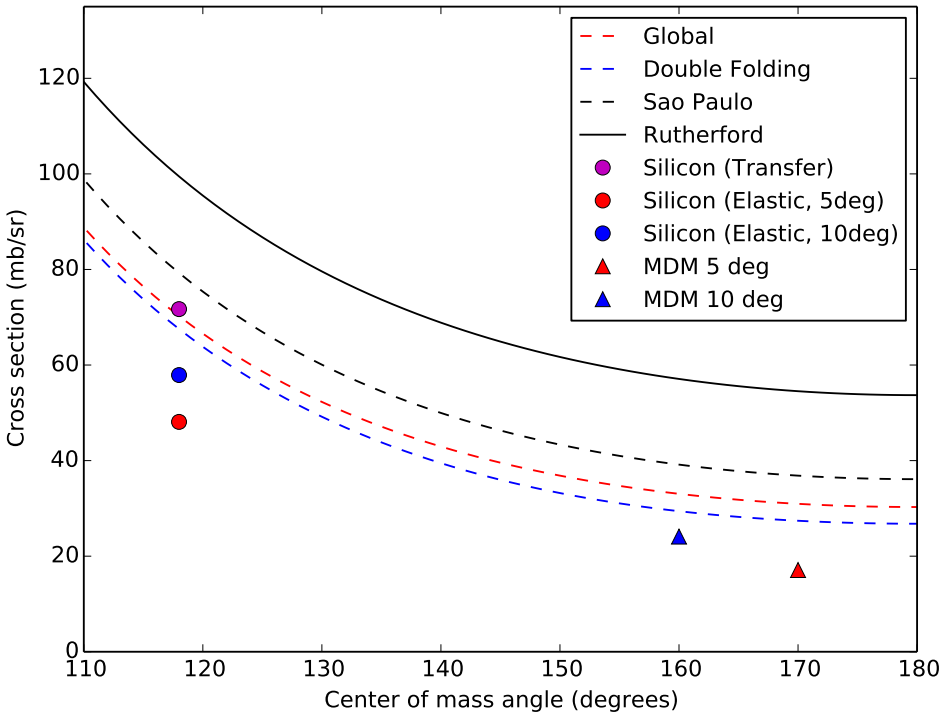

Figure 4.5: The Rutherford cross section (solid curve) along with elastic scattering cross sections calculated using optical model calculations (dashed curves) for 3 different entrance channel potentials. These individual points are the elastic cross sections calculated using nominal values for the 2nd quadrant of the silicon detector in the target chamber and for two different angles of the MDM spectrometer.

to 170° and 160° in the c.m frame, respectively. These five different cross section data points (3 for the silicon detector quadrant and 2 for the two angles of the MDM spectrometer) are shown in Figure 4.5. The measurements of detecting elastically scattered ^{6}Li using the MDM spectrometer was performed after the transfer reaction measurements. Hence, the reason that the nominal cross sections are lower compared to the theoretical cross sections could be due to the degradation of the thin ^{6}LiF targets. The large uncertainties introduced by the charge state of the beam and the target thickness results in the nominal cross sections to be lower than the theoretical cross sections.

The theoretical elastic scattering cross sections, calculated using three different entrance channel optical model potentials (dashed curves) using the code FRESCO [43] (described in detail in

Section 4.6), are also shown in Figure 4.5 along with the Rutherford cross section (solid curve). At the c.m angle for the silicon quadrant (118°), the theoretical cross section is about 70% of the Rutherford cross section. The difference is increased at larger angles. The systematic uncertainty due to the optical model parameters is about 20%. It is evaluated based on the variations of the calculated cross section when different potentials are used.

It can be seen from Figure 4.5 that the elastic scattering cross sections calculated using nominal values for target thickness, solid angle, etc. are in relative agreement with the cross sections calculated using theoretical models even without any application of normalization procedures. It also indicates that there is significant variation if one relies on the beam integral recorded by the Faraday cup (which was not electron suppressed). This is likely due to several factors, such as variations in beam geometry, and possible target degradation. We have employed the normalization to elastic scattering to avoid these uncertainties. It also has an additional important benefit of significantly reducing uncertainties associated with the choice of optical model potential in the entrance channel, as will be discussed later in this section.

Using the theoretically calculated elastic scattering cross section at the c.m. angle for the 2^{nd} quadrant of the silicon detector (which is about 70% of the Rutherford cross section), the number of background-subtracted ^{6}Li ions in the silicon detector, the solid angle for the silicon quadrant and the kinematic conversion between lab and c.m frames (k), the product of (It) in Equation 4.1 can be accurately calculated. The theoretical cross section is obtained using the global ^{6}Li optical model parameter set described in section 4.6.1.1.

The elastic scattering cross sections from FRESCO and the number of elastically-scattered ^{6}Li observed using the spectrometer can then be used in Equation 4.1 along with the previously calculated (It) factor to find the corresponding solid angle of the MDM spectrometer. Consistency of this method was checked using the measurements at both angles (5° and 10°) of the MDM spectrometer. The solid angles calculated for both of these were 1.01 and 1.11 msr respectively.

The error budget for the solid angle calculations is given in Table 4.1.

For these two measurements, elastically scattered ^{6}Li from the ^{6}LiF target was measured in

Quantity	Component	Statistical Error (%)	Systematic Error (%)
$\Delta\Omega_{MDM,5}$	Number of counts from silicon (N_{si})	$\pm$ 5.5	$\pm$ 4.5
	Number of counts from Oxford (N_{MDM})	$\pm$ 4	-
	Theoretical elastic cross section	-	$\pm$ 7
$\Delta\Omega_{MDM,10}$	Number of counts from silicon (N_{si})	$\pm$ 2.3	$\pm$ 4.5
	Number of counts from Oxford (N_{MDM})	$\pm$ 1.5	-
	Theoretical elastic cross section	-	$\pm$ 7

Table 4.1: The error analysis for the determination of the solid angle of the MDM spectrometer using elastic scattering measurements done at 5° and 10°.

the Oxford detector. The number of ^{6}Li particles measured in the detector for these cases along with corresponding number of elastic ^{6}Li measured in the 2nd quadrant of the silicon detector in the target chamber provides the statistical uncertainty. For both cases, the systematic error arises from the uncertainty of the theoretical elastic scattering cross sections ($\sim$ 7%) calculated using FRESCO, and the uncertainty in the number of counts in the ^{6}Li peak in the silicon detector after background subtraction. The final solid angle is taken as the weighted average between these two values, which is 1.09 $\pm$ 0.03(stat) $\pm$ 0.08(sys) msr.

4.2 Alpha transfer reaction measurements

To measure the ^{6}Li(^{22}Ne,d)^{26}Mg* reaction, the magnetic field of MDM Spectrometer was set for 6.5 to 7.5 MeV deuterons, the relevant energy ranges for populating the excitation energies of ^{26}Mg corresponding to the Gamow energy window for the ^{22}Ne(α,n) reaction in the AGB stars. The Gamow energy window for this reaction lies at $\sim$ 10.7 MeV - 11.4 MeV in excitation energies of ^{26}Mg.

The magnetic field setting for deuterons populating the center of the Gamow window was approximately found using the RAYTRACE code, and this value was set as the dipole field value of the MDM spectrometer. The deuterons were measured in the Oxford detector. Using the calibrated

positions for the four proportional counter wires and the MDMTRACE code, the energies and angles of the deuterons right after the target were reconstructed. The spectrum of deuterons is shown in Fig. 4.6.

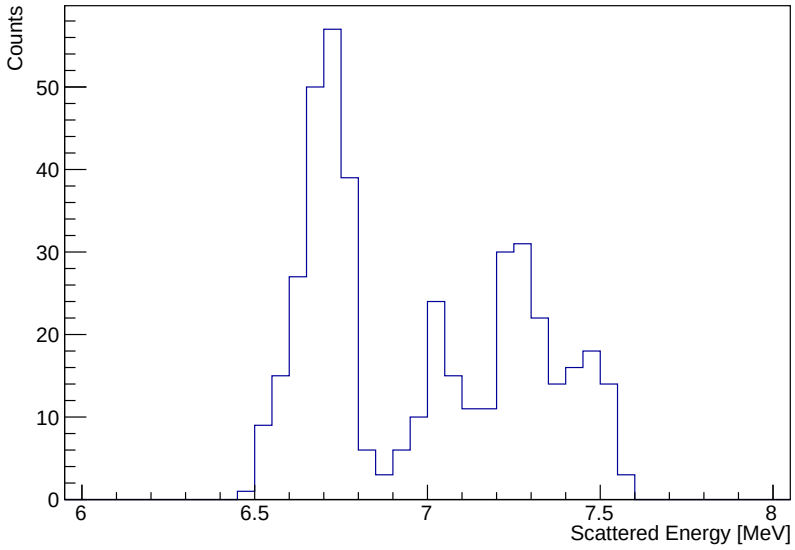

Figure 4.6: The deuteron energy spectrum reconstructed from the tracks in the Oxford detector for the ^{22}Ne(^{6}Li,d)^{26}Mg transfer reaction.

4.3 Analysis of the ^{26}Mg Excitation energies

Once the deuteron energies have been recreated using MDMTRACE (Figure 4.6), their energies at the center of the ^{6}LiF target are reconstructed using the energy losses through the carbon backing and half of the ^{6}LiF. After these energy losses are accounted for, the deuteron energies can be converted into excitation energies of ^{26}Mg.

$$Q = \frac{(M_3 + M_4)}{M_4} E_3 - \frac{(M_4 - M_1)}{M_4} E_1 - 2\cos\theta \frac{\sqrt{M_1 M_3 E_1 E_3}}{M_4} \tag{4.3}$$

Using the reconstructed deuteron energies and angles, the Q-value for each event can be calculated using Equation 4.3. The Q-value for a reaction is the amount of energy which is absorbed or

released during the nuclear reaction. Here, M is the mass and E is the energy. The subscripts are defined as follows: 1 = Beam particle, 2 = Target particle, 3 = Light recoil, 4 = Heavy recoil.

$$E_x = Q_0 - Q \tag{4.4}$$

Once the Q-values has been calculated, the corresponding excitation energies (E_x) can be found by subtracting this from the Q-value for the ground state of the heavy recoil (Q_0) as shown in Equation 4.4. The ground state Q-value is calculated using the masses of the individual particles involved.

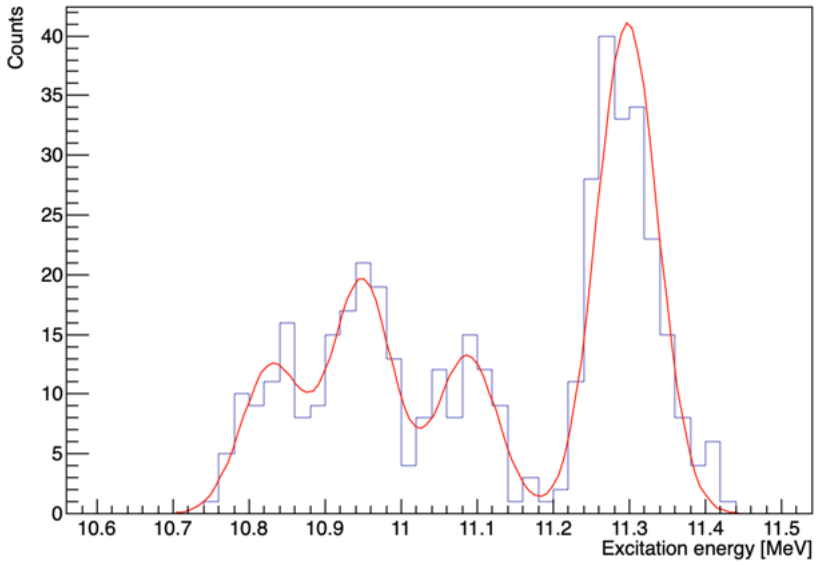

Figure 4.7: The excitation energy spectrum of ^{26}Mg reconstructed from deuteron energies for the ^{22}Ne(^{6}Li,d)^{26}Mg transfer reaction.

The reconstructed ^{26}Mg excitation energy spectrum from the ^{22}Ne(^{6}Li,d)^{26}Mg reaction is shown in Figure 4.7. The curve shown in this figure is a Gaussian fit for the four peaks. In order to obtain this curve, the isolated peak at 11.3 MeV in excitation energies was fitted with a Gaussian function ($f(x)$) and the width of that state was set as the width for all the 4 states.

$$f(x) = A\text{exp}\Big(- \frac{(x-b)^2}{2\sigma^2}\Big) \tag{4.5}$$

By fitting the peak at 11.3 MeV of Figure 4.7, a standard deviation for the peak (σ) was found to be $\sim$40 keV. Using this value, the full-width at half maximum (FWHM) experimental resolution is calculated as $2\sqrt{2\text{ln}2}\ \sigma$ = 94 keV. Then the curve in Figure 4.7 was obtained by combining four Gaussian fits with the standard deviations set to 40 keV centered at the respective peak locations obtained from individual gaussian fits. It is important to note that the same σ=40 keV was extracted also by fitting the spectrum obtained from track reconstruction of elastically scattered deuterons from the ^{197}Au target into the Oxford detector. This implies that the experimental resolution is mainly influenced by the detector resolution and the reconstruction procedure.

$$\text{Area of a Gaussian curve} = A \times \sigma \times \sqrt{2\pi} \tag{4.6}$$

Peak location (MeV)	Number of counts in the peak
11.30 (2)	206
11.08 (2)	66
10.95 (2)	98
10.83 (2)	62

Table 4.2: The excitation energies and the number of counts in the peaks for the excitation energy of ^{26}Mg.

Using the complete multi-Gaussian fit, the number of counts for each peak can be found using Equation 4.6 and the parameters from the fit. The peak locations and number of counts for each peak are listed in Table 4.2. Similarly to the solid angle calculations, the (It) normalization factor should also be found for the (^{6}Li,d) runs using the corresponding elastic scattering peak in the silicon quadrant (Figure 4.3).

Using the number of counts per each peak (N) and the solid angle of the spectrometer, combined with the (It) value established from elastic scattering (see previous section) the experimental cross sections for each resonance can be calculated using Equation 4.1. The corresponding cross section for the ^{6}Li(^{22}Ne,d)^{26}Mg reaction, performed at 21.7 MeV energy of ^{22}Ne beam and populating the near α-threshold states in ^{26}Mg is given in the Table 4.3.

Excitation energy (MeV)	Adopted values (MeV)	Experimental Cross section ($\mu b/sr$)
11.30 (2)	11.3195 (25) [a]	82 $\pm$ 6 (stat) $^{+13}_{-8}$ (sys)
11.08 (2)	11.08 (2) [b]	26 $\pm$ 3 (stat) $^{+4}_{-3}$ (sys)
10.95 (2)	10.95 (2) [b]	39 $\pm$ 4 (stat) $^{+6}_{-4}$ (sys)
10.83 (2)	10.82 (2) [b]	24 $\pm$ 3 (stat) $^{+4}_{-3}$ (sys)

Table 4.3: The cross sections of the peaks in the excitation energy spectrum of ^{26}Mg.
[a] Adopted from Ref. [9].
[b] Averaged between current and previous measurements (described within the chapter).

The statistical and systematic errors associated with the calculation of the (It) factor and the experimental cross sections are listed in Table 4.4. The statistical uncertainty for the (It) factor arises from the number of counts for elastically scattered ^{6}Li detected in the 2nd quadrant of the silicon detector placed at 31° from the beam axis in the target chamber. The systematic errors arises from: the different optical model potentials used to calculate the elastic scattering cross section at that angle, the uncertainty in the solid angle for that silicon quadrant and the uncertainty in the subtraction of the background from the spectrum of the Si detector at 31° to obtain the "true" number of elastically scattered ^{6}Li.

Quantity	Component	Statistical Error (%)	Systematic Error (%)
(It)	Number of counts from silicon (N_{si})	$\pm$ 0.4	$\pm$ 4.5
	Solid angle of the silicon detector quadrant ($\Delta\Omega$)	-	$\pm$ 2
	Theoretical elastic cross section	-	$^{+13}_{-3}$
$d\sigma/d\Omega$	(It) factor	$\pm$ 0.4	$^{+6}_{-14}$
	Solid angle of the MDM spectrometer ($\Delta\Omega_{MDM}$)	$\pm$ 3	$\pm$ 8
	Number of counts in the 11.30 MeV peak ($N_{11.30}$)	$\pm$ 7	-
	Number of counts in the 11.08 MeV peak ($N_{11.08}$)	$\pm$ 12	-
	Number of counts in the 10.95 MeV peak ($N_{10.95}$)	$\pm$ 10	-
	Number of counts in the 10.83 MeV peak ($N_{10.83}$)	$\pm$ 13	-

Table 4.4: The error analysis for the determination of the (It) factor and the experimental cross sections

4.4 Overview of previous direct measurements of ^{22}Ne(α,n) and ^{22}Ne(α,γ) reactions.

Several direct measurements to study the excitation functions of the ^{22}Ne(α,n)^{25}Mg reaction have been performed previously [32, 31, 27, 26]. Remarkable progress in suppressing the background was shown in the latest direct measurement by Ref. [4]. This work provides independent data on the partial α-widths for the lowest resonance observed in direct measurements at a center of mass energy of 704 keV for ^{22}Ne+α, corresponding to the 11.319 MeV excitation energy in ^{26}Mg (832 keV resonance energy E_α in Figure 4.8), and also for near α-threshold resonances at lower excitation energy. The (α,n) strength of the 11.3 MeV resonance was measured to be 118$\pm$11 μeV [4]. Additionally, a strong limit is given in Ref. [4] for another resonance located at 537 keV (11.152 MeV excitation energy in ^{26}Mg). The 11.15 MeV resonance has been previously reported in Ref. [5]. It is important to point out that neutron resonance strength measurements are inconsistent, ranging from 80(20) [31] to 200(36) [7] μeV. The Gamow energy window for the ^{22}Ne(α,n)^{25}Mg and ^{22}Ne(α,γ)^{26}Mg reactions lies between $\sim$200-800 keV in c.m. This range can-

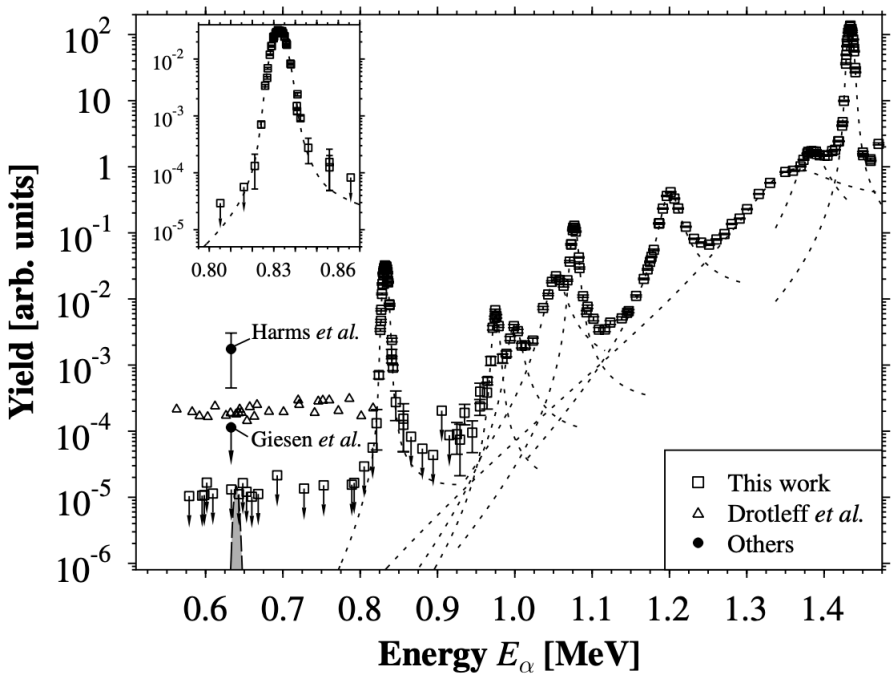

Figure 4.8: The excitation energy spectrum from a direct ^{22}Ne(α,n)^{25}Mg measurement from Ref. [4]

not be entirely covered by direct measurements due to the small cross section and high background conditions. Hence, the possible contributions from lower lying resonances of ^{26}Mg (below $E_{c.m}$ = 704 keV) have to be measured using indirect methods. The lowest resonance observed at 704 keV using direct measurements corresponds to the highest excitation energy peak in the spectrum from the present study. The present work covers the entirety of the Gamow energy window (Figure 4.7).

There have been previous direct studies to explore the ^{22}Ne(α,γ)^{26}Mg reaction as well. One prominent measurement was done by Ref. [26] where the 11.3 MeV state was measured at E_x = 11313.4 $\pm$ 4.2 keV (corresponding to E_α(lab) of 828 $\pm$ 5 keV, and a resonance strength of $\omega\gamma$ = 36 $\pm$ 4 μeV). Another more recent measurement was published in 2019 [9]. Here, the state at 11.3 MeV in the present study has been observed at E_x = 11319.5 $\pm$ 2.5 keV (corresponding to E_α(lab) = 835.2 $\pm$ 3.0 keV, and a resonance strength of $\omega\gamma$ = 46 $\pm$ 12 μeV). The weighted average between these two measurements is taken as the adopted resonance strength of the state for the (α, γ) reaction, $\omega\gamma$ = 37 $\pm$ 4 μeV for future discussions.

4.5 Comparison to the previous (^{6}Li,d) measurements performed at higher energies

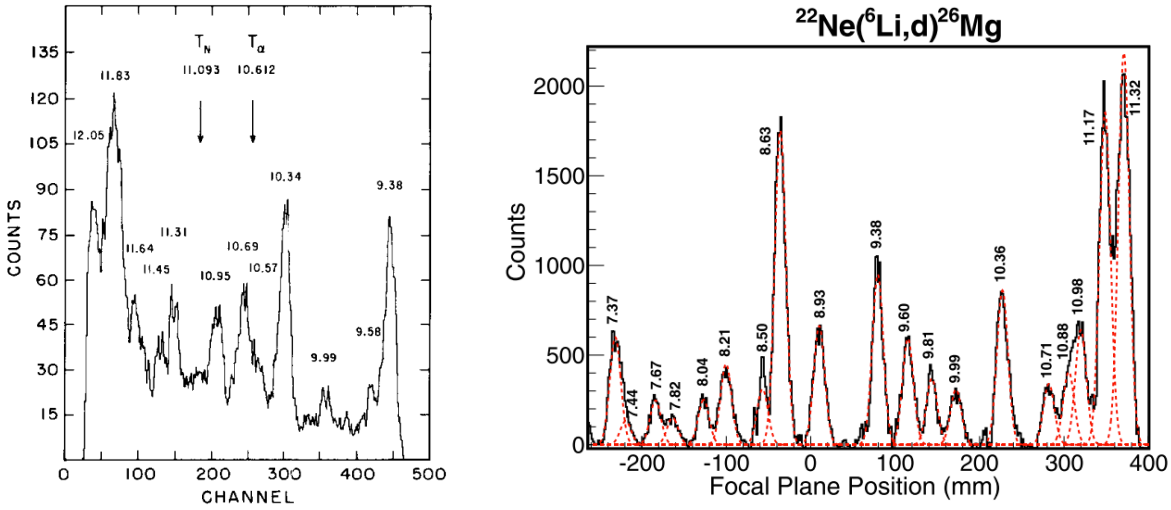

(a) (b)

Figure 4.9: Previously published ^{26}Mg excitation energy spectra for higher energies obtained by a) a 32 MeV measurement by Ref. [5] and b) a 82 MeV measurement by Ref. [6].

There have been several previous experimental efforts to use indirect techniques to study the resonances in ^{26}Mg which potentially could contribute to the reaction rates of the ^{22}Ne(α,n) and ^{22}Ne(α,γ) reactions. Some of these efforts include the use of the ^{22}Ne(^{6}Li,d) α-transfer reaction [5, 6, 67] to populate excited states of ^{26}Mg. Two previous measurements performed at two different energies were used for comparisons with the results of the current work; the most recent work by [6] which used a ^{6}Li beam of 82.3 MeV and another work by [5] which utilized a 32 MeV ^{6}Li beam. Additionally, the work by [6] provides details regarding an (α,α') inelastic scattering measurement to populate the states of ^{26}Mg using an alpha particle beam of 206 MeV. Due to the extremely high level density of ^{26}Mg in the excitation energy range of interest, it is difficult to uniquely link the states populated using the ^{26}Mg(α, α') reaction to those observed in ^{22}Ne(^{6}Li,d).

The peak at 11.3 MeV within the Gamow energy window is a common feature in all three measurements. It is dominant within the Gamow window in the current measurement and in Ref.

[6]. A significant difference between the excitation energy spectrum obtained in this dissertation and in Ref. [6] is a state at 11.17 MeV. In Ref. [6], this state is populated as strongly as the 11.3 MeV state. It is absent in the current measurements as well as in the 32 MeV measurement [5].

The state observed in the current measurement at 10.95 MeV is also present in both of the previous studies as well (10.95 MeV in [5] and 10.951(21) MeV in [6]). This peak has also been previously observed in Ref. [67] using the same ^{22}Ne(^{6}Li,d) alpha-transfer reaction with a 30 MeV beam of ^{6}Li, and is located at E_x=10.953(21) MeV. The excitation energy value observed in all 4 of these measurements (present work included) averages to 10.95(2) MeV which is used as the adopted value in Table 4.3.

The state at 10.83 MeV from the present study has also been seen in 2 previous (^{6}Li,d) studies, in Ref. [67] at E_x = 10.808(20) MeV and in Ref. [6] at 10.822(10) MeV. Since the uncertainties for these measurements are roughly similar to the present study as well as Ref. [67], the average of these are used as the adopted value for the excitation energy for this state in Table 4.3.

For the state at 11.08 MeV from the present study, it has been previously reported in Ref. [6] at 11.085(8) MeV. A similar approach as for the 10.95 and 10.83 MeV states is used here and an excitation energy of 11.084(20) MeV is adopted for the partial alpha width calculations (shown in Table 4.3).

4.6 Theoretical analysis of the cross sections

A DWBA analysis of the α-transfer reactions using code FRESCO was performed to determine the spin/parities and partial α-widths of the populated states. These calculations require knowledge of interaction potentials for the partitions given in Table 4.5. The choices of parameters for these potentials and uncertainties associated with these choices are described below.

Interaction	Description
Entrance Channel	^{22}Ne + ^{6}Li
Exit Channel	^{26}Mg + d
Core-Core	^{22}Ne + d
^{6}Li Form Factor	d + α
^{26}Mg Form Factor	^{22}Ne + α

Table 4.5: The various interactions for the ^{22}Ne(^{6}Li,d)^{26}Mg α-transfer reaction.

4.6.1 Entrance channel optical model parameters

Three different optical model parameterizations for the ^{22}Ne+^{6}Li partition were considered. Descriptions for each of these parameterizations are provided below. The entrance channel potentials play an important role because they are the dominant source of theoretical uncertainty for the analysis of the α-transfer reactions, as it will be clear from the discussion below.

4.6.1.1 Global ^{6}Li potentials

$$
\begin{aligned}
&V_0 = 109.5 \quad \text{MeV}, \\
&r_R = 1.326 \quad \text{fm}, \qquad a_R = 0.811 \quad \text{fm}, \\
&r_I = 1.534 \quad \text{fm}, \qquad a_I = 0.884 \quad \text{fm}, \\
&r_C = 1.3 \\
&W_0 = 58.16 - 0.328A + 0.00075A^2 \quad \text{MeV}
\end{aligned}
\tag{4.7}
$$

A set of global optical model potentials for ^{6}Li elastic scattering was provided by [68]. Here, V_0, W_0, r, a denote the real and imaginary potential depths, the reduced radius and the diffuseness,

respectively. The subscripts R and I denote the real and imaginary components. This has been accomplished by fitting a large set of experimental ^{6}Li elastic scattering data over a mass range of 24 - 208 and an energy range of 13 - 156 MeV. The parameters established in Ref. [68] are listed in Equation 4.7. Here, A is the atomic mass of the nuclei interacting with ^{6}Li.

4.6.1.2 Double-folding potentials

The double-folding potential model is described in 1979 by G. R. Satchler and W. G. Love [46]. An optical potential for a $A + b$ system ($U(R)$) appears in the Schrödinger equation:

$$\Big[-\frac{\hbar^2}{2\mu}\nabla^2 + U(R)\Big]\chi(R) = E\,\chi(R) \tag{4.8}$$

In Equation 4.8, μ is the reduced mass of the two particles, $\chi(R)$ is the wavefunction, R is the separation of the particles in the center of mass and E is the center of mass energy. When the proper boundary conditions are applied, $\chi(R)$ will be the elastic scattering between A and b. The total wavefunction of the $A + b$ system can be described using the internal eigenstates (ψ) of the separate nuclei.

$$\Psi = \sum_{i,j} \psi_{bi}\psi_{Aj}\chi_{ij}(R) \tag{4.9}$$

Here, i and j are the internal states of b and A, respectively. $\chi_{ij}(R)$ is the wave function that corresponds to the relative motion between the i and j states. When $i = j = 0$, χ_{00} represents elastic scattering. In order to obtain an equation similar to Equation 4.8 for χ_{00}, an effective potential U_{op} can be used.

$$U_{op} = U_F(R) + \Delta U \tag{4.10}$$

where,

$$U_F(R) = V_{00} = (\psi_{b0}\psi_{A0}|V|\psi_{b0}\psi_{A0}) \tag{4.11}$$

where the term $U_F(R)$ is called the *"folded potential"*. In a case where all the nucleons i are in

one nucleus and j is from the other, $U_F(R)$ can be described using the distributions of the center of mass of the nucleons in the ground state of each interacting nuclei (density distributions). Then for $U_F(R)$, since there is an integration over two separate densities, this is often called the *"Double-folding model"*. Hence the double-folding model derives the real and imaginary parts of the optical potentials from realistic nucleon-nucleon interactions and particle densities. More details can be found in Ref. [69].

4.6.1.3 São Paulo potentials

The São Paulo potential [70] is a theoretical model mainly used for heavy-ion interactions which uses the double-folding potential $U_F(R)$ described previously. The São Paulo potential (V^{SP}) can be used to describe various other reaction mechanisms in addition to elastic scattering (e.g. inelastic scattering, transfer reactions, etc.). This potential can be combined with coupled-channel calculations to describe elastic processes near the Coulomb barrier.

$$V^{SP}(R,E) = U_F(R) \times e^{-\frac{4v^2}{c^2}} \tag{4.12}$$

Equation 4.12 shows the form of the São Paulo potential. Here, c is the speed of light and v is the local velocity between two interacting nuclei.

$$v^2(R,E) = \frac{2}{\mu}\Big[E - V_C(R) - V^{SP}(R,E)\Big] \tag{4.13}$$

The velocity v is given by Equation 4.13. $V_C(R)$ is the Coulomb potential and E is the energy. By numerically solving Equations 4.12 and 4.13 in an iterative process, the São Paulo potential can be found.

4.6.2 Exit channel and core-core optical model parameters

A global fit for the optical model potentials for deuterons used for this work was provided by H. An and C. Cai in 2006 [71] for deuteron of energies E_d. This global fit was produced for incident deuteron energies up to 183 MeV and a mass range of A = 12-238. A χ^2 minimization routine to

minimize the deviation between the experimental data and the calculated cross section from the fit was used to obtain the fit parameters. The parameters from Ref. [71] are listed below in Equation 4.14, where the notation is described in Section 2.4.

$$
\begin{aligned}
V_R &= 91.85 - 0.249E_d + 0.000116E_d^2 + 0.642Z/A^{1/3} \\
W_D &= 10.83 - 0.0306E_d, \qquad W_S = 1.104 + 0.0622E_d, \\
V_{so} &= 3.557, \\
a_R &= 0.719 + 0.0126A^{1/3}, \qquad a_D = 0.531 + 0.062A^{1/3}, \\
a_S &= 0.855 - 0.100A^{1/3}, \\
r_R &= 1.152 - 0.00776A^{-1/3}, \qquad r_D = 1.334 + 0.152A^{-1/3}, \\
r_S &= 1.305 + 0.0997A^{-1/3}, \\
a_{so} &= 1.011, \qquad r_{so} = 0.972, \qquad r_C = 1.303.
\end{aligned}
\tag{4.14}
$$

Since the binding energy of deuteron is very low, most of the elastic scattering measurements are performed at higher energies ($\sim$5-10 MeV/u). Hence, the global fits for deuteron systems are much better for higher energies. For optical model calculations, apart from the real potential, the imaginary potential can be broken into many different scenarios such as surface, volume, etc. For transfer reactions, most of the time, it is the surface effect that contributes the most. Hence for low energies, the volume part could be safely ignored. In case of the compound nucleus contribution (described later), the volume term is important. In this case, the volume imaginary part has to be taken into account. Hence in a more realistic situation, both the surface and volume imaginary parts have to be considered. When going to lower energies where the accuracy of the global fits are unclear, it is a trade off between having a slightly more accurate fit with the volume term considered along with the addition of three more parameters (depth, radius, diffuseness) for higher uncertainties.

For this global fit, when the deuteron energy is increasing, the contribution of the real potential (V_R) decreases, the imaginary surface potential (W_D) decreases, and the imaginary volume

potential (W_S) increases (Equation 4.14).

4.6.3 Form factor potentials

Two different potential sets were chosen for the ^{22}Ne+α form factor. One is a potential with a larger interaction radius (potential A in Table 4.6) from [72], and the other is a potential which fits the partial alpha widths of α-cluster states in ^{16}O [73] (potential B in Table 4.6). In the work presented here, it is assumed that a good measure for a realistic upper limit for the α-cluster widths in ^{26}Mg is provided by potential B since this potential reproduces the width of a well-known strong α-cluster state. The potentials for the d+α system were obtained from Ref. [74].

The transfer reaction cross section for one state of ^{26}Mg at 11.30 MeV was calculated using FRESCO for the transfer of angular momenta $L = 0, 1, 2$ by the alpha particle using the three different entrance channel potentials described above. The transfer reaction cross section dependence for these three angular momenta are shown in Figure 4.10. Low angular momenta for the transferred particles were chosen due to the fact that a sub-Coulomb energy was used for this study (described in detail in Section 4.8). The global parametrization was chosen for further calculations for the entrance channel because it produced cross sections between the São Paulo and the double-folding potentials. The selection of this potential set over other parametrizations does not influence the principal conclusions of this work. As seen in Figure 4.10, the different optical model parameter sets for the entrance channel do not significantly change the shape of the angular distribution which is mainly governed by the Coulomb potential. The cross section at the higher center of mass angles varies roughly within 30% in magnitude. However, there is a partial cancellation of this theoretical uncertainty due to the normalization procedure adopted using elastic scattering measurements.

The final potential parameters chosen for the DWBA calculations are shown in Table 4.6.

4.7 Attempt to obtain spin / parity assignments for the 11.30 and 10.95 MeV states of ^{26}Mg

One of the difficulties regarding the evaluation of the astrophysical importance of resonances in ^{26}Mg for the ^{22}Ne(α,n) and ^{22}Ne(α,γ) reaction rates using indirect methods is the lack of definitive

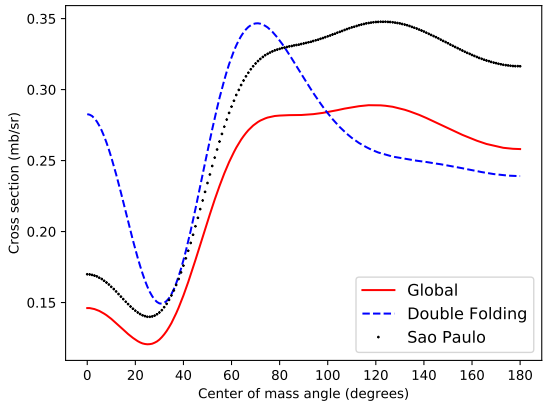

(a) L = 0

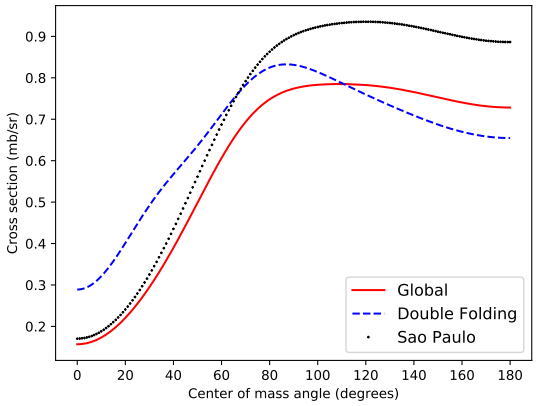

(b) L = 1

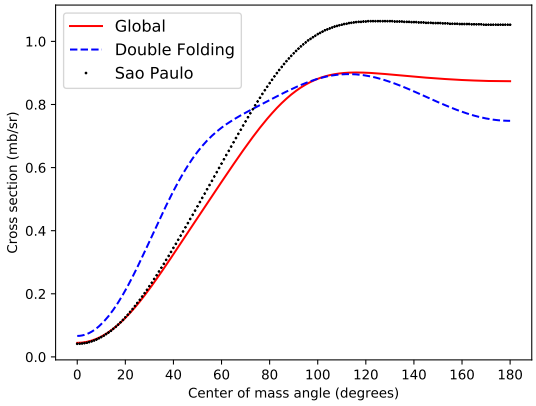

(c) L = 2

Figure 4.10: The angular distribution of the cross section for L=0, 1 and 2 angular momentum transfers.

Reaction Channel	V_0 (MeV)	r_r (fm)	a_r (fm)	W_s (MeV)	W_D (MeV)	r_I (fm)	a_I (fm)	r_C (fm)	V_{so} (MeV)	r_{so} (fm)	a_{so} (fm)	Ref.
^{22}Ne+^{6}Li	109.5	1.326	0.811	51.307		1.534	0.884	1.30				[68]
^{26}Mg+d	93.293	1.149	0.756	1.394		1.339	0.559	1.303				[71]
"					10.687	1.385	0.715		3.557	0.972	1.011	
^{22}Ne+d	79.5	1.25	0.8	10.0		1.25	0.8	1.25	6.0	1.25	0.8	[71]
α+d	85.0	1.25	0.68					1.25				[74]
A) ^{22}Ne+α	[a]	1.25	0.68					1.25				[72]
B) ^{22}Ne+α	[a]	1.23	0.6					1.25				[73]

Table 4.6: Optical model parameters used in the FRESCO calculations of the ^{22}Ne(^{6}Li,d)^{26}Mg reaction. All the radii r_x are given such that $R_x = r_x.A_T^{1/3}$, where x can be r (real part), I (imaginary part), C (Coulomb) or so (spin-orbit). Two different potential sets were used for the form factor ^{22}Ne+α (A & B).
[a] Adjusted to give the correct binding energy.

spin-parity J^{π} assignments for the states of ^{26}Mg within the Gamow energy window. Sensitivity of the angular distribution of the (^{6}Li,d) reactions to the transferred angular momenta is limited and model dependent. Additionally, it has been noted that for higher energies of ^{6}Li beam, there is a strong dependence of the spectroscopic factors on the optical potentials [75].

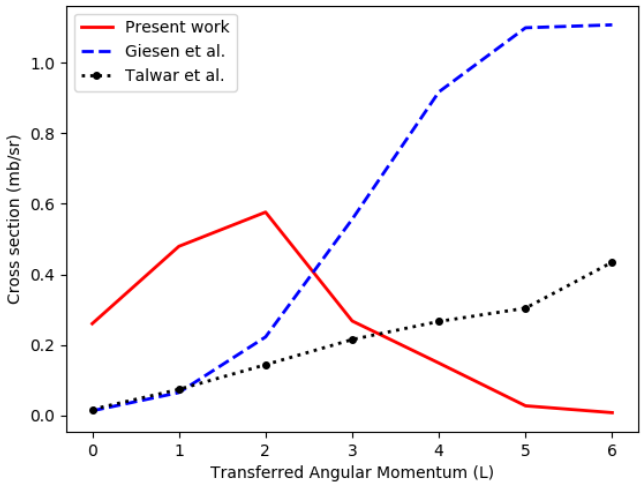

Figure 4.11: The transfer cross section for the 11.30 MeV state in ^{26}Mg for different transferred angular momenta using different center of mass energies, present work (solid line), 32 MeV data (dashed) and 82 MeV data (dotted)

A comparison is made between the results of the current measurement with the higher energy (^{6}Li,d) data mentioned previously in an attempt to constrain the spin-parities of the populated states of ^{26}Mg.

Figure 4.11 shows cross section calculations done using the three different energies of the three experimental studies for different transferred angular momenta of the α-cluster. The cross sections shown in this figure correspond to the respective center of mass angles of the observations in question: small angles of 8° for [5] and 0° for [6] for previously published data, and 170° for the present work. Each cross section calculation for the two higher energy data were performed using the optical model parameters provided in the respective publication.

The angular momentum of a grazing collision between two nuclei is given by $L = k_{eff}R = r_0(A_1^{1/3} + A_2^{1/3})\sqrt{(2\mu/\hbar)(E-B)}$ where A_1, A_2 are the masses of the nuclei involved, μ is the reduced mass, E is the energy and B is the Coulomb energy at the point of contact of the nuclear surfaces [76]. From this relation, it can be seen that an increase in the energy of ^{6}Li results in the possibility for higher transferred angular momenta. Hence, for the higher energies used by Refs. [5] and [6], population of higher spin states of ^{26}Mg is preferred. It should be noted that in the work by Ref. [6], the 11.3 and 11.17 MeV states are mentioned to have rapidly falling cross sections at larger angles and have only been observed at a single angle of zero degrees (along the beam axis). Hence, for further discussion of spin-parity assignments, data from Ref. [6] will only used for the lower lying excited states for further discussion.

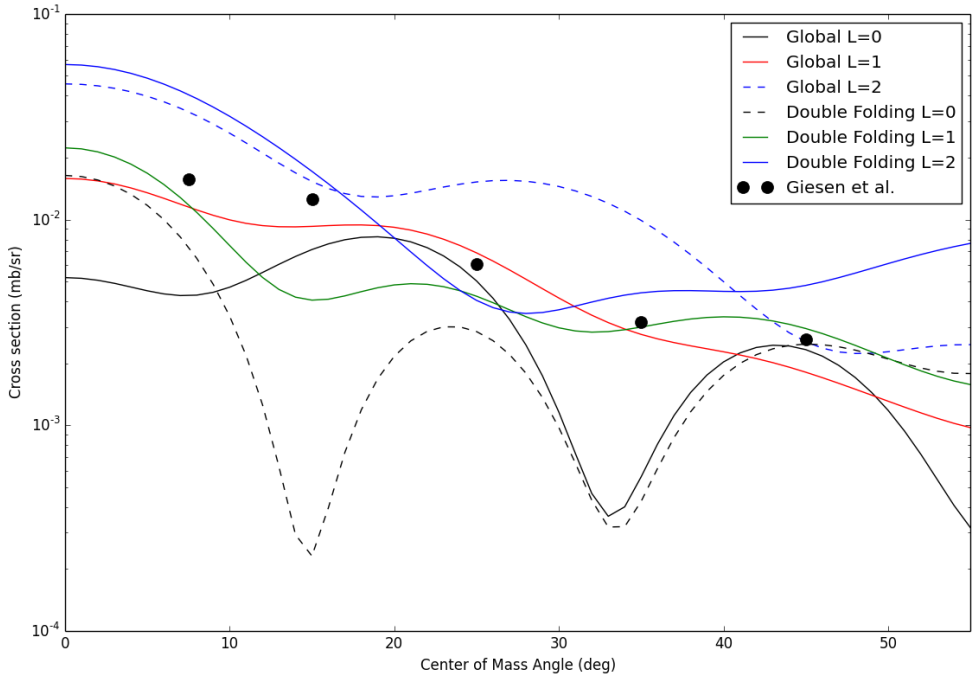

Figure 4.12: The transfer cross section distributions obtained for the global and double folding parameter sets for 32 MeV ^{6}Li beam (corresponding to a 117 MeV ^{22}Ne beam) scaled using the spectroscopic factors established from the present measurement. The points represent the experimental cross sections obtained by Giesen *et al* [5].

The spectroscopic factor for the 11.3 MeV state was calculated for the current measurement using the experimental cross section at 170° in center of mass and the theoretical cross sections calculated using the global and double folding potentials for three different angular momenta (L=0,1,2). Next, DWBA calculations were performed using the same optical model potential parameters for the energy used in the work of Giesen $et\ al.$ [5]. The theoretical cross sections obtained in this manner were scaled using the respective spectroscopic factors and plotted along with the experimental data obtained for the 32 MeV measurement. These scaled theoretical curves are shown in Figure 4.12.

It is seen from Figure 4.12 that none of the two DWBA cross section distributions for any choice of transferred angular momenta perfectly matches with the experimental data provided by Giesen $et\ al.$ It can also be seen here that the theoretical cross sections for the alpha transfer reaction are extremely model dependent at these energies and further development of better optical model potentials are needed for such cases.

It is also important to note that at the energies used by Giesen $et\ al.$, the experimental data could also have contributions from the compound nucleus reaction mechanism (indicative of the relatively smooth angular distribution reported) that would affect the final cross sections reported by the authors.

Hence, it can be concluded that using the spectroscopic factors from the current measurement, a definitive spin-parity assignment for the 11.3 MeV state of ^{26}Mg cannot be achieved.

4.8 Partial alpha widths of the states of ^{26}Mg

Theoretical cross sections for the sub-Coulomb ($E_{c.m.}$=4.7 MeV) ^{22}Ne(^{6}Li,d)^{26}Mg α-transfer reaction at 170° in the center of mass frame were calculated for different transferred angular momentum for the state at 11.30 MeV using the global ^{6}Li potentials (described in Section 4.6.1.1) for the entrance channel. These calculations, shown in Fig. 4.13, demonstrate that low transferred angular momenta (L less than 4) are preferred for the energies used for this study. The highest cross section is obtained for L=2. After this point, the cross section drops rapidly.

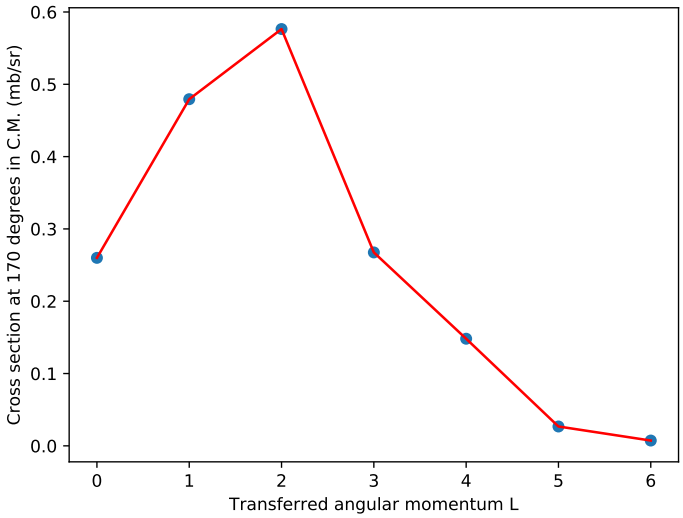

Figure 4.13: The α-transfer cross section at 170° in the center of mass for the 11.30 MeV state in ^{26}Mg for different transferred angular momenta.

4.8.1 Partial widths using the ANC technique

In order to calculate the partial widths of the excited states of ^{26}Mg, the wave functions for the ^{22}Ne+α form factors were initially generated using the optical model potentials listed in Table 4.6. The depth of the potentials were fitted individually for each state of interest in ^{26}Mg so that they would have the correct c.m. energy.

A typical shape of a wave function for the ^{22}Ne+α system is shown in Figure 4.14. As expected, the wave function will have an oscillatory pattern resulting from the nuclear potentials which defines the interactions of the nuclei at small distances. The amplitude of the wave function smooths out at asymptotic distances (further away from the core). The number of times the amplitude of the wave function crosses the zero value gives the number of radial nodes (N) of the wave function for which a minimum number is given by:

$$2(N-1)+L=\sum_{i=1}^{v}(2(n_i-1)+l_i) \tag{4.15}$$

The minimum number of radial nodes suitable for these wave functions while satisfying the

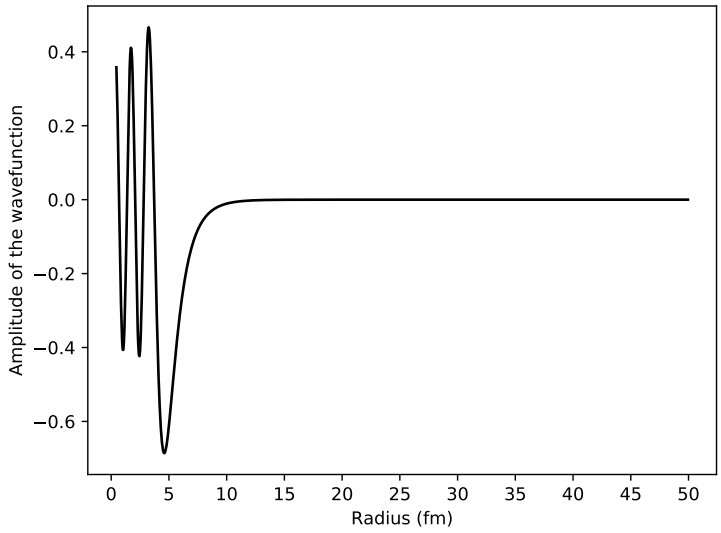

Figure 4.14: The shape of the nuclear wavefunction for the 11.3 MeV state.

Pauli principle were calculated using the Talmi-Moshinky transformation given in Equation 4.15 [77]. Here, n_i and l_i are the principle quantum number and angular momentum quantum number for the i^{th} nucleon of the transferred cluster with v number of nucleons. L is the transferred angular momenta by the alpha particle. All the constituent nucleons of an alpha particle transferred into the ground state of ^{22}Ne would occupy the $1d_{5/2}$ orbital of the sd-shell, giving $2N+L=8$ for positive parity states (even L) and $2N+L=9$ for negative parity states (odd L). For higher excitation levels, higher $2N+L$ values should be used. For the excited states of interest for the present study, $2N+L=12$ and $2N+L=11$ were used for positive and negative parity states respectively.

Using the number of nodes and various angular momenta of the α particle, the partial α widths (Γ_α) can be calculated using a formalism described in Section 2.8. DWBA codes such as FRESCO are designed to calculate the transfer cross sections only to bound states (positive binding energies). Since all the states of ^{26}Mg withing the Gamow energy window are unbound with respect to α decay, an artificial binding energy is used (bound state approximation) and a linear extrapolation to the correct resonance energy is then made. The extrapolation for the width of the 11.30 MeV state for a L=0 transfer is shown in Fig. 4.15.

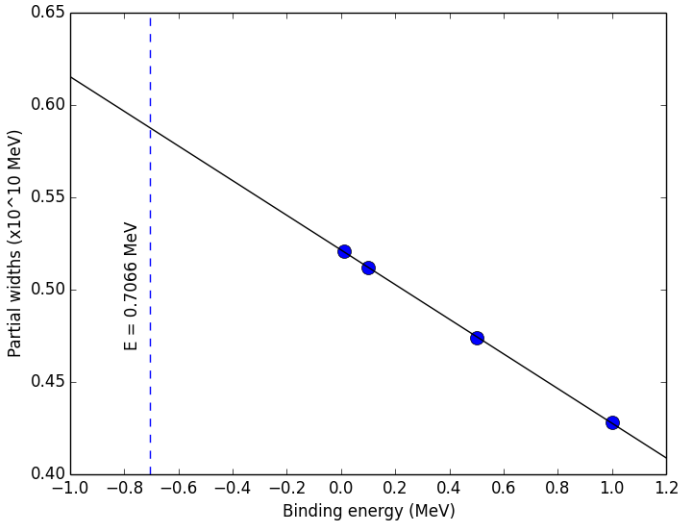

Figure 4.15: Partial α width as a function of binding energy for L=0 angular momentum transfer into the 11.30 MeV state of ^{26}Mg. The vertical dashed line represents the correct binding energy for this state.

An artificial parameter which is called the channel radius is defined to calculate the partial widths using the ANC approach. When using the R-matrix calculations, for radii higher than the channel radius, the solution for the wave function is analytical as the nuclear interaction is negligible and the Coulomb energy is the only contribution. So, it is important to use a channel radius that is large enough to escape the nuclear potential, but the exact values are still arbitrary and the dependence of the final result on the specific choice of this parameter needs to be elucidated. For the calculations of the partial α widths, the penetrability factor and the Whittaker function were calculated using a channel radius of R = 6.0 fm. This choice was made because it has been shown to reproduce the width of the known cluster states in neighboring nuclei [55]. It was evaluated that the uncertainty arising from this choice of the channel radius is $\sim$ 15 %, if it is varied between 5.5 and 6.5 fm.

It is important to point out that Γ_α from the direct ^{22}Ne(α,n) measurement in Ref. [4] (with the published assumption of an angular momentum transfer of L=2) and assuming that this state decays predominantly via neutron decay, is approximately equal to the upper limit of the α cluster

width (Wigner limit) for the state with Γ_α = 26 μeV. This is a very unlikely feature since there are no well-known states with low spins that have similar properties in neighboring nuclei to ^{26}Mg. Such a pure configuration of a low spin state for excitation energies around 12 MeV is highly unlikely to not mix with nearby states, which could provide a part of the cluster configuration. Due to this reason, an assumption is made in the present study that the transferred angular momentum in the ^{22}Ne(^{6}Li,d) reaction populating the 11.3 MeV state should be limited to L=2 or below. A more detailed discussion of the spin-parity assignment for the 11.3 MeV state will follow.

The method described previously to calculate the partial α widths using ANCs was applied for all the 4 states observed within the Gamow energy window. They are listed in Table 4.7. The error analysis for all the four states is shown in Table 4.8. For the three states observed below the neutron decay threshold (E_x = 11.093 MeV), the uncertainty for the calculated widths is dominated by the large uncertainty in resonance energies (20 keV). We expect that future studies will reduce this uncertainty by a factor of 10 (as in the case of the 11.3 MeV resonance) and therefore the uncertainties given in Tables 4.7 and 4.8 exclude the uncertainty due to resonance energy. This is done to highlight the uncertainties that result from these measurements of the (^{6}Li,d) and (^{7}Li,t) reactions, that were not designed to provide accurate excitation energies for the populated states. However, the final reaction rate uncertainties discussed in the next Chapter, will include the resonance energy uncertainty. The error budget for each resonance is shown in Table 4.8.

Table 4.8: The error analysis for the determination of the partial alpha widths for the states of ^{26}Mg in the Gamow energy window for different transferred angular momenta L.

E_R (MeV)	L	Component	Statistical Error (%)	Systematic Error (%)
11.319	0	Experimental cross section	$\pm$ 7	$^{+16}_{-10}$
		Resonance Energy	-	$\pm$ 8
		Channel Radius	-	$^{+11}_{-13}$
		Theoretical cross section	-	$\pm$ 14

Table 4.8 Continued

E_R (MeV)	L	Component	Statistical Error (%)	Systematic Error (%)
11.319	1	Experimental cross section	$\pm$ 7	$^{+16}_{-10}$
		Resonance Energy	-	$\pm$ 8
		Channel Radius	-	$\pm$ 15
		Theoretical cross section	-	$\pm$ 14
	2	Experimental cross section	$\pm$ 7	$^{+16}_{-10}$
		Resonance Energy	-	$\pm$ 8
		Channel Radius	-	$\pm$ 14
		Theoretical cross section	-	$\pm$ 14
11.080	0	Experimental cross section	$\pm$ 11	$^{+16}_{-10}$
		Channel Radius	-	$^{+5}_{-13}$
		Theoretical cross section	-	$\pm$ 14
	1	Experimental cross section	$\pm$ 12	$^{+16}_{-10}$
		Channel Radius	-	$^{+15}_{-13}$
		Theoretical cross section	-	$\pm$ 14
	2	Experimental cross section	$\pm$ 12	$^{+16}_{-10}$
		Channel Radius	-	$^{+13}_{-12}$
		Theoretical cross section	-	$\pm$ 14
10.950	0	Experimental cross section	$\pm$ 10	$^{+16}_{-10}$
		Channel Radius	-	$\pm$ 12
		Theoretical cross section	-	$\pm$ 14
	1	Experimental cross section	$\pm$ 10	$^{+16}_{-10}$
		Channel Radius	-	$\pm$ 12
		Theoretical cross section	-	$\pm$ 14
	2	Experimental cross section	$\pm$ 10	$^{+16}_{-10}$
		Channel Radius	-	$^{+12}_{-11}$
		Theoretical cross section	-	$\pm$ 14

Table 4.8 Continued

E_R (MeV)	L	Component	Statistical Error (%)	Systematic Error (%)
10.820	0	Experimental cross section	$\pm$ 12	$^{+16}_{-10}$
		Channel Radius	-	$^{+9}_{-10}$
		Theoretical cross section	-	$\pm$ 14
	1	Experimental cross section	$\pm$ 12	$^{+16}_{-10}$
		Channel Radius	-	$\pm$ 10
		Theoretical cross section	-	$\pm$ 14
	2	Experimental cross section	$\pm$ 12	$^{+16}_{-10}$
		Channel Radius	-	$\pm$ 10
		Theoretical cross section	-	$\pm$ 14

4.8.2 Resonance at 11.17 MeV excitation energy in ^{26}Mg

There have been many observations/predictions of a resonance at E_x = $\sim$11.15-11.17 MeV in previous direct and indirect measurements of the excitation levels of ^{26}Mg [4, 5, 6, 7, 34]. We have not observed this state, but an upper limit for its contribution can be established. A previous ^{22}Ne(α,n) direct measurement [4] has observed this level at E_x = 11152(10) keV. The highest reported excitation energy for this state using an alpha-transfer reaction is by Ref. [6] at 11167(8) keV using a ^{22}Ne(^{6}Li,d) measurement. An attempt to establish an upper limit to the width of this state is performed using the value from Ref. [6] for the excitation energy of this state (resonance energy 553(8) keV). From the present work, no more than 2 counts from Figure 4.7 can be attributed for this state at the energy of interest which can be used to calculate an upper limit for the width and resonance strength of this state. Assuming a Poisson distribution for the number of counts that can be attributed to the 11.17 MeV state, the "true" mean has to be below 5.8 at 95% confidence level. This value is used to calculate the upper limit for the experimental cross section for this state - 2 μb/sr.

E_R (MeV)	Transferred Momentum L	Γ_α (μeV)
11.319[a]	0	58 ± 4 (st.) $\pm$ 15 (sys.)
	1	13 ± 1 (st.) $\pm$ 3 (sys.)
	2	3 ± 1 (st.) $\pm$ 1 (sys.)
11.080[b]	0	$(1.3 \pm 0.1$ (st.) ± 0.3 (sys.)) x 10^{-3}
	1	$(2.5 \pm 0.3$ (st.) $^{+0.7}_{-0.5}$ (sys.)) x 10^{-4}
	2	$(5.7 \pm 0.7$ (st.) $^{+1.4}_{-1.2}$ (sys.)) x 10^{-5}
10.950[b]	0	$(9.6 \pm 1.0$ (st.) $^{+2.3}_{-1.9}$ (sys.)) x 10^{-8}
	1	$(2.0 \pm 0.2$ (st.) $^{+0.5}_{-0.4}$ (sys.)) x 10^{-8}
	2	$(0.5 \pm 0.1$ (st.) $^{+0.1}_{-0.1}$ (sys.)) x 10^{-8}
10.820[b]	0	$(3.8 \pm 0.5$ (st.) $^{+0.8}_{-0.7}$ (sys.)) x 10^{-15}
	1	$(7.4 \pm 0.9$ (st.) $^{+1.7}_{-1.4}$ (sys.)) x 10^{-16}
	2	$(1.5 \pm 0.2$ (st.) $^{+0.3}_{-0.3}$ (sys.)) x 10^{-16}

Table 4.7: Partial alpha widths of the states of ^{26}Mg calculated for the resonances observed within the Gamow window for different transferred angular momenta L.
[a] Changed later in the text after taking the weighted average using the (^{7}Li,t) measurement. Final values are shown in Table 4.12.
[b] Exact energies used for the partial alpha width calculations. The systematic error does not include the error from the uncertainty from the resonance strength.

The spin parity of this state in ^{26}Mg is not known. As is seen from the four resonances obtained from the present measurement, the widths and the resonance strengths are the largest for a J^π assignment of 0^+. This choice results in an upper limit for the width of the 11.17 MeV state of Γ_α = 6.5 x 10^{-3} μeV, assuming 553(8) keV center of mass resonance energy from Ref. [6], which is

the highest value reported for this resonance. In this manner, we have arrived at the absolute upper limit for the partial α width for this state.

4.9 Transfer reaction cross section dependence on optical model parameters

For the study of the ^{22}Ne(^{6}Li,d)^{26}Mg reaction, the beam energy of 21.7 MeV was chosen such that the center of mass energy will be below the Coulomb barrier to reduce the dependence of the results on the parameters used for the optical model potentials. The dependence of the theoretical cross sections on the various optical model parameters used for the entrance and exit channels is discussed in this section. This study was done for an angular momentum of L=0 for the transferred alpha particle into the 11.30 MeV state of ^{26}Mg. The values adopted for the final DWBA calculations (selected from the global optical model potentials for ^{6}Li [68] and deuterons [70] are shown by the dotted vertical lines in the plots below) were individually changed to see their effect on the theoretical cross section. The theoretical cross section was calculated at 170° in the center of mass frame (5° in the lab frame).

4.9.1 Coulomb radius

The dependence of the cross section on the Coulomb reduced radius parameter is shown in Figure 4.16. For the entrance channel as well as the d+α interaction channels, the Coulomb radius does not affect the reaction cross section at all (Figures 4.16a and 4.16d).

When the Coulomb radius is increased for the other two channels (Figures 4.16b and 4.16c) the calculated cross section is decreased, but the effect is very small (2%) as compared to the uncertainty due to the ^{6}Li+^{22}Ne potential parametrization.

4.9.2 Potentials in the entrance channel

For the present study, since the normalization is performed using the theoretical elastic scattering cross sections, the sensitivity of the choice of the entrance channel potentials in the transfer reaction cross sections are significantly reduced. The overall influence from the entrance channel potentials are estimated as 10%.

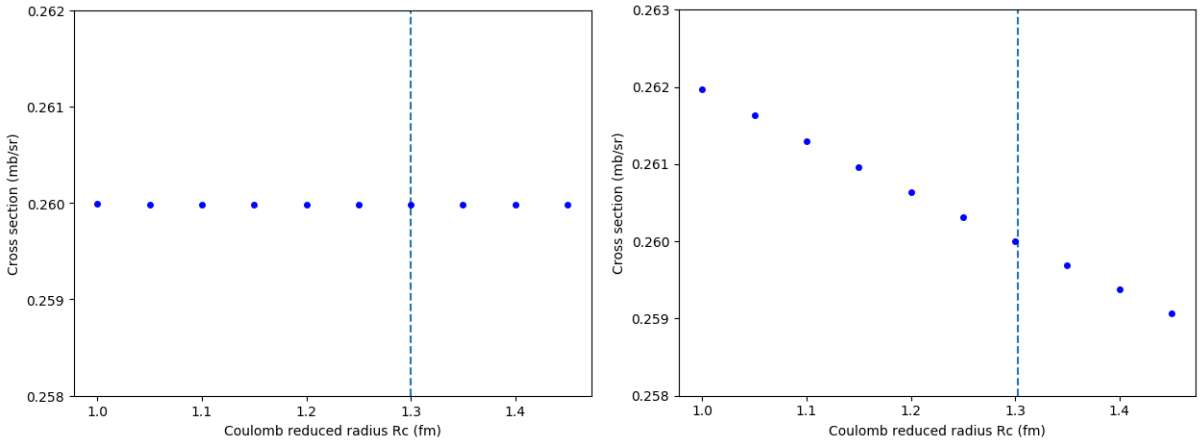

(a) Coulomb reduced radius for ^{22}Ne+^{6}Li

(b) Coulomb reduced radius for d+^{26}Mg

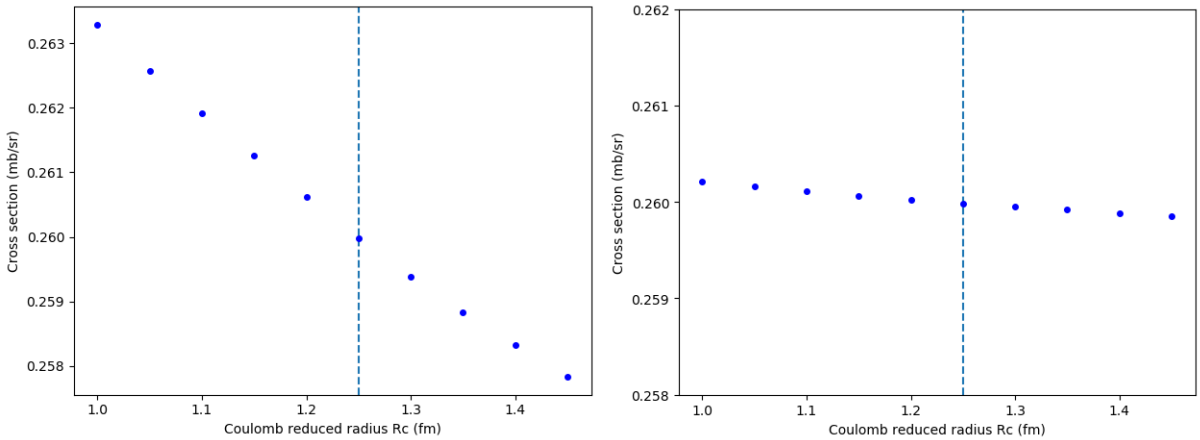

(c) Coulomb reduced radius for ^{22}Ne+α

(d) Coulomb reduced radius for d+α

Figure 4.16: The cross section dependence on the potential variation for the reduced radius of the Coulomb potentials for the various channels. The adopted values are denoted by the vertical lines.

4.9.3 Potential depth in the exit channel

In the case of the exit channel potentials, the most interesting dependence is shown in the imaginary potential part by the surface absorption (see Figure 4.17c). Since sub-Coulomb energies are used for this experimental measurement, the particle-transfer reaction mainly occurs as a peripheral reaction due to the presence of the Coulomb barrier. Hence the surface absorption will play a major role in the reaction cross section. As the depth of the surface potential is gradually increasing, the reaction cross section will gradually decrease until it reaches a point where further

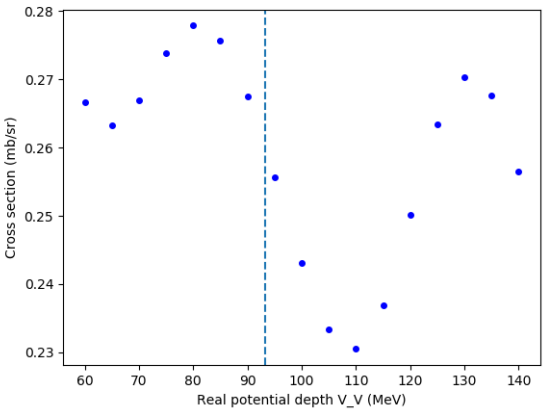

(a) Real volume depth

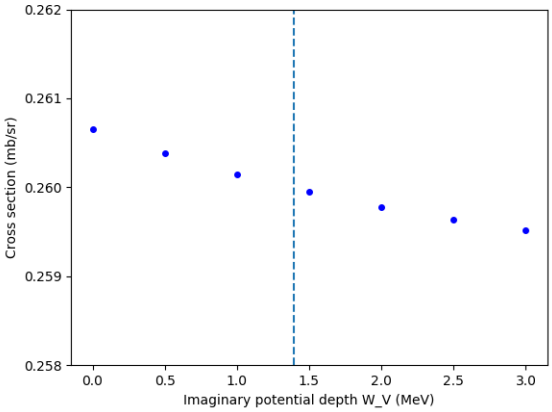

(b) Imaginary volume depth

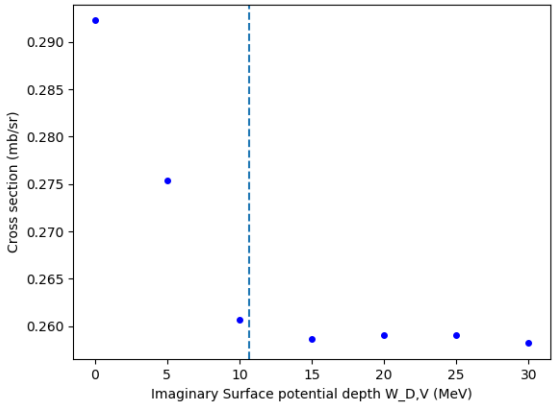

(c) Imaginary surface depth

Figure 4.17: The cross section dependence on the potential variation for the real and imaginary volume depth term of the exit channel potentials. The adopted values are denoted by the vertical lines.

penetration of the particle is hindered completely. At this point, the cross section of the reaction will no longer vary with the depth of the potential. This is clearly seen in Figure 4.17c. The depth of the real potential of the exit channel shows an oscillatory behavior (see Figure 4.17a). The dependence of the cross section on the imaginary potential from the volume absorption seems to be very small (see Figure 4.17b). Overall, the influence of the variation of the d+^{26}Mg potential parameters are generally within 10%.

4.9.4 Reduced radius of the exit channel potentials

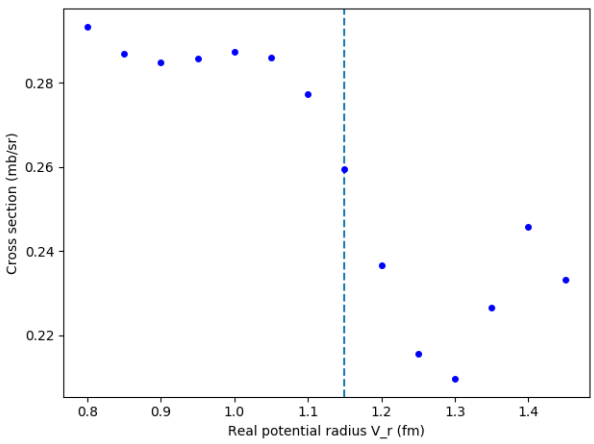

(a) Real volume reduced radius

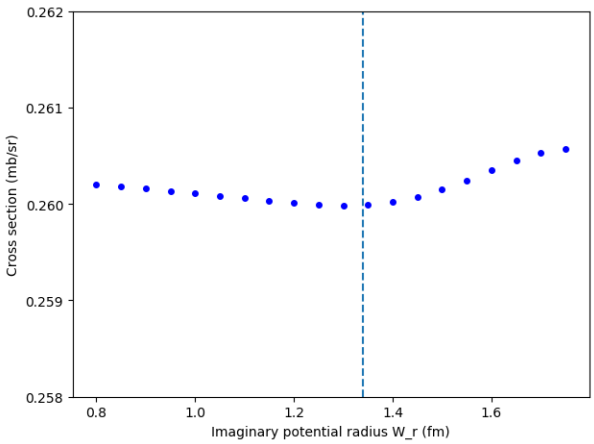

(b) Imaginary volume reduced radius

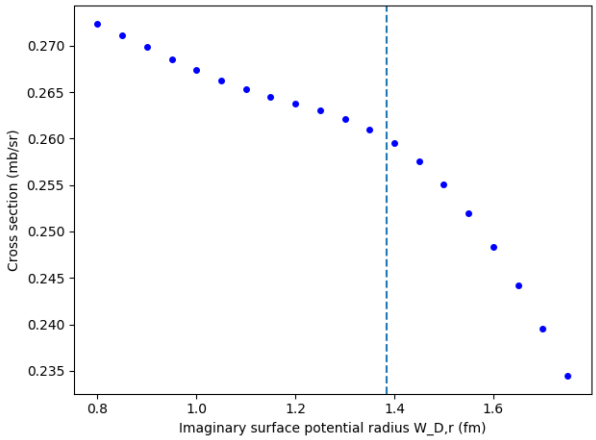

(c) Imaginary surface reduced radius

Figure 4.18: The cross section dependence on the potential variation for the real and imaginary reduced radius term of the exit channel potentials. The adopted values are denoted by the vertical lines.

The cross section dependence of the reduced radius parameter of the potentials of the exit channel are shown in Figure 4.18. The reduced radius of the real volume potential (Fig. 4.18a) showcases a similar oscillatory behavior followed by the depth of the same potential (see Figure 4.17a). The reduced radius of the imaginary volume potential does not show a significant effect on

the reaction cross section. The overall variation is still significantly below the dependence on the entrance channel potentials.

From Figures 4.16 - 4.18, it can be concluded that the final results are most sensitive to the parameters of the exit channel (d+^{26}Mg) optical model potentials. None of the other potential parameters influence the theoretical cross section at the same level. A final uncertainty of 14% is adopted for the theoretical uncertainty.

4.10 Compound nucleus mechanism

An important check that needs to be done at this stage is to see if there is any contribution for this measurement from a compound nucleus reaction mechanism. A compound nucleus reaction is one where two nuclei will combine together to create a single "compound" nucleus system in highly excited state. This was first introduced by Niels Bohr in 1936. In most cases, the created compound nucleus will have a relatively long lifetime and it will 'forget' the mechanism which formed it. These collisions lead to a thermally equilibrated state within the compound nucleus.

$$A + b \rightarrow C^* \rightarrow a + B \tag{4.16}$$

For the system described in Section 2.3, the reaction mechanism would be modified as above to include the compound nucleus (C^*). These reactions can be described in two stages: the formation of the compound nucleus ($\sigma_{A+b\rightarrow C^*}$) and the probability of the decay of the compound nucleus ($P_{C^*\rightarrow a+B}$). The cross section of this reaction would be given by the product of these two factors.

Since a compound nucleus in thermal equilibrium has no memory of the mechanism involved in creating it, the mode of decay of the compound nucleus is entirely independent of the method of its creation. Hence, no information on the partial α-widths of the states in ^{26}Mg can be extracted from this experiment if the compound nucleus is the dominant mechanism for the reaction in question.

In the case of the ^{22}Ne+^{6}Li reaction, the compound nucleus that would be created is ^{28}Al. In order to elucidate the influence of the compound nucleus mechanism, another measurement was done concurrently with the ^{22}Ne(^{6}Li,d)^{26}Mg, utilizing the ^{7}LiF target. Using this target and the

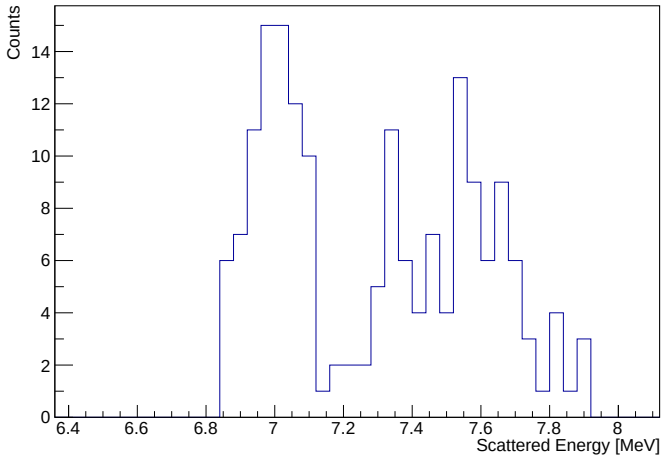

Figure 4.19: The triton energy spectrum reconstructed from the tracks in the Oxford detector for the ^{22}Ne(^{7}Li,t)^{26}Mg transfer reaction.

same ^{22}Ne beam, a similar α-particle transfer reaction of ^{22}Ne(^{7}Li,t)^{26}Mg was carried out (with lower statistics), which populated the same excitation energy window of ^{26}Mg as the previous reaction. The ^{7}Li nucleus has an $\alpha - t$ structure [78] with an alpha binding energy of 2.47 MeV. In this case, if there is a contribution from a compound nucleus, the spectrum of tritons should be very different from that in Figure 4.6 due to the fact that the compound system would be an entirely different isotope (^{29}Al) and there is no reason for triton evaporation from the highly excited states in ^{29}Al to lead to the same states in ^{26}Mg as deuteron evaporation from ^{28}Al.

Figure 4.19 shows the triton energy spectrum reconstructed from the tracks in the Oxford detector for the ^{22}Ne(^{7}Li,t)^{26}Mg transfer reaction. Figures 4.6 and 4.19 show a very dominant resonance in the 6-7 MeV region which translates to the same 11.3 MeV excited state of ^{26}Mg. The dominance of the 11.3 MeV state in both spectra serves as an indication of the dominance of the same α-cluster transfer reaction mechanism. Similarities between the spectrum of states populated in the (^{6}Li,d) and (^{7}Li,t) reactions can be used as an argument for the dominant role of direct α-transfer reaction mechanism. To make a quantitative comparison, the partial α-width for the 11.3 MeV resonance obtained in two different reactions can be used as a consistency check.

In order to calculate the cross section for the ^{26}Mg peak at 11.3 MeV, the same normalization

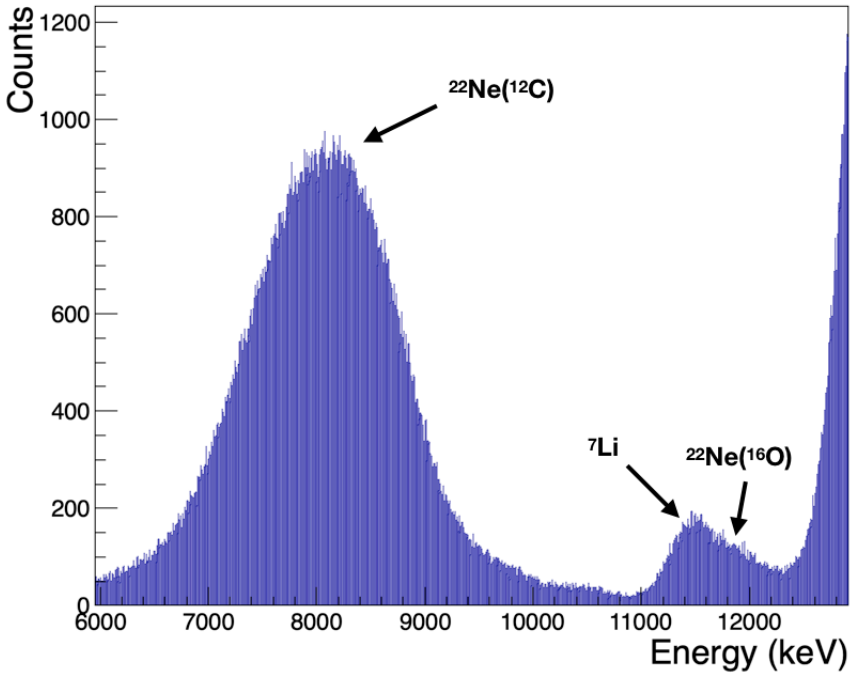

Figure 4.20: The calibrated energy spectrum from the 2[nd]quadrant of the silicon detector for the ^{22}Ne(^{7}Li,t)^{26}Mg transfer reaction.

procedure tat was carried out for the (^{6}Li,d) measurement using the silicon detector located in the target chamber is used. There is no definitive elastic ^{7}Li peak in the silicon detector (see Figure 4.20) at the angle of the silicon quadrant (31°). The elastically scattered ^{7}Li peak is overlapping with ^{22}Ne beam particles elastically scattered from the oxygen (^{16}O) in the water molecules spread out in the target due to the hydroscopic nature of LiF.

$$
\begin{aligned}
V_0 &= 114.2 \quad \text{MeV}, \\
r_R &= 1.286 \quad \text{fm}, \qquad a_R = 0.853 \quad \text{fm}, \\
r_I &= 1.739 \quad \text{fm}, \qquad a_I = 0.809 \quad \text{fm}, \\
r_C &= 1.3 \\
W_0 &= 40.13 - 0.341A + 0.00093A^2 \quad \text{MeV}
\end{aligned}
\tag{4.17}
$$

Figure 4.21 shows Gaussian fits to separate the elastic ^{7}Li peak from the elastic ^{22}Ne peak. The number of counts in the ^{7}Li peak after this fit, is used to calculate the (It) factor. The ^{22}Ne+^{7}Li

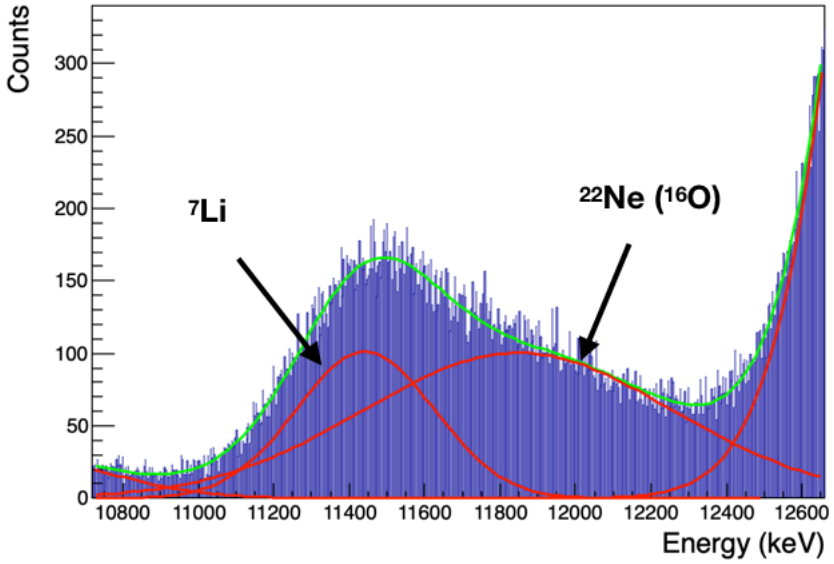

Figure 4.21: The calibrated energy spectrum from the 2[nd]quadrant of the silicon detector for the ^{22}Ne(^{7}Li,t)^{26}Mg transfer reaction.

elastic scattering cross section was calculated using FRESCO with the global ^{7}Li optical potential set (see Equation 4.17, the parameters of which are described in Section 2.4) provided in Ref. [68]. Unlike the ^{22}Ne+^{6}Li case where the elastic scattering cross section is $\sim$ 70% of the Rutherford cross section at higher c.m angles, it is roughly 30% for ^{22}Ne+^{7}Li. Using this calculated cross section, the number of counts measured in the silicon quadrant 2 and the solid angle of the quadrant, the (It) factor can be found using Equation 4.1. Using this (It) factor, the experimental cross section for populating the 11.3 MeV resonance in ^{26}Mg using the (^{7}Li,t) reaction was found to be 59 $\pm$ 7 (stat.) $\pm$ 6 (sys.) μb/sr. The error analysis for the experimental cross section for the 11.3 MeV state is given in Table 4.9.

Once the experimental cross section for this resonance is known, the theoretical cross section can be calculated using various potentials for the exit channel. Four different exit channel optical model parameters were used for the t+^{26}Mg channel: one from the global triton optical potentials published in Ref. [79] and three from Ref. [80]. The core-core (^{22}Ne+t) optical potential parameters were also obtained from Ref. [80].

Quantity	Component	Statistical Error (%)	Systematic Error (%)
	Number of counts from silicon (N_{si})	$\pm$ 0.9	$\pm$ 4.5
(It)	Solid angle of the silicon detector quadrant ($\Delta\Omega$)	-	$\pm$ 2
	(It) factor	$\pm$ 0.9	$\pm$ 5
	Solid angle of the MDM spectrometer ($\Delta\Omega_{MDM}$)	$\pm$ 3	$\pm$ 8
$d\sigma/d\Omega$	Number of counts in the 11.30 MeV peak	$\pm$ 11	-

Table 4.9: The error analysis for the determination of the (It) factor and the experimental cross section for the (^{7}Li,t) measurement.

Using these four exit channel parameter sets, the partial alpha width (Γ_α) of the 11.3 MeV state of ^{26}Mg can be calculated for L = 0,1 and 2 transferred-angular momenta using the formalism described in Section 2.8, and the extrapolation used for the (^{6}Li,d) described in Section 4.8.1. The center of the range of the four widths was considered as the width of the state for a given transferred angular momentum. The widths found in this manner for the 11.3 MeV state for L=0,1,2 are listed below in Table 4.10.

Angular Momentum (L)	Γ_α (μeV)
0	64 $\pm$ 7 (stat.) $\pm$ 14 (sys.)
1	13 $\pm$ 1 (stat.) $\pm$ 3 (sys.)
2	3 $\pm$ 1 (stat.) $\pm$ 1 (sys.)

Table 4.10: The partial alpha widths calculated for the 11.3 MeV state of ^{26}Mg using the (^{7}Li,t) measurement.

The statistical error for the experimental cross section for the 11.3 MeV state using the (^{7}Li,t) measurement is determined by the number of elastically scattered ^{7}Li particles as well as the tritons from the (^{7}Li,t) reaction in the Oxford detector. The error analysis of the partial widths are shown

Quantity	Component	Statistical Error (%)	Systematic Error (%)
Γ_α (L=0)	Experimental cross section	$\pm$ 11	$\pm$ 9
	Resonance energy	-	$\pm$ 7
	Channel radius	-	$\pm$ 13
	Theoretical cross section	-	$\pm$ 11
Γ_α (L=1)	Experimental cross section	$\pm$ 11	$\pm$ 9
	Resonance energy	-	$\pm$ 7
	Channel radius	-	$\pm$ 15
	Theoretical cross section	-	$\pm$ 12
Γ_α (L=2)	Experimental cross section	$\pm$ 11	$\pm$ 9
	Resonance energy	-	$\pm$ 7
	Channel radius	-	$\pm$ 14
	Theoretical cross section	-	$\pm$ 12

Table 4.11: The error analysis for the determination of the experimental cross section and widths for the 11.3 MeV state in ^{26}Mg using the (^{7}Li,t) measurement.

in Table 4.11.

The partial alpha width (Γ_α) found using the (^{7}Li,t) measurement for the 11.3 MeV state agrees within error bars with the widths obtained for the same state using the (^{6}Li,d) measurement. This shows that the contribution from the compound nucleus mechanism for the sub-Coulomb α transfer reaction for (^{6}Li,d) and (^{7}Li,t) should be negligible.

The weighted average of the alpha partial widths obtained from the (^{6}Li,d) and (^{7}Li,t) measurements for the 11.3 MeV state of ^{26}Mg is taken as the final widths for this state. The averaged widths are shown in Table 4.12.

The reaction rates of the ^{22}Ne(α,n)^{25}Mg and ^{22}Ne(α,γ)^{26}Mg reactions are proportional to the resonance strengths and the partial α-width (Γ_α) of the resonances in ^{26}Mg. In the approximation of a narrow resonance, the resonance strengths for the (α, n) and (α, γ) reactions can be calculated

Angular Momentum (L)	Γ_α (μeV)
0	61 ± 4 (stat.) $\pm$ 10 (sys.)
1	13 ± 1 (stat.) $\pm$ 2 (sys.)
2	3 ± 1 (stat.) $\pm$ 1 (sys.)

Table 4.12: The partial alpha widths calculated for the 11.3 MeV state of ^{26}Mg as a weighted avegrage between the widths obtained from the (^{6}Li,d) and (^{7}Li,t) measurements.

using the partial widths, the total width of the state (Γ) and the spins of the particles (J's) as follows:

$$\omega\gamma_{(\alpha,n)} = \frac{2J+1}{(2J_1+1)(2J_2+1)}\frac{\Gamma_\alpha\Gamma_n}{\Gamma} \tag{4.18a}$$

$$\omega\gamma_{(\alpha,\gamma)} = \frac{2J+1}{(2J_1+1)(2J_2+1)}\frac{\Gamma_\alpha\Gamma_\gamma}{\Gamma} \tag{4.18b}$$

Here, J is the spin of the resonance and $J_1 = J_2 = 0$ are the spins of the ^{22}Ne and α particles. $\Gamma_\alpha, \Gamma_\gamma, \Gamma_n$ are the partial widths for alpha, gamma and neutron decays, respectively.

For neutron bound states (states below the neutron decay threshold), the total width is $\Gamma = \Gamma_\alpha + \Gamma_\gamma$. For neutron unbound states, the total width is $\Gamma = \Gamma_\alpha + \Gamma_\gamma + \Gamma_n$. For low energy resonances where the penetrability of an α particle through the Coulomb barrier is very small, Γ_α is much smaller than the neutron and γ partial widths. For neutron unbound states, the ratio of neutron and gamma widths can be found using the ratio of the resonance strengths of those states as follows:

$$\frac{\omega\gamma_{(\alpha,n)}}{\omega\gamma_{(\alpha,\gamma)}} = \frac{\Gamma_n}{\Gamma_\gamma} \tag{4.19}$$

For low energy resonances ($\Gamma_\alpha \ll \Gamma_n$ and Γ_γ), the resonance strength for neutron unbound states can be written as follows:

$$\omega\gamma_{(\alpha,n)} \approx (2J+1)\frac{\Gamma_\alpha}{1+\Gamma_\gamma/\Gamma_n} \tag{4.20a}$$

$$\omega\gamma_{(\alpha,\gamma)} \approx (2J+1)\frac{\Gamma_\alpha}{1+\Gamma_n/\Gamma_\gamma} \tag{4.20b}$$

For the neutron bound states that contribute to the (α,γ) reaction, the resonance strength is then $\omega\gamma_{(\alpha,\gamma)} \approx (2J+1)\,\Gamma_\alpha$.

4.11 Spin-parity assignment of the 11.3 MeV state using comparison to the direct ^{22}Ne(α,γ) measurements

As mentioned previously, the only resonance observed within the Gamow energy window for the ^{22}Ne(α,γ) reaction using direct measurements is the state at 11.3 MeV. The strength of this resonance has been reported by two direct measurements (Refs. [9] and [26]). The weighted average between these two reported strengths is $\omega\gamma_{(\alpha,\gamma)}$ = 37 $\pm$ 4 μeV. By using this strength in Equation 4.20 along with a recent Γ_n/Γ_γ value of 1.25 $\pm$ 0.28 from Ref. [81], the partial alpha width of the state can be calculated as 83(13), 28(5), and 17(3) μeV for L = 0, 1 and 2, respectively. The partial α-width for the 11.3 MeV state obtained in the present study (see Table 4.7) is in agreement within error bars (although, outside of 1σ) with the widths calculated from the direct ^{22}Ne(α,γ) measurements but only for the L=0 case - yielding the likely 0^+ spin-parity assignment for the 11.3 MeV state. The L=1 assignment would produce close to 3σ discrepancy, and the L=2 would lead to almost 5σ discrepancy. Therefore, we exclude the L=2 assignment, but we cannot rule out the L=1 ($J^\pi = 1^-$).

The other three resonances within the Gamow energy window have not so far been measured directly.

4.12 Comparison of neutron strengths with previous direct measurements

Out of the four resonances observed within the Gamow energy window in the present work, only the 11.3 MeV state is above the neutron decay threshold of E_x = 11093.08(4) keV. Hence, this

is the only resonance that will contribute to the ^{22}Ne(α,n)^{25}Mg reaction. There have been several previous attempts to measure the neutron strength of this state (Refs. [4, 31, 82]). Out of these, the work by Jaeger $et.al.$ (Ref. [4]) shows remarkable background suppression in measuring the relevant states of ^{26}Mg for the ^{22}Ne(α,n)^{25}Mg reaction. This work provides a strength of $\omega\gamma_{(\alpha,n)}$ = 118 $\pm$ 11 μeV for the 11.3 MeV state. The work by Ref. [82] provides the lowest measured strength for this state at a value of 80 $\pm$ 20 μeV for this state.

It is important to note here that if the weighted average of the gamma strength for the 11.3 MeV state $\omega\gamma_{(\alpha,\gamma)}$ = 37 $\pm$ 4 μeV from previous measurements is used along with Γ_n/Γ_γ value of 1.25 $\pm$ 0.28 from Ref. [81] in Equation 4.20, the resulting neutron decay strength would be $\omega\gamma_{(\alpha,n)}$ = 46 $\pm$ 12 μeV. This value is within 2σ of the minimum strength for this resonance published by Ref. [82], but certainly disagrees with all other direct measurements of the (α,n) strength for this resonance. If the result from the present sub-Coulomb (^{6}Li,d) measurement and the Γ_n/Γ_γ from Ref. [81] are adopted, the $\omega\gamma_{(\alpha,n)}$ would be 34 $\pm$ 7 μeV. In either case, the (α,n) resonance strength for the 11.3 MeV state is much lower than previously reported values.

4.13 Conclusion

The ^{22}Ne(α,n) and ^{22}Ne(α,γ) reactions were studied using the ^{22}Ne(^{6}Li,d) reaction in inverse kinematics using sub-Coulomb energies. Four resonances in ^{26}Mg were observed within the Gamow energy window, for which the partial alpha widths have been calculated. The consistency of the partial width of the 11.3 MeV state using the ^{22}Ne(^{6}Li,d) reaction has been checked using the ^{22}Ne(^{7}Li,t) reaction populating the same states in ^{26}Mg. An upper bound for the partial alpha width of a state at 11.17 MeV is provided.

The dependence of the partial alpha widths of the states on the parameters chosen for the entrance channel (^{22}Ne+^{6}Li) is significantly reduced by using a beam and target normalization to the elastic scattering measurements.

Only the 11.3 MeV state (and possibly 11.17 MeV state) contribute to the ^{22}Ne(α,n) reaction. The 11.3 MeV resonance strengths were found using the partial alpha widths of the state for different angular momenta and the γ/n branching ratio from Ref. [81]. The values obtained for the

resonance strengths of this state are lower than the values previously reported from direct ^{22}Ne(α,n) measurements. However, it is in good agreement with the strengths observed for this state using direct ^{22}Ne(α,γ) measurements if 0^+ spin-parity assignment is assumed. The 1^- assignment cannot be excluded, but it results in 3σ discrepancy between the direct ^{22}Ne(α,γ) measurements. Hence, the spin-parity of the 11.3 MeV state has been constrained to $J^\pi = 0^+$ or 1^-.

Large uncertainties for the other three resonances of ^{26}Mg within the Gamow window is present due to the uncertainties in the spin-parity assignments and the resonance energies.

5.1 Reaction rate of the ^{22}Ne+α reaction

Constraining the reaction rate of the $^{22}Ne + \alpha$ reaction is important to understand the role of this reaction as a neutron source for the s-process. In order to calculate the reaction rate, it is important to know the exact center of mass energies of all the resonances involved in the reaction (E_R), and the strength of each of the resonances ($\omega\gamma$).

$$E_R = E_{ex} - Q \tag{5.1}$$

The resonance energies can be found as using the above equation by using the excitation energy of each state (E_{ex}) and the Q value of the reaction (Ex: 10.614 MeV for the ^{22}Ne(α, γ)^{26}Mg reaction, also called the *alpha threshold*).

$$N_A\langle\sigma v\rangle = 1.54 \times 10^5(\mu T_9)^{-\frac{3}{2}} \sum_i (\omega\gamma)_i \text{exp}\Big[-\frac{11.605E_{R,i}}{T_9}\Big] \quad \times (\text{ cm}^3\text{ s}^{-1}\text{ mol}^{-1}) \tag{5.2}$$

Once the resonance strength has been found, Equation 2.4 to calculate the rate of the reaction ($N_A\langle\sigma v\rangle$) can be written as Equation 5.2. Here N_A is the Avagadro's constant, μ is the reduced mass (in atomic mass units), T_9 is the temperature (in GK), $\omega\gamma$ is the resonance strength (in eV), and $E_{R,i}$ is the center of mass resonance energy of the i^{th} resonance (in MeV).

The reaction rate for the ^{22}Ne(α,n)^{25}Mg and ^{22}Ne(α,γ)^{26}Mg reactions can be calculated in this manner for the results from the present work and can be compared with previous work that have attempted to constrain the reaction rate of the ^{22}Ne(α,n)^{25}Mg reaction.

The contributions for the reaction rates by the relevant individual states within the Gamow window are shown in Figure 5.1. Out of the four resonances observed in the present study, only the 11.30 MeV state lies above the neutron decay threshold, which lies at E_x = 11.093 MeV. Hence,

this is the only state that contributes to the (α,n) reaction from the states observed in the present work. The Γ_n/Γ_γ ratio of 1.25 $\pm$ 0.28 [81] has been used for the neutron unbound state 11.30 MeV in both cases. The uncertainty in the partial alpha widths for each state for each angular momenta is considered for the curves in Figure 5.1. The dashed lines in Figure 5.1 represents the upper bound of the reaction rate for the 11.17 MeV state. This was calculated assuming an L=0 transferred momentum and the highest reported resonant energy of 11.167 MeV by Talwar $et.\ al$ [6]. For the upper limit reaction rate contributions from the 11.17 MeV state, the state was assumed to decay predominantly via neutron and gamma emission for the ^{22}Ne(α,n) and ^{22}Ne(α,γ) reactions, respectively.

Figure 5.2 shows the reaction rates for the ^{22}Ne(α,n) and ^{22}Ne(α,γ) reactions with the upper and lower bounds from the present work, and the most recent 82 MeV measurement by Talwar $et\ al.$ [6] as a ratio to the reaction rate from Käeppeler $et\ al.$ (1994) [7]. The reaction rates were all normalized to the rates published in Ref. [7]. The width of the bands for the reaction rate contributions from each state is mainly dominated by the uncertainty in the angular momentum (L=0,1,2) and the uncertainty in the resonance energy (20 keV for the neutron bound states). For the 11.30 MeV state, only L values of 0 and 1 are considered.

For the ^{22}Ne(α,n)^{25}Mg reaction rate comparison shown in Figure 5.2a, for the present measurement and the works of Talwar $et\ al.$ (2016) [6] and Käeppeler $et\ al.$ (1994) [7], higher lying resonances (E_x > 11319 keV) were adopted from the direct measurement of Jaeger $et\ al.$ [4]. For the strength of the resonance at 11.17 MeV from Käeppeler, 10% of the reported strength was used as explained in Ref. [7].

For the ^{22}Ne(α,γ)^{26}Mg reaction rate (Figure 5.2b), all the reported resonances within the Gamow energy window are taken into account. It is important to note that the work by Käeppeler $et\ al.$ have not included the resonances at 10.82 and 11.08 MeV.

For the upper bounds on the rates for the ^{22}Ne(α,n) and ^{22}Ne(α,γ) reactions from the present work in Figure 5.2, the upper limit for the resonance strength calculated for the 11.17 MeV state (assuming J=0) is included assuming that the state decays predominantly via neutron and gamma

emission, respectively.

5.2 Effect on the s-process isotope abundances

S-process nucleaosynthesis calculations can be performed using the code NEWTON (Nucleosynthesis of Elements With Transfer Of Neutrons) [83, 84] upgraded from the original version by Busso $et\ al.$ [85]. This code is devoted to neutron-capture nucleosynthesis for the main component (from Sr to Bi) of the s-process in low mass stars (less massive than 3 solar masses). However, this code can also be used for several ($\sim$400) other isotopes ranging from He to Bi, along with $\sim$500 reactions and possible decays for each. Using this code, several stellar models can be selected to describe the effect of the ^{22}Ne(α,n)^{26}Mg reaction as a neutron source for the s-process.

$$[Fe/H] = log_{10}\left(\frac{N_{Fe}}{N_H}\right)_{star} - log_{10}\left(\frac{N_{Fe}}{N_H}\right)_{sun} \tag{5.3}$$

In order to perform s-process nucleosynthesis calculations, a few different stellar models were chosen with different metallicities for the stars. The metallicity of a star describes the abundance of elements present that are heavier than hydrogen (H) and helium (He). These choices are listed below. The metallicity of a star is defined by the total amount of iron (Fe) content of the star along with the amount of hydrogen (H) that is present (hydrogen being the most abundant element in most stellar environments). The abundance ratio of a star is defined as a logarithm of the ratio of the iron abundance of the star to that of the sun (see Equation 5.3). Here N_{Fe} and N_H are the number of iron and hydrogen atoms per unit volume. [Fe/H] will be a positive logarithmic value for stars with a higher metallicity than our sun, and a negative value otherwise.

A 1.5 $M_\odot$ star is an appropriate model for a low-mass AGB star where the ^{13}C(α,n)^{16}O reaction is the main source of neutrons for the s-process. Stars of this mass do not have the required temperatures to effectively activate the ^{22}Ne(α,n)^{25}Mg reaction. In order to study the effect of the ^{22}Ne(α,n)^{25}Mg reaction as a neutron source, higher mass stellar models such as 3.0 $M_\odot$ or 5.0 $M_\odot$ are more appropriate where this reaction is the main neutron source in some cases. For Model 1 in Table 5.1, 1.5 $M_\odot$ and solar metallicity provides an environment with low temperatures and low

Model number	Stellar Mass	Metallicity [Fe/H]
1	1.5 $M_{\odot}$	+0.0
2	3.0 $M_{\odot}$	-0.5
3	5.0 $M_{\odot}$	+0.0

Table 5.1: The various stellar masses and metallicities used for s-process nucleosynthesis calculations.

neutron densities. For Models 2 and 3, environments with higher temperatures and higher neutron densities are considered.

$$P_{isotope} = \frac{m_{isotope}}{X^{\odot}_{isotope} \times M_{tot}} \tag{5.4}$$

These upper and lower limits for the reaction rates established in Section 5.1 are used as inputs to the NEWTON code in order to calculate the *Production Factors (P)* for all of the s-only isotopes for various stellar models. The production factor for an isotope can be calculated as shown in Equation 5.4. Here, $m_{isotope}$ is the total yield of a given isotope (in solar masses), M_{tot} is the initial mass of the star, and $X^{\odot}_{isotope}$ is the mass fraction of the isotope. The production factor is a measure of the amount of a certain isotope produced in a star compared with the amount of the same isotope in the Sun.

Production factors for the s-only isotopes for the three stellar models listed in Table 5.1 are shown in Figure 5.3. These calculations adopt the recommended value for the ^{22}Ne+α rate from Ref. [7] as the reference for normalization. The production factors have been calculated here for the upper and lower limit for the reaction rate produced by the present measurement, and the reaction rate from Ref. [6]. It can be seen in Figure 5.3a that for a low-mass star, the effect of the ^{22}Ne(α,n)^{26}Mg reaction on the production factors of the s-only isotopes is relatively low compared with other higher mass stars (Figures 5.3b, 5.3c). Variations are proportional to differences between the adopted rates (for different reaction rates used) and the reference, as expected. Moreover, changes are higher when the calculations were performed with higher masses models where

the ^{22}Ne+α reactions are expected to be more efficient. All these facts are plausible and seem to provide reasonable results.

The reason behind the increase/decrease of the production factors for specific s-only isotopes due to the lower reaction rate from the present measurement requires further analysis and is not ventured in the present work. We only make three general observations:

- The ^{22}Ne(α,n) reaction rate has a strong influence on the s-process nucleosynthesis in heavier stars.

- The lower reaction rate results in lower overall production of the s-process isotopes in general in heavier stars. This is not surprising, as the lower rate reduces the neutron flux available for the s-process.

- The (α, γ) reaction rate was fixed to that of Ref. [7] in these preliminary calculations. A more detailed study will be necessary to elucidate the effects due to the updated (α, γ) reaction rate.

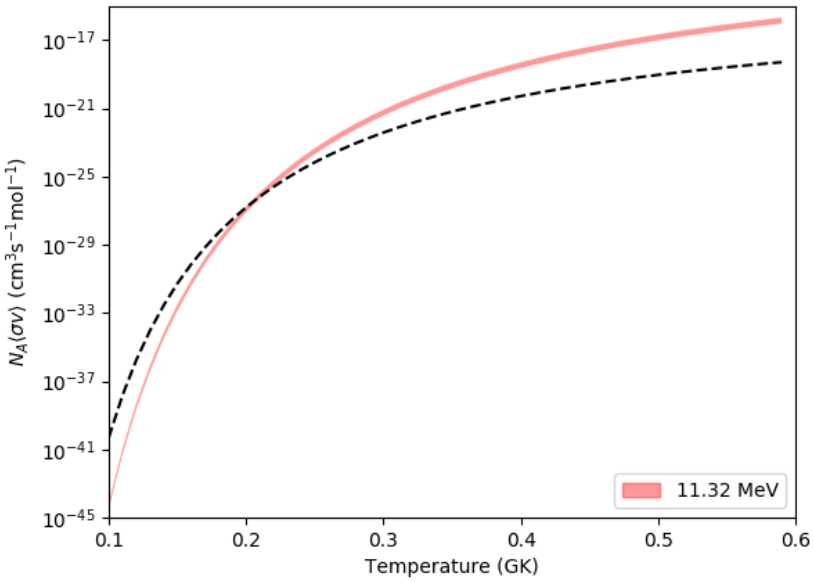

(a) ^{22}Ne(α,n)^{25}Mg reaction rate contribution from the 11.32 MeV state.

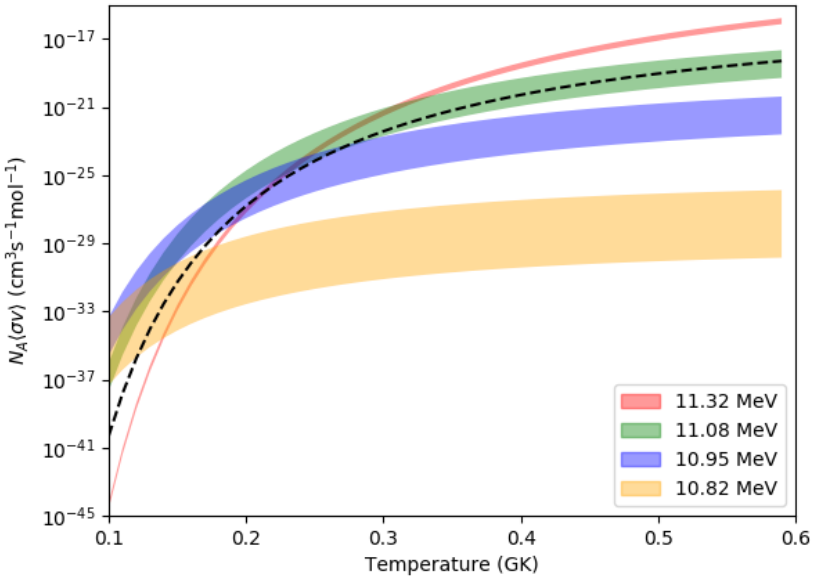

(b) ^{22}Ne(α,γ)^{26}Mg reaction rate contributions from individual states

Figure 5.1: Contributions from the observed states of ^{26}Mg for the rates of ^{22}Ne(α,n)^{25}Mg and ^{22}Ne(α,γ)^{26}Mg reactions. The widths of the bands represent the uncertainties of the spin-parity assignments, the resonance energies and the resonance strengths. The dashed line represents the upper bound of the reaction rate for the 11.17 MeV state in ^{26}Mg. The temperature region relevant for AGB stars is 0.2-0.3 GK.

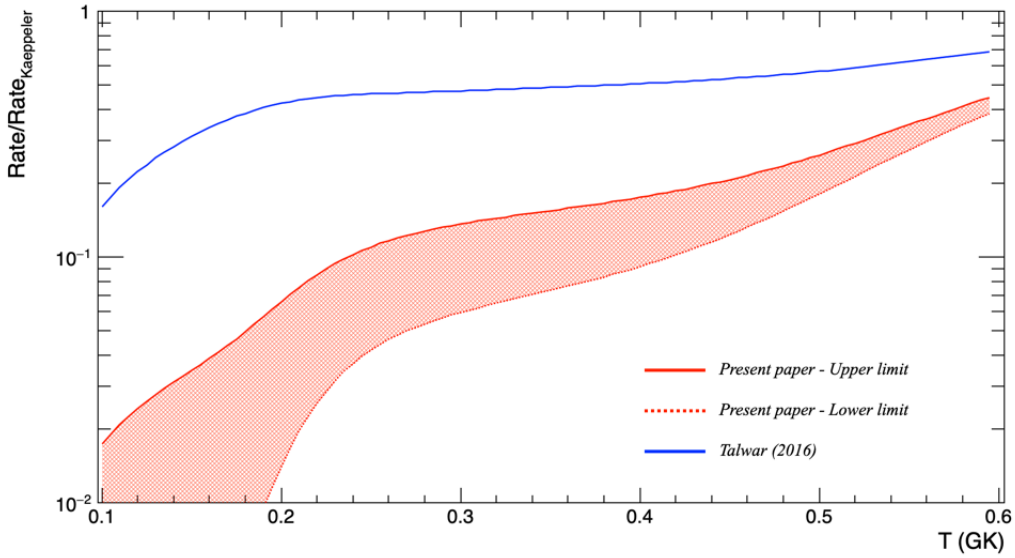

(a) ^{22}Ne(α,n)^{25}Mg reaction rate comparison

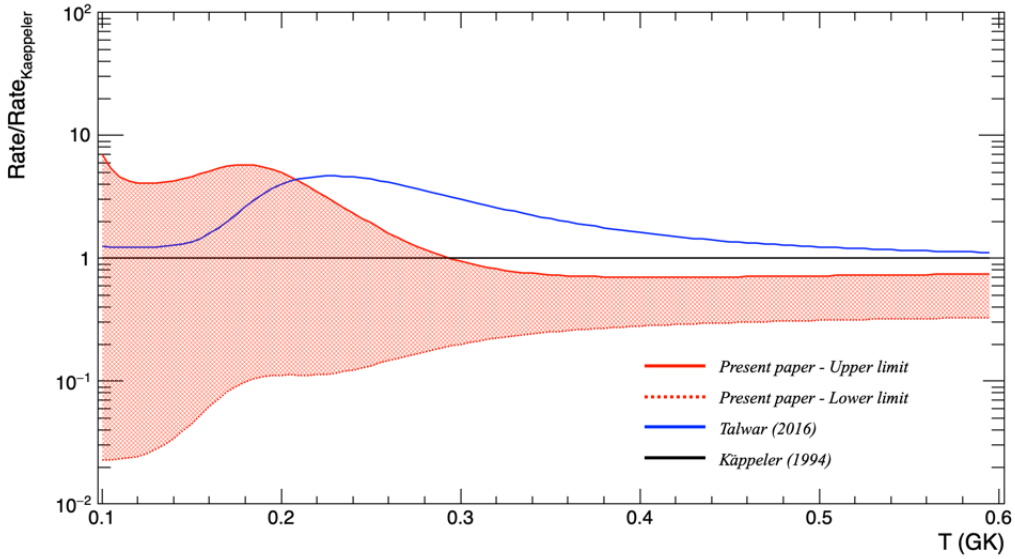

(b) ^{22}Ne(α,γ)^{26}Mg reaction rate comparison

Figure 5.2: Reaction rate comparisons for ^{22}Ne(α,n)^{25}Mg and ^{22}Ne(α,γ)^{26}Mg reactions using different studies (present work and Ref. [6]) normalized to the rate of Käeppeler (1994) [7].

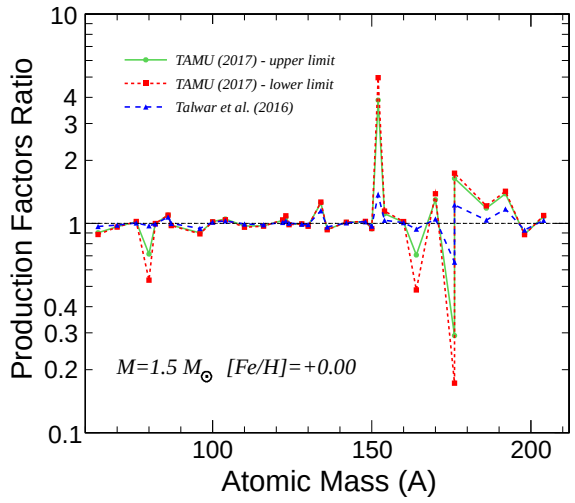

(a) 1.5 $M_{\odot}$

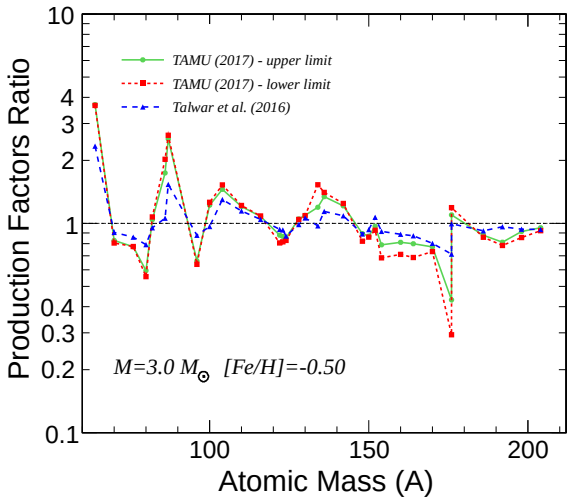

(b) 3.0 $M_{\odot}$

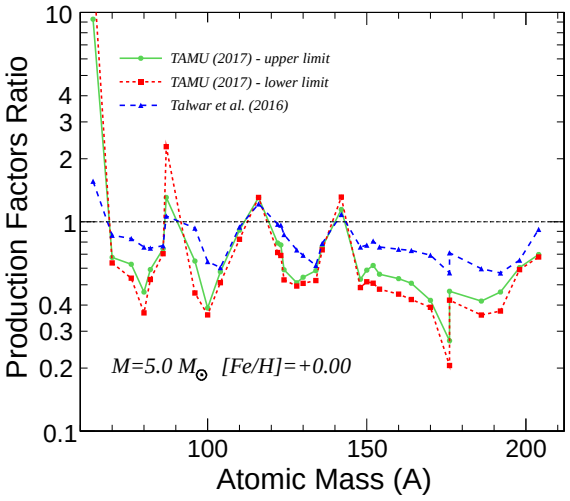

(c) 5.0 $M_{\odot}$

Figure 5.3: Production factors for the different stellar models listed in Table 5.1 normalized to that of Ref. [7].

6. CONCLUSION

The ^{22}Ne(^{6}Li,d)^{26}Mg alpha transfer reaction at sub-Coulomb energies was used to study the ^{22}Ne(α,n) and ^{22}Ne(α,γ) reactions, which are important for s-process nucleosynthesis in asymptotic giant branch stars. Measurements were performed using the MDM spectrometer and Oxford detector at the Texas A&M University Cyclotron Institute. Four resonances have been observed in excitation energy region of ^{26}Mg that corresponds to the Gamow energy window for the temperatures of interest for the ^{22}Ne(α,n) reaction in massive stars (0.2-0.3 GK).

The experimental cross sections and partial alpha widths for all four states have been established. The consistency of the applied method was tested using the ^{22}Ne(^{7}Li,t) reaction populating the same states in ^{26}Mg and producing the same partial width (although, only 11.3 MeV state had sufficient statistics in the ^{22}Ne(^{7}Li,t) measurements).

Out of the four observed states, the resonance at E_x = 11.319 MeV is the only resonance which contributes significantly to the ^{22}Ne(α,n) reaction at temperatures above 0.2 GK. The spin-parity of this state has been constrained to $J^\pi = 0^+$ or 1^- by requiring consistency with the previous direct ^{22}Ne(α,γ)^{26}Mg measurements [9, 26]. An upper bound for the partial alpha width of a possible state at E_x = 11.17 MeV is provided at 6.5 x 10^{-3} μeV, assuming 0^+ spin-parity (the resonance strength would be lower for any other spin-parity assignment).

The partial alpha width calculated for the 11.3 MeV state is lower compared with the previous direct ^{22}Ne(α,n) measurements, which in turn reduced the reaction rate of the ^{22}Ne(α,n) reaction by one order of magnitude as compared to Ref. [7], and by a factor of four as compared to Ref. [6]. This lowers the overall production of s-process isotopes in more massive stars (more than 5 solar masses) considerably in comparison with the rates adopted from previous measurements.

The ^{22}Ne(α,γ) reaction rate still has a large uncertainty below 0.3 GK. This is mostly due to uncertainties in spin-parity assignments and resonance energies. The rate recommended in Ref. [7] is within our uncertainty band. Future work is necessary to make the spin-parity assignments and to obtain accurate excitation energies for the observed resonances within the Gamow energy

window to further constrain the reaction rates of the ^{22}Ne(α,n) and ^{22}Ne(α,γ) reactions.

REFERENCES

[1] M. V. Persson, "Proposed internal structure of AGB star," 2014.

[2] R. Reifarth, C. Lederer, and F. Käppeler, "Neutron reactions in astrophysics," *Journal of Physics G: Nuclear and Particle Physics*, vol. 41, p. 053101, mar 2014.

[3] D. M. Pringle *et al.*, "The oxford mdm-2 magnetic spectrometer," *Nucl. Instr. Meth. Phys. Res.*, vol. 245, pp. 230–247, may 1986.

[4] M. Jaeger, R. Kunz, A. Mayer, J. W. Hammer, G. Staudt, K. L. Kratz, and B. Pfeiffer, "^{22}Ne(α,n)^{25}Mg: The Key Neutron Source in Massive Stars," *Physical Review Letters*, vol. 87, p. 202501, Nov. 2001.

[5] U. Giesen, C. P. Browne, J. Görres, S. Graff, C. Iliadis, H.-P. Trautvetter, M. Wiescher, W. Harms, K. L. Kratz, B. Pfeiffer, R. E. Azuma, M. Buckby, and J. D. King, "The astrophysical implications of low-energy resonances in ^{22}Ne + α," *Nuclear Physics A*, vol. 561, pp. 95–111, Aug. 1993.

[6] R. Talwar, T. Adachi, G. P. A. Berg, L. Bin, S. Bisterzo, M. Couder, R. J. deBoer, X. Fang, H. Fujita, Y. Fujita, J. Görres, K. Hatanaka, T. Itoh, T. Kadoya, A. Long, K. Miki, D. Patel, M. Pignatari, Y. Shimbara, A. Tamii, M. Wiescher, T. Yamamoto, and M. Yosoi, "Probing astrophysically important states in the ^{26}Mg nucleus to study neutron sources for the s process," *Phys. Rev. C*, vol. 93, p. 055803, May 2016.

[7] F. Kaeppeler, M. Wiescher, U. Giesen, J. Goerres, I. Baraffe, M. El Eid, C. M. Raiteri, M. Busso, R. Gallino, M. Limongi, and A. Chieffi, "Reaction rates for ^{18}O(α,γ)^{22}Ne, ^{22}Ne(α,γ)^{26}Mg, and ^{22}Ne(α,n)^{25}Mg in stellar helium burning and s-process nucleosynthesis in massive stars," *The Astrophysical Journal*, vol. 437, pp. 396–409, Dec. 1994.

[8] F. Käppeler, R. Gallino, S. Bisterzo, and W. Aoki, "The s process: Nuclear physics, stellar models, and observations," *Rev. Mod. Phys.*, vol. 83, pp. 157–193, Apr 2011.

[9] S. Hunt, C. Iliadis, A. Champagne, L. Downen, and A. Cooper, "New measurement of the E^{lab}=0.83 MeV resonance in ^{22}Ne(α ,γ)^{26}Mg," *Phys. Rev. C*, vol. 99, p. 045804, Apr. 2019.

[10] R. A. Alpher, H. Bethe, and G. Gamow, "The Origin of Chemical Elements," *Physical Review*, vol. 73, pp. 803–804, Apr. 1948.

[11] E. M. Burbidge, G. R. Burbidge, W. A. Fowler, and F. Hoyle, "Synthesis of the Elements in Stars," *Reviews of Modern Physics*, vol. 29, pp. 547–650, 1957.

[12] J. Audouze and J. W. Truran, "P-process nucleosynthesis in postshock supernova envelope environments," *The Astrophysical Journal*, vol. 202, pp. 204–213, Nov. 1975.

[13] S. E. Woosley and W. M. Howard, "The p-process in supernovae," *The Astrophysical Journal Supplement Series*, vol. 36, pp. 285–304, Feb. 1978.

[14] C. E. Rolfs and W. S. Rodney, "Cauldrons in the cosmos," *McGraw-Hill, New York*, 1988.

[15] M. Pignatari, R. Gallino, M. Heil, M. Wiescher, F. Käppeler, F. Herwig, and S. Bisterzo, "The weak s-process in massive stars and it's dependence on the neutron capture cross sections.," *The Astrophysical Journal*, vol. 710, pp. 1557–1577, Feb 2010.

[16] M. Heil, F. Käppeler, E. Uberseder, R. Gallino, and M. Pignatari, "Neutron capture cross sections for the weak s process in massive stars.," *Phys. Rev. C*, vol. 77, p. 015808, Jan 2008.

[17] C. M. Raiteri, M. Busso, R. Gallino, and G. Picchio, "S-process nucleosynthesis in massive stars and the weak component. II - Carbon burning and galactic enrichment," *The Astrophysical Journal*, vol. 371, pp. 665–672, Apr. 1991.

[18] S. Bisterzo, R. Gallino, F. Käppeler, M. Wiescher, G. Imbriani, O. Straniero, S. Cristallo, J. Görres, and R. J. deBoer, "The branchings of the main s-process: their sensitivity to α-induced reactions on ^{13}C and ^{22}Ne and to the uncertainties of the nuclear network," *Monthly Notices of the Royal Astronomical Society*, vol. 449, pp. 506–527, May 2015.

[19] F. Kappeler, H. Beer, and K. Wisshak, "s-process nucleosynthesis-nuclear physics and the classical model," *Reports on Progress in Physics*, vol. 52, pp. 945–1013, Aug. 1989.

[20] I. Iben, Jr., "Thermal pulses; p-capture, alpha-capture, s-process nucleosynthesis; and convective mixing in a star of intermediate mass," *The Astrophysical Journal*, vol. 196, pp. 525–547, Mar. 1975.

[21] I. Iben, Jr. and A. Renzini, "Asymptotic giant branch evolution and beyond," *Annual Review of Astronomy and Astrophysics*, vol. 21, pp. 271–342, 1983.

[22] P. C. Keenan and P. C. Boeshaar, "Spectral types of S and SC stars on the revised MK system," *The Astrophysical Journal Supplement Series*, vol. 43, pp. 379–391, July 1980.

[23] B. F. Peery, Jr., "Technetium Stars," *The Astrophysical Journal Letters*, vol. 163, p. L1, Jan. 1971.

[24] R. Guardiola, I. Moliner, and M. A. Nagarajan, "Alpha-cluster model for ^{8}Be and ^{12}C with correlated alpha particles," *Nuclear Physics A*, vol. 679, pp. 393–409, Jan. 2001.

[25] E. D. Johnson, G. V. Rogachev, V. Z. Goldberg, S. Brown, D. Robson, A. M. Crisp, P. D. Cottle, C. Fu, J. Giles, B. W. Green, K. W. Kemper, K. Lee, B. T. Roeder, and R. E. Tribble, "Extreme α -clustering in the ^{18}O nucleus," *European Physical Journal A*, vol. 42, pp. 135–139, Nov. 2009.

[26] K. Wolke, H. W. Becker, C. Rolfs, U. Schröder, H. P. Trautvetter, V. Harms, K. L. Kratz, J. W. Hammer, M. Wiescher, and A. Wöhr, "Helium burning of ^{22}Ne.," *Zeitschrift fur Physik A Hadrons and Nuclei*, vol. 334, pp. 491–510, Dec. 1989.

[27] V. Harms, K.-L. Kratz, and M. Wiescher, "Properties of ^{22}Ne(α,n)^{25}Mg resonances," *Phys. Rev. C*, vol. 43, pp. 2849–2861, June 1991.

[28] E. Kuhlmann, E. Ventura, J. R. Calarco, D. G. Mavis, and S. S. Hanna, "E1 and E2 strength in ^{24}Mg and ^{26}Mg observed in α-capture reactions," *Phys. Rev. C*, vol. 11, pp. 1525–1536, May 1975.

[29] F. X. Haas and J. K. Bair, "Total Neutron Yield from the (α, n) Reaction on ^{21,22}Ne," *Phys. Rev. C*, vol. 7, pp. 2432–2436, June 1973.

[30] H. W. Drotleff, A. Denker, J. W. Hammer, H. Knee, S. Küchler, D. Streit, C. Rolfs, and H. P. Trautvetter, "New^{22}Ne(α,n)^{25}Mg-resonances at very low energies relevant for the astrophysical s-process," *Zeitschrift fur Physik A Hadrons and Nuclei*, vol. 338, pp. 367–368, Sept. 1991.

[31] H. W. Drotleff, A. Denker, H. Knee, M. Soine, G. Wolf, J. W. Hammer, U. Greife, C. Rolfs, and H. P. Trautvetter, "Reaction rates of the s-process neutron sources ^{22}Ne(α,n)^{25}Mg and ^{13}C(α,n)^{16}O," *The Astrophysical Journal*, vol. 414, pp. 735–739, Sept. 1993.

[32] D. Ashery, "Study of the ^{22}Ne(α, n) ^{25}Mg reaction: a possible source of stellar neutronS," *Nuclear Physics A*, vol. 136, pp. 481–495, 1969.

[33] A. A. Sonzogni, "Nudat 2.0: Nuclear structure and decay data on the internet," *AIP Conference Proceedings*, vol. 769, no. 1, pp. 574–577, 2005.

[34] C. Massimi *et al.*, "Neutron spectroscopy of ^{26}Mg states: Constraining the stellar neutron source ^{22}Ne(α,n)^{25}Mg," *Physics Letters B*, vol. 768, pp. 1–6, May 2017.

[35] P. E. Koehler, "Constraints on the $^{22}\mathrm{Ne}(\alpha, n)^{25}\mathrm{Mg}$ s-process neutron source from analysis of $^{\mathrm{nat}}\mathrm{Mg} + n$ total and $^{25}\mathrm{Mg}(n, \gamma)$ cross sections," *Phys. Rev. C*, vol. 66, p. 055805, Nov 2002.

[36] C. Massimi *et al.*, "Resonance neutron-capture cross sections of stable magnesium isotopes and their astrophysical implications," *Phys. Rev. C*, vol. 85, p. 044615, Apr 2012.

[37] C. Moss, "Excitation energies of levels in $^{23}\mathrm{Na}$, $^{24}\mathrm{Mg}$ and $^{26}\mathrm{Mg}$," *Nuclear Physics A*, vol. 269, no. 2, pp. 429 – 442, 1976.

[38] P. Adsley, J. W. Brümmer, T. Faestermann, S. P. Fox, F. Hammache, R. Hertenberger, A. Meyer, R. Neveling, D. Seiler, N. de Séréville, and H.-F. Wirth, "High-resolution study of levels in the astrophysically important nucleus ^{26}Mg and resulting updated level assignments," *Phys. Rev. C*, vol. 97, p. 045807, Apr. 2018.

[39] P. Adsley, J. W. Brümmer, K. C. W. Li, D. J. Marín-Lámbarri, N. Y. Kheswa, L. M. Donaldson, R. Neveling, P. Papka, L. Pellegri, V. Pesudo, L. C. Pool, F. D. Smit, and J. J. van

Zyl, "Re-examining the ^{26}Mg(α ,α')^{26}Mg reaction: Probing astrophysically important states in ^{26}Mg," *Phys. Rev. C*, vol. 96, p. 055802, Nov. 2017.

[40] R. Longland, C. Iliadis, G. Rusev, A. P. Tonchev, R. J. deBoer, J. Görres, and M. Wiescher, "Photoexcitation of astrophysically important states in ^{26}Mg," *Phys. Rev. C*, vol. 80, p. 055803, Nov 2009.

[41] R. Schwengner, A. Wagner, Y. Fujita, G. Rusev, M. Erhard, D. De Frenne, E. Grosse, A. R. Junghans, K. Kosev, and K. D. Schilling, "Dipole transition strengths in ^{26}Mg," *Phys. Rev. C*, vol. 79, p. 037303, Mar 2009.

[42] R. J. deBoer, M. Wiescher, J. Görres, R. Longland, C. Iliadis, G. Rusev, and A. P. Tonchev, "Photoexcitation of astrophysically important states in ^{26}Mg. ii. ground-state-transition partial widths," *Phys. Rev. C*, vol. 82, p. 025802, Aug 2010.

[43] I. J. Thompson and F. M. Nunes, *Nuclear Reactions for Astrophysics*. Cambridge University Press, July 2009.

[44] G. R. Satchler, "Introduction to nuclear reactions," *Oxford University Press*, 1990.

[45] S. Bottoni *et al.*, "Cluster-transfer reactions with radioactive beams: A spectroscopic tool for neutron-rich nuclei," *Phys. Rev. C*, vol. 92, p. 024322, Aug. 2015.

[46] G. R. Satchler and W. G. Love, "Folding model potentials from realistic interactions for heavy-ion scattering," *Physics Reports*, vol. 55, pp. 183–254, Oct. 1979.

[47] C. Iliadis, "Proton single-particle reduced widths for unbound states," *Nuclear Physics A*, vol. 618, no. 1, pp. 166 – 175, 1997.

[48] S. E. Hale, A. E. Champagne, C. Iliadis, V. Y. Hansper, D. C. Powell, and J. C. Blackmon, "Investigation of the ^{22}Ne(p,γ)^{23}Na reaction via (^{3}He,d) spectroscopy," *Phys. Rev. C*, vol. 65, p. 015801, Jan. 2002.

[49] J. Schiffer, "Proton widths in a diffuse well," *Nuclear Physics*, vol. 46, pp. 246 – 250, 1963.

[50] G. Breit and E. Wigner, "Capture of slow neutrons," *Phys. Rev.*, vol. 49, pp. 519–531, Apr 1936.

[51] H. T. Fortune, "Definitions of a single-particle resonance," *Phys. Rev. C*, vol. 73, p. 014318, Jan 2006.

[52] G. Baur, "Breakup reactions as an indirect method to investigate low-energy charged-particle reactions relevant for nuclear astrophysics," *Physics Letters B*, vol. 178, no. 2, pp. 135 – 138, 1986.

[53] H. M. Xu, C. A. Gagliardi, R. E. Tribble, A. M. Mukhamedzhanov, and N. K. Timofeyuk, "Overall normalization of the astrophysical s factor and the nuclear vertex constant for $^{7}\mathrm{Be}(p,\gamma)^{8}\mathrm{B}$ reactions," *Phys. Rev. Lett.*, vol. 73, pp. 2027–2030, Oct 1994.

[54] C. R. Brune, W. H. Geist, R. W. Kavanagh, and A. K. Veal, "Sub-Coulomb α Transfers on ^{12}C and the ^{12}C(α,γ)^{16}O S Factor," *Physical Review Letters*, vol. 83, pp. 4025–4028, Nov. 1999.

[55] M. L. Avila, G. V. Rogachev, E. Koshchiy, L. T. Baby, J. Belarge, K. W. Kemper, A. N. Kuchera, and D. Santiago-Gonzalez, "α-cluster asymptotic normalization coefficients for nuclear astrophysics," *Phys. Rev. C*, vol. 90, p. 042801, Oct 2014.

[56] M. L. Avila, G. V. Rogachev, E. Koshchiy, L. T. Baby, J. Belarge, K. W. Kemper, A. N. Kuchera, A. M. Mukhamedzhanov, D. Santiago-Gonzalez, and E. Uberseder, "Constraining the 6.05 MeV 0^+ and 6.13 MeV 3^- cascade transitions in the $^{12}\mathrm{C}(\alpha,\gamma)^{16}\mathrm{O}$ reaction using the asymptotic normalization coefficients," *Phys. Rev. Lett.*, vol. 114, p. 071101, Feb 2015.

[57] M. L. Avila, G. V. Rogachev, E. Koshchiy, L. T. Baby, J. Belarge, K. W. Kemper, A. N. Kuchera, and D. Santiago-Gonzalez, "New measurement of the α asymptotic normalization coefficient of the $1/2^+$ state in $^{17}\mathrm{O}$ at 6.356 MeV that dominates the $^{13}\mathrm{C}(\alpha,n)^{16}\mathrm{O}$ reaction rate at temperatures relevant for the s process," *Phys. Rev. C*, vol. 91, p. 048801, Apr 2015.

[58] A. M. Mukhamedzhanov, "Coulomb renormalization and ratio of proton and neutron asymptotic normalization coefficients for mirror nuclei," *Phys. Rev. C*, vol. 86, p. 044615, Oct 2012.

[59] A. M. Mukhamedzhanov and R. E. Tribble, "Connection between asymptotic normalization coefficients, subthreshold bound states, and resonances," *Phys. Rev. C*, vol. 59, pp. 3418–3424, June 1999.

[60] A. M. Lane and R. G. Thomas, "R-Matrix Theory of Nuclear Reactions," *Reviews of Modern Physics*, vol. 30, pp. 257–353, Apr. 1958.

[61] A. M. Lane, "Reduced Widths of Individual Nuclear Energy Levels," *Reviews of Modern Physics*, vol. 32, pp. 519–566, July 1960.

[62] S. Kowalski, and H. A. Enge, "Computer code raytrace (unpublished)," Univeristy of Oxford, England, UK, 1986.

[63] V. K. Shen, D. W. Siderius, W. P. Krekelberg, and H. W. Hatch, *NIST Standard Reference Simulation Website*. NIST Standard Reference Database Number 173, National Institute of Standards and Technology, Gaithersburg MD, 20899.

[64] A. Spiridon, "Update on the upgrade of the oxford detector.," *Progress in Research, Cyclotron Institute, Texas A&M University*, pp. IV–32, 2014.

[65] Y. Giomataris *et al.*, "Micromegas: a high-granularity position-sensitive gaseous detector for high particle-flux environments," *Nucl. Instr. Meth. Phys. Res.*, vol. 376, no. 1, pp. 29–35, 1996.

[66] I. Antcheva, M. Ballintijn, B. Bellenot, M. Biskup, R. Brun, N. Buncic, P. Canal, D. Casadei, O. Couet, V. Fine, L. Franco, G. Ganis, A. Gheata, D. G. Maline, M. Goto, J. Iwaszkiewicz, A. Kreshuk, D. M. Segura, R. Maunder, L. Moneta, A. Naumann, E. Offermann, V. Onuchin, S. Panacek, F. Rademakers, P. Russo, and M. Tadel, "Root a c++ framework for petabyte data storage, statistical analysis and visualization," *Computer Physics Communications*, vol. 180, no. 12, pp. 2499 – 2512, 2009. 40 YEARS OF CPC: A celebratory issue focused on quality software for high performance, grid and novel computing architectures.

[67] C. Ugalde, A. E. Champagne, S. Daigle, C. Iliadis, R. Longland, J. R. Newton, E. Osenbaugh-Stewart, J. A. Clark, C. Deibel, A. Parikh, P. D. Parker, and C. Wrede, "Experimental evi-

dence for a natural parity state in Mg26 and its impact on the production of neutrons for the s process," *Phys. Rev. C*, vol. 76, p. 025802, Aug. 2007.

[68] J. Cook, "Global optical-model potentials for the elastic scattering of ^{6,7}Li projectiles," *Nuclear Physics A*, vol. 388, pp. 153–172, Oct. 1982.

[69] Y. P. Xu and D. Y. Pang, "Toward a systematic nucleus-nucleus potential for peripheral collisions," *Phys. Rev. C*, vol. 87, p. 044605, Apr 2013.

[70] L. C. Chamon, "The São Paulo Potential," *Nuclear Physics A*, vol. 787, pp. 198–205, May 2007.

[71] H. An and C. Cai, "Global deuteron optical model potential for the energy range up to 183 MeV," *Phys. Rev.*, vol. C73, p. 054605, 2006.

[72] E. D. Johnson, G. V. Rogachev, A. M. Mukhamedzhanov, L. T. Baby, S. Brown, W. T. Cluff, A. M. Crisp, E. Diffenderfer, V. Z. Goldberg, B. W. Green, T. Hinners, C. R. Hoffman, K. W. Kemper, O. Momotyuk, P. Peplowski, A. Pipidis, R. Reynolds, and B. T. Roeder, "Astrophysical Reaction Rate for the Neutron-Generator Reaction C13(α,n)O16 in Asymptotic Giant Branch Stars," *Physical Review Letters*, vol. 97, p. 192701, Nov. 2006.

[73] V. Goldberg, A. Volya, A. Nurmukhanbetova, D. Nauruzbayev, and G. Rogachev, "Alpha cluster resonances in light nuclei," *EPJ Web Conf.*, vol. 165, p. 02004, 2017.

[74] K.-I. Kubo and M. Hirata, "Dwba treatment of cluster transfer reactions," *Nuclear Physics A*, vol. 187, no. 1, pp. 186 – 204, 1972.

[75] F. D. Becchetti, D. Overway, J. Janecke, and W. W. Jacobs, "^{12}C(^{6}Li, d)^{16}O at E(Li) = 90 MeV," *Nuclear Physics A*, vol. 344, pp. 336–350, Aug. 1980.

[76] N. K. Glendenning, *Direct Nuclear Reactions*. WORLD SCIENTIFIC, 2004.

[77] B. Buck and A. A. Pilt, "Alpha-particle and triton cluster states in ^{19}F," *Nuclear Physics A*, vol. 280, pp. 133–160, Apr. 1977.

[78] D. R. Tilley, C. M. Cheves, J. L. Godwin, G. M. Hale, H. M. Hofmann, J. H. Kelley, C. G. Sheu, and H. R. Weller, "Energy levels of light nuclei A=5, 6, 7," *Nuclear Physics A*, vol. 708, pp. 3–163, Sept. 2002.

[79] X. Li, C. Liang, and C. Cai, "Global triton optical model potential," *Nuclear Physics A*, vol. 789, pp. 103–113, June 2007.

[80] C. Perey and F. Perey, "Compilation of phenomenological optical-model parameters 19541975," *Atomic Data and Nuclear Data Tables*, vol. 17, no. 1, pp. 1 – 101, 1976.

[81] S. Ota, G. Christian, *et al.* Private Communication.

[82] P. M. Endt, "Supplement to energy levels of A = 21-44 nuclei (VII)," *Nuclear Physics A*, vol. 633, pp. 1–220, Apr. 1998.

[83] O. Trippella, M. Busso, E. Maiorca, F. Käppeler, and S. Palmerini, "s-Processing in AGB Stars Revisited. I. Does the Main Component Constrain the Neutron Source in the ^{13}C Pocket?," *The Astrophysical Journal*, vol. 787, p. 41, May 2014.

[84] O. Trippella, M. Busso, S. Palmerini, E. Maiorca, and M. C. Nucci, "s-Processing in AGB Stars Revisited. II. Enhanced ^{13}C Production through MHD-induced Mixing," *The Astrophysical Journal*, vol. 818, p. 125, Feb. 2016.

[85] M. Busso, R. Gallino, and G. J. Wasserburg, "Nucleosynthesis in Asymptotic Giant Branch Stars: Relevance for Galactic Enrichment and Solar System Formation," *Annual Review of Astronomy and Astrophysics*, vol. 37, pp. 239–309, 1999.